12-18-2018

Investigation of a Non-Premixed Liquid Fuel Injector and Swirler Using a Purpose-Built Combustion Test Rig

Kyle Twarog
kyle.twarog@uconn.edu

Investigation of a Non-Premixed Liquid Fuel Injector and Swirler Using a Purpose Build Combustion Test Rig

Kyle Evan Twarog

B.S., University of Connecticut, 2017

A Thesis

Submitted in Partial Fulfillment of the

Requirements for the Degree of

Master of Science

At the

University of Connecticut

2019

APPROVAL PAGE

Masters of Science Thesis

Investigation of a Non-Premixed Liquid Fuel Injector and Swirler Using a Purpose Build Combustion Test Rig

Presented by

Kyle Evan Twarog, B.S.

Major Advisor: _____

Dr. Chih-Jen Sung

Associate Advisor: _____

Dr. Baki M. Cetegen

Associate Advisor: _____

Dr. Bryan Weber

University of Connecticut

2019

Acknowledgements

I would like to thank Dr. Chih-Jen Sung for introducing me to the worlds of laser diagnostics and combustion science. His mentorship, dedication, and patience have been nothing short of irreplaceable.

I would like to thank Dr. Hukam Mongia for introducing me to the field of spray diagnostics and helping guide me through this investigation.

I would like to thank my parents for their support throughout this journey, both as rocks to keep me grounded and spurs to push me forward.

I would like to thank Dr. Xin Xue for his support and insight into laser diagnostics.

I would like to thank all of my colleagues in the Combustion Diagnostics Laboratory for their advice, support, and perspective.

Table of Contents

List of Figures

List of Tables

Chapter I. Introduction

1.1 Motivations and Scope

Ever since the 1970s, one of the principle motivations of combustor and injection system design has been the improvement of emissions profiles of commercial gas turbine engines[1-3]. These improvements have taken the form of optimizations of flame parameters, air-fuel flow schemes, and fuel atomization quality among others. Originally testing these improvements in a practical environment required the construction and testing of a full scale gas turbine. In these experiments the engine is supplied with air at intake speeds and pressures similar to the altitude of operation and gas analyzers, thermocouples, and load cells are be utilized to determine both the propulsive and emission performance of the engine. While this method certainly was, and remains, the highest fidelity testing method for a practical engine this method requires the construction of a large fan-fed blast tunnel for experimentation as well as the construction of full scale engines for testing. This makes the testing of full scale engine designs impractical for initial design and research purposes.

It is possible to divide modern annular combustors into individual segments for testing. In these tests only a single portion of the annular combustor is produced and supplied with fuel and air in a well-controlled laboratory environment. This allows for facilities of lesser scope to be employed and the additional benefit of direct study of the flame and flow field as the engine casing does not have to be constructed. Despite these facts these tests still require the construction of very specialized exhaust and fire suppression systems, usually requiring their own building or wing, and the fabrication of large portions of practical engines for study, both being expensive propositions. Moreover, this form of testing still renders the fundamental study of design parameters challenging, as it does not eliminate the interactions between individual air and fuel components. As such, this form of analysis is more commonly employed in computational fluid dynamics (CFD) than experimental research as these computational studies can take advantage of the symmetry of the

annular combustor to allow for increased mesh resolution to be established for a given section of the combustor.[4-7]

In order to further reduce the barriers to research it has been common to study a single element of a combustor: this being a single fuel injection system, swirler assembly, and a confined combustion domain. This allows for not only the construction of larger numbers of design parameters to be tested efficiently, but it also allows for the elimination of the effects of the interaction between elements for parametric study. Single element testing also allows for the employment of a wide range of diagnostic methods, as the combustion domain can be fabricated specifically for this purpose[7]. The use of single elements for testing also allows for practical comparisons to be conducted between specific element designs and their meshed equivalents in CFD, as shown by Han et al[9,10].

Recently research groups have employed overlaid and simultaneous diagnostics techniques in single element testing[11-12]. Temme et al.[13] were able to employ particle image velocimetry (PIV), chemiluminescence, raw visual spectrum analysis, and confinement mounted thermocouples to study lean combustion of a single element. This represented a significant improvement in the ability to image, study, and manipulate the combustion performance of a flame compared to previous efforts, such as those of Johnson et al[8], that employed a singular PIV plane and a global downstream species measurement.

Even with this improved diagnostics capability, these efforts were similar in that they all utilized gaseous fuels or pre-evaporated liquid fuels. This was done for practical reasons, as the use of gaseous fuels in the single element allowed for the elimination of any spray effects from a liquid phase. This in turn allowed for the elimination of spray-air effects, mechanical influences on the spray field, and interference in diagnostics methods introduced by the presence of the liquid phase. Despite this isolation of combustion and air flow phenomena, the usage of gaseous fuels resulted in a loss of fidelity as most gas turbine applications utilize liquid fuels in their production combustors.

As such, the goal of this project is to develop a series of test stations capable of conducting comprehensive air flow, combustion, and spray diagnostics on a practical non-premixed liquid fuel single element. This capability is not only to allow for the testing of engineering designs, but also to allow for the fundamental study of the effects of parameters such as air/fuel flow rates and fuel atomization characteristics on the combustion process. More specifically the diagnostic methods included are to be sufficient to allow for the development and validation of spray and flame models for use in CFD simulations as well as providing the boundary conditions necessary conduct such simulations on a given geometry. This experimental capability will therefore be essential to any future modeling or simulation effort and will allow for the application of models to specific element geometries of varying family or type. Due to the nature of the simulation inputs this rig will require the deployment of a much wider ranger range of diagnostic tools than other of existing liquid fuel element experiments such as those of Grohmann[11] or Chterev et al[10]. These methods are to include high-speed PIV, Malvern spray diagnostics, and planar laser induced fluorescence (PLIF).

1.2 Organization of this Thesis

Chapter 2 details the experimental rig utilized for this effort including both the air and fuel delivery systems and the utilized diagnostics methods. The injector and swirler are also detailed.

Chapter 3 discusses the procedure and results of effective area measurements undertaken on the element assembly. This includes both the equations utilized for the ACd calculation.

Chapter 4 the results of spray diagnostics undertaken with the injector. Droplet size values are presented for various fuel pressure level and analysis of the pressure effect on droplet size trend is provided.

Chapter 5 provides detailed analysis of the nonreacting flow field via PIV measurements. Time resolved flow structures are presented and discussed at various pressure drops as well as varying radial locations. Flow symmetry is discussed in terms of both bulk and fluctuation velocities.

Chapter 6 includes analysis of the reacting flow field via PIV measurements. Comparisons are made between the reacting and nonreacting flow structures. Complications and limitations of the flow field measurement are discussed.

Chapter 7 discusses the chemiluminescence profiles of the 3% pressure drop condition. Measurements of OH*, CH*, and NO_2* are discussed and compared.

Chapter 8 provides details regarding the visible spectrum emittance of the flame.

Chapter 9 details the results of formaldehyde PLIF at the 3% pressure drop condition. Post processing methods are presented, as are overall formaldehyde distributions.

Chapter 10 provides the results of hydroxyl PLIF at the 3% pressure drop condition. Bulk hydroxyl distributions are discussed and compared with those of formaldehyde PLIF.

Chapter 11 provides conclusions based on the gathered diagnostics information. Conclusions regarding the location of the heat release region of the flame are presented. Discussions regarding the abilities of this combustion test rig are presented.

Chapter 12 lists recommendations for future work. Suggested improvements to the established test rig are detailed so as to expand its capabilities. Recommendations for further study of the tested element are detailed.

Chapter II: Testing Rig Details

Time-resolved particle imaging velocimetry (TR-PIV) measurements and effective area (ACd) analysis were conducted utilizing a fixed injector test rig. The air supply of this rig consisted of a pre-charged 400 gallon air tank and an on-board air flow control system. The flow control board consisted of a manually adjustable pressure regulator and two 0.125 inch sonic nozzles, establishing a choked flow condition so as to allow for variable control of the air mass flow rate. A schematic of this system can be seen in Figure 1. Before testing the sonic nozzle pair was calibrated utilizing a dry air flow meter. Air supplied through these nozzles then routed to a collimating rectangular air plenum, to which the injector assembly and a pressure transducer were mounted. This air box was in turn mounted to a three-axis adjustable platform so as to allow for precise control of the location and orientation of the TR-PIV measurement plane. During TR-PIV testing a separate seeding airline was added, diverting 30% of the air supplied by the sonic nozzles through a fluidized bed of 1-micron aluminum oxide particles. This seeding air flow entrained the particles before rejoining the main air line, thus achieving reliable and controllable global seeding of the airflow[14]. These particles were chosen for reactive testing as they do not react with the flame, thus allowing for measurement throughout the flow field. These particles were also selected for non-reactive TR-PIV testing, rather than an oil particle or other similar method, so as to maintain consistency across the two measurements. This allows the two measurements to be compared directly.

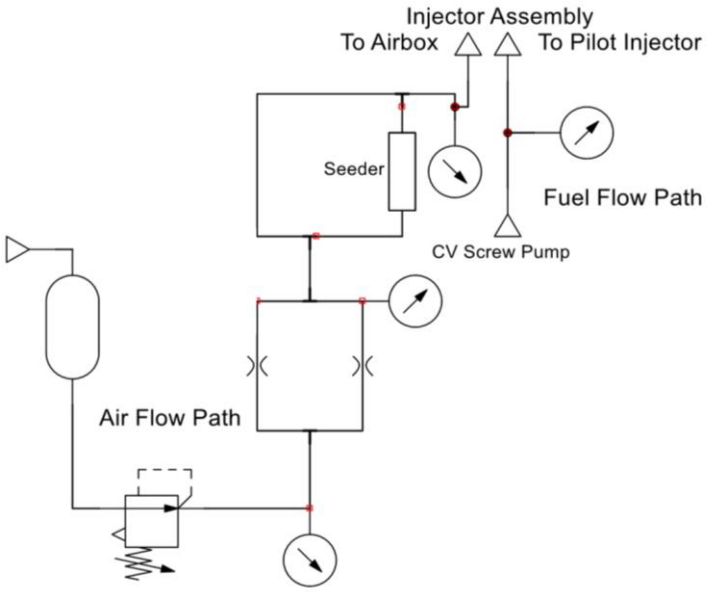

Figure 1: Air and Fuel Flow Paths for Experimental Rig

The particle diameter itself was chosen so as to minimize the particle response time, thus allowing for high fidelity measurement of all portions of the flow[14-17]. The small particle size was also chosen so as to allow for high seeding density. High speed flows are extremely difficult to seed consistently, and small solid particles have a tendency to allow for more consistent entrainment within fluidized bed seeders than larger ones for experiments of this duration[14].

Table 1: Jet-A Fuel Properties[18]	
Property	Value
Aromatics (% Volume)	17
Total Sulfur (% mass)	0.04
Flash Point °C	48
Density at 15°C (kg/m^3)	803
Viscosity at -20°C (mm^2/s)	4.5
Hydrogen Content (% mass)	13.9
Net Heat of Combustion (MJ/kg)	43

Fuel (Jet-A POSF10325) was supplied to the injector via a Teledyne 1000D high-pressure syringe pump. This pump was digitally controlled and allowed for constant mass fuel flow rates to be supplied during each trial with a continuous error of 0.05% of the prescribed flow rate. Fuel pressure was monitored via a pressure transducer built into the pump with an accuracy of 0.6895 bar. A complete top view of the diagnostic configuration of the experimental rig can be found in Figure 2. A complete schematic of the fluid delivery configuration of the experimental rig can be found in Figure 1. The properties of the fuel batch utilized can be found in Table 1.

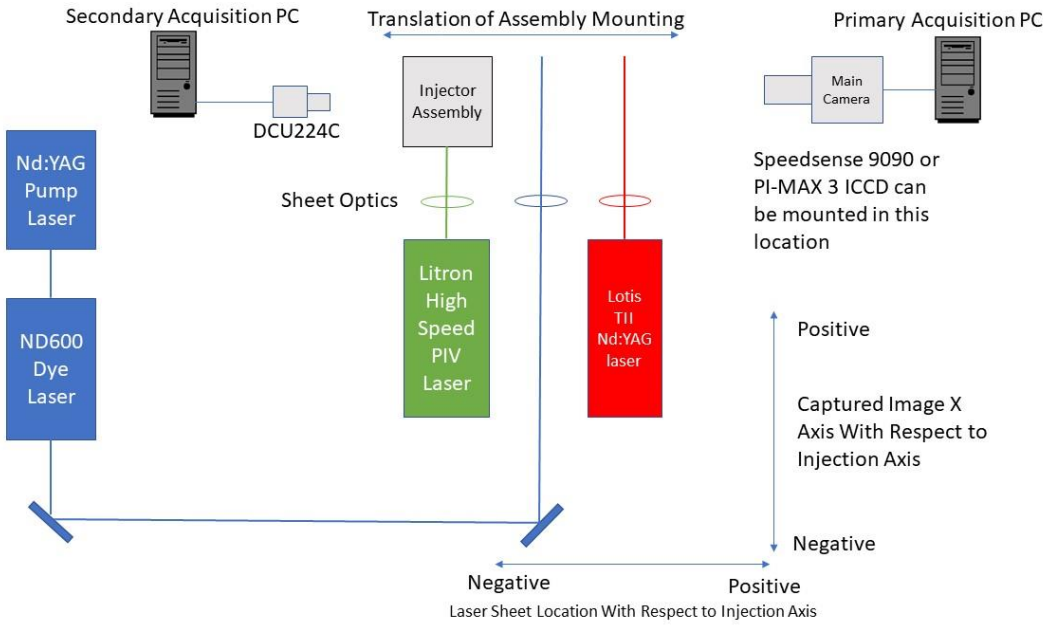

Figure 2: Top View of Main Testing Rig

A fused quartz chamber was utilized for investigating confined air and fuel flow characteristics for all TR-PIV testing. The chamber with internal dimensions 80x80x254 mm was mounted to the top of the injector mounting plate, with the interface between them being sealed by a carbon paper gasket. The surfaces of this chamber were not temperature controlled during experimentation. Between all trials it was ensured that the chamber was

mounted so that is centroid would be within 0.5 mm of the injection axis across the injection plane.

For spray analysis a separate test rig was utilized. In this rig the injector itself was mounted to a fixed cantilever such that the measurement axis of a Malvern Spraytech system would pass through the injection axis, 50.8 mm downstream of the injection plane. A fixed CMOS camera was mounted adjacent to the Malvern system so as to record the spray pattern of each trial. The same syringe fuel pump described in the TR-PIV test rig was utilized for spray testing. A side view of the Malvern portion of this rig can be found in Figure 3. This configuration was very similar to that utilized for spray characterization of higher pressure injectors by Sivakumar et al[19].

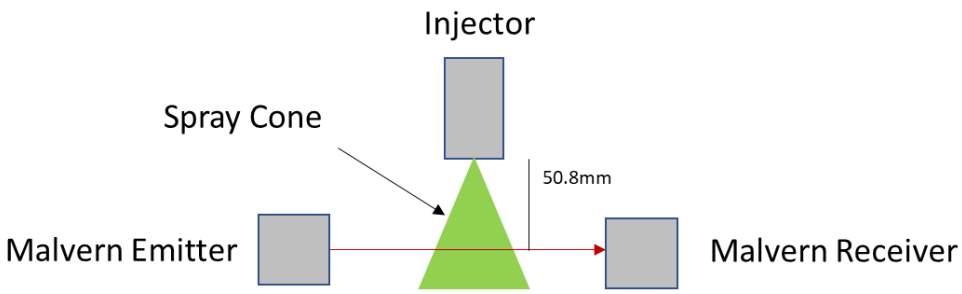

Figure 3: Malvern SprayTech Rig Side View

The injector system utilizing for this experiment consisted of a pressure-swirl nozzle and a three-stage swirler. The swirler consisted of a 40-degree clockwise inner stage, 45-degree counter-clockwise middle stage, and dilution outer stage. The injector and swirler were mounted to the top plate of the plenum, along with the confinement chamber. A basic schematic of this assembly can be found in Figure 4.

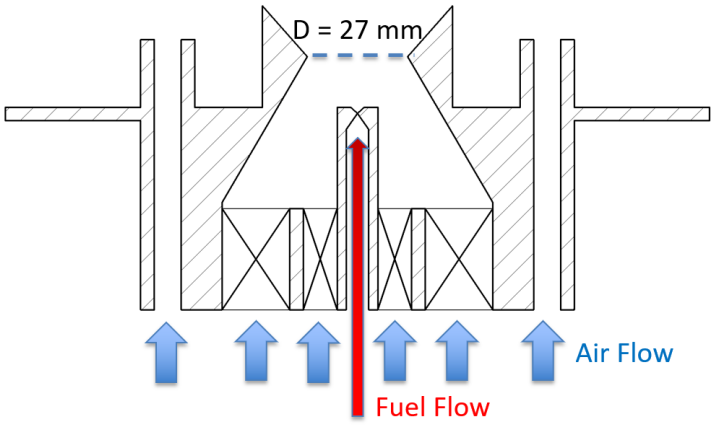

Figure 4: Injector/Swirler Assembly Schematic

Spray testing of the fuel injector was conducted using Jet-A and the Malvern analysis unit. Particle sizing analysis was conducted with the injector inverted and with the line-of-sight of the Malvern system being located through the injection axis at y/D=1.88 (50.8 mm) from the injection plane. To determine the droplet size characteristics, three trials were taken at each condition, with each trial being averaged over 30 seconds. So as to eliminate aeration effects and fluctuations, the injector was purged at a flow rate of 200 ml/min for 30 seconds and the flow rate of that condition for 10 seconds before beginning the measurement period.

In addition to the particle sizing data, a high-resolution CMOS camera was used to record still images of the spray pattern of each test condition. These stills were then utilized for qualitative evaluation of the patterns of each condition.

Nonreactive TR-PIV testing was conducted utilizing a Dantec Speedsense high-speed dual-frame CCD camera at a resolution of 800x800 pixels and a spatial resolution of 82 pixels/mm^2 over a region of 80x80 mm along the central plane of the injector and chamber. Illumination was provided by a 527 nm Litron Nd:YLF laser system, coupled with sheet formation optics, triggered at a rate of 5000 Hz for 1 second. To separate illuminated seeding particles from the background a per-pixel minimum value was determined across all captured images for each frame which was subtracted

from each captured image pair, after which dewarping was conducted on each frame utilizing pre-calibrated array image taken prior to testing. An adaptive PIV algorithm was then employed to establish the vector map of each captured frame pair, with a final interrogation area of 32x32 pixels. While interrogation area overlap varied between individual cells due to the processes of this algorithm, an average overlap value of 25% between neighboring cells was maintained. The maximum displacement of seeding particles was limited to 8 pixels. The full-scale accuracy of the velocity measurement was calculated utilizing the following function:[20]

$$\delta = \frac{\sigma_d}{d} \qquad (1)$$

where δ is the full-scale accuracy of the measurement, σ_d is the discriminative minimum displacement, and d is the maximum displacement of the particles within any given subregion. The discriminative minimum displacement was assumed to be 0.1 pixels[21], resulting in a full-scale accuracy of 1.25% in both the axial and radial directions. Once the vector maps were constructed for each image pair, all 5000 vector maps were averaged to form the mean velocity vector map for the flow. The final contours were then formed via a 2D Delaunay meshing algorithm utilizing the mean vector map as an input.

Airflow was delivered and controlled by the sonic nozzle bench; and seeding was provided by the fluidized bed seeder. Conditions A1–A5 were utilized for this nonreacting test series as found in Table 2 below. The axial dimension (y) and radial dimension (x) were normalized by the interior throat dimension D=27 mm, while flow velocities were normalized by the mean axial velocity for each case, $\dot{m}/(\rho A_t)$, based on the corresponding air mass flow rate ($\dot{m}$) and the interior throat area of the swirler-injector assembly, A_t. Table 2 also lists the air mass flow rate and the mean axial velocity for each case.

Table 2: Air Flow Conditions			
Condition	Percent Air Pressure Drop	Air Mass Flow Rate (g/s)	Mean Axial Velocity (m/s)
A1	1.5	10.9	16.10
A2	2.0	11.67	17.23
A3	2.5	12.97	19.15
A4	3.0	15.3	22.59
A5	4.0	18.0	26.58

Reactive TR-PIV testing was conducted utilizing a Dantec Speedsense high-speed dual-frame CCD Litron Nd:YLF laser in the same way as previous non-reactive testing with the exception of the measurement repetition rate. These experiments utilized a 1000 Hz repetition rate, with data being collected over the course of 3 seconds. All contours constructed in the same way as the non-reactive PIV series with the difference of the use of 3000 images rather than 5000. All testing was conducted utilizing fuel flow rate conditions of F1, F3, F4, and F5 listed in Table 6 at 3% pressure drop. It should be noted that the fuel flow rate condition of F2 was omitted due to the lack of significant differences in spray performance between Conditions F1 and F2. The global equivalence ratio value (φ) of each reacting condition, as well as the air mass flow rate at 3% pressure drop during experiments and the mean axial velocity used for velocity normalization, can be found in Table 3 below.

Table 3: Reactive PIV Conditions				
Condition	Fuel Volumetric Flow Rate (ml/min)	Air Mass Flow Rate (g/s)	Global φ at 3% Pressure Drop	Air Mean Axial Velocity (m/s)
F1	165	17.45	1.78	25.63
F3	149		1.62	
F4	110		1.19	
F5	80		0.88	

Adhesion of wetted seeding particles to the chamber wall was an issue in reactive TR-PIV, causing areas of obscuration of the seeding particles, and could not be completely prevented. Seeding

was wetted by the spray and carried to the quartz walls. To control the effects of sooting and fuel deposition each reacting test was ignited at an intermediate air flow rate of 10 g/s utilizing a kerosene torch within a steel sub-chamber. After ignition, the air flow rate was set for the given reacting condition and the sub-chamber was removed from the combustion chamber. The resulting flame was given 3 seconds to stabilize from this point before TR-PIV diagnostics were initiated.

Chemiluminescence analysis of Conditions F1 and F3–F5 was conducted utilizing a Thorlabs DCU224C color CCD camera at a resolution of 1280x1024 pixels and a framerate of 18 fps. Each condition was ignited and stabilized, and still frames were recorded for 4 seconds in each test. Each still frame was recorded as the 8-bit hardware intensity value and collected into an Audio Video Interleave (AVI) container. The AVI containers for each condition were separated by MATLAB back into individual frames. A threshold-type background subtraction was then used to isolate the chemiluminescence signature of each frame. In this method the value of the background pixel with the highest intensity was manually determined and set as a threshold. Each pixel of each individual frame was compared against this threshold, and was set to a value of zero if it was found to be of lower intensity than the threshold. Once this was completed the entire set of still frames were averaged together a single image, with the plotted color of each pixel being determined by its intensity relative to the highest intensity value within the image.[22] The bandpass filters used to dictate the detection wavelength range for the measurement of each species can be found in Table 4[9,23].

Table 4: Filter Specifications

Detected Species	Central Wavelength (nm)	Total Bandgap (nm)
OH*	320	80
CH*	430	20
NO_2*	850	20

Visible spectrum analysis of Conditions F1–F5 was conducted utilizing the same Thorlabs DCU224C color CCD camera utilized in the chemiluminescent testing at a framerate of 30 fps. Each

condition was ignited and stabilized, and still frames were recorded for 6 seconds in each test. Each still frame was recorded as a 3x8-bit image and collected into an AVI container. The AVI containers for each condition were separated by MATLAB back into individual frames and further split these frames into the RGB components of each pixel. These stills were averaged together on a per-value-per-pixel basis to form a singular matrix, after which a time-resolved minimum per-value-per-pixel background subtraction method was employed. The resulting matrix was then plotted a true color 3x8-bit composite image.[22]

PLIF analysis was conducted for formaldehyde on the reacting flows. A 355 nm Nd:YAG laser was used to excite the flow at a repetition rate of 10 Hz and energy output of 50 mJ per pulse. Planar converging and diverging UV lenses were utilized to form a 26 mm tall laser sheet. A Princeton Instruments PI-MAX 3 1024x256 pixels ICCD camera was utilized at a gain value of 20, gate value of 80 ns, and delay of 27 ns combined with a UV-Nikkor 105mm lens and a 410-490nm bandpass filter to record the resulting emittance spectrum[24-29].

Before each PLIF measurement, the PI-MAX 3 camera was utilized to record a background reading of the reacting flow. In these cases the flame would be ignited, allowed to reach the desired operating condition, and the PI-MAX 3 would begin recording; however the laser would not be used to excite the flow. Once this background test had been completed two trials were taken with the laser exciting the flow so as to capture the PLIF emittance. In each of these tests 100 still images were recorded, each in the form of a 16-bit raw pixel intensity matrix collected into a SPE container. Due to the laser sheet height being smaller than the measurement area this process was repeated at three additional axial laser sheet locations.

Once the testing had been completed, the SPE files of each axial plane of each testing condition were read into MATLAB, split into their component frame pixel matrices, and averaged into two PLIF matrixes and a background matrix. The background matrix was then subtracted from

the PLIF matrixes, and the PLIF matrixes were then averaged together into a single matrix. A threshold type noise subtraction method was then conducted in the same way as was done previously in chemiluminescence testing and the plane was converted into an 8-bit intensity matrix. This process was then repeated for the other three axial measurement planes of each test condition. Once completed, the four planes were plotted to a single pixel matrix and their overlapping regions were averaged together. A color bar was utilized to assign each pixel a color based on its intensity relative to the highest intensity pixel within the matrix, thus resulting in a single 8-bit image.

PLIF measurement of hydroxyl radical (OH) was conducted along the centerline of the injector utilizing an excitation wavelength of 282.97 nm at 10 Hz and 10mJ per pulse via a tunable dye laser (Continuum ND6000) with Rhodamine-590 dye pumped by a Nd:YAG laser (Continuum Powerlite 8010) [24,27,39,30]. This OH excitation scheme was in the band of $X^2\Pi \rightarrow A^2\Sigma^+$ electronic transition. A laser sheet height of 32.4 mm was utilized, and the nominal sheet width was 0.75 mm. A PI-MAX 3 ICCD camera was utilized in conjunction with a UV-Nikkor 105mm lens and a 310±5 nm filter to capture both the background and the OH PLIF signal. The working resolution of this camera was 558x256 pixels, resulting in a spatial resolution of 0.127 mm/pixel. Images were captured as single 16-bit accumulations over the course of 10 seconds at 10 Hz, after which all 100 captured imaged were saved as a single SPE file. For each reactive condition, tabulated in Table 6, measurements were taken at two axial locations as was done with the previous CH_2O PLIF testing. A schematic of the system can be found in Figure 1.

MATLAB was utilized to read and process the SPE files. Each image set was averaged on a per-pixel basis to form singular averaged images. A background subtraction method was then implemented for each captured image set based on the background chemiluminescence signal as was done in the previous CH_2O PLIF testing so as to isolate the PLIF signal. The individual images were then mapped to the corresponding axial locations of their respective test conditions and colors were assigned to each pixel based on the ratio between that pixel's intensity and a manually set constant.

Chapter III: Determination of Swirler Experimental Effective Area

To determine the effective area, or ACd value, of the swirler experimentally, an OMEGA PX303 pressure transducer built into the air plenum was used to determine the ambient air pressure with an error value of 0.7 bar. Once this value was determined, known volumetric flow rates of air were supplied to the swirler assembly from the sonic nozzles, and the resulting pressure within the air plenum was recorded for each flow rate utilizing the same pressure transducer. The following equation was then utilized to calculate the percent pressure drop across the swirler:

$$Percent\ pressure\ drop = \frac{P_i - P_{amb}}{P_i} \times 100 \qquad (2)$$

where P_i represents the pressure within the air plenum and P_{amb} represents the ambient air pressure. Pressure measurements were taken at multiple percent pressure drop values so as to ensure that the calculated ACd value would be independent of pressure drop. Each time the swirler assembly was dismounted and remounted it was checked for leaks so as to avoid any deviances due to leaks or improper mounting.

Once the pressure values were recorded for each trial, the following equations were utilized to determine the ACd for each trial:

$$\frac{\rho v^2}{2} = P_i - P_{amb} \qquad (3)$$

$$\dot{m} = \rho \dot{V} \qquad (4)$$

$$ACd = \frac{\dot{V}}{v} \qquad (5)$$

where ρ represents the ambient air density, v represents the air velocity at the throat of the swirler cup at each given flow rate, $\dot{V}$ represents the supplied volumetric flow rate, and $\dot{m}$ represents the air mass flow rate through the calibrated sonic nozzles of the air delivery system. The results of this analysis can be found in Table 5. The individual trials were then averaged to form the experimental ACd value of 180.99±9.05 mm^2.

Table 5: Swirler Assembly ACd Results			
Trial	Percent Pressure Drop	Volumetric Flow Rate (L/s)	ACd (mm^2)
1	2.92	12.77	181.99
2	2.99	12.93	182.11
3	3.02	13	182.01
4	1.61	9.35	180.96
5	1.55	9.19	181.09
6	1.66	9.51	180.95
7	1.72	9.67	181.48
8	1.72	9.69	181.48
9	1.78	9.88	181.43
10	3.05	13.01	181.57
11	3.08	13.07	181.56
12	3.15	13.22	181.37
13	3.15	13.51	181.21
14	3.22	13.33	180.75
15	3.16	13.19	180.57
16	3.22	13.21	179.28
17	3.22	13.24	179.66
18	3.19	13.09	178.43
		Average ACd:	180.99

Chapter IV: Spray Testing

Table 6 lists the experimental Conditions F1-F5 and the droplet size distribution of these conditions in terms of the Sauter mean diameter (SMD) and percentile droplet sizes. The SMD can be calculated from a given spray of known size distribution using equation:[31]

$$SMD = \frac{\sum N_i {D_i}^3}{\sum N_i {D_i}^2} \qquad (6)$$

Where N_i is the number of particles in the spray of a given size and D_i is the mean diameter of that set of particles. As can be seen in Table 6, the Sauter mean diameter (SMD), the size of a droplet with the same volume to surface area ratio as the spray itself, decreases as the fuel flow rate increases. This in turn means that the absolute surface area of the spray decreases at a higher order than the fuel flow rate. From a combustion standpoint this is important as the evaporation of liquid fuel to the combustible gaseous phase occurs on this interface surface, and a decrease in the area of the interface can be assumed to result in a decrease in the rate of evaporation of the fuel.

This trend was also found in the percentile droplet sizes of d10, d50, and d90, each being the representative droplet size such that only a given percentage of smaller droplets exist within the spray. Even so, Conditions F1-F3 all displayed similar particle size values in all categories, despite their differences in volumetric fuel flow rate. More precisely, between Conditions F1 and F3 a 10% increase in volumetric fuel flow rate only resulted in a 5% reduction in SMD. Qualitatively these three conditions all exhibited spray cones of similar structure, each being that of a symmetric hollow spray cone of roughly a 60-degree spray angle.

Table 6: Spray Testing Results							
	Global ϕ at 3% Pressure Drop	Volumetric Flow Rate (ml/min)	Fuel Supply Pressure (MPa)	SMD (microns)	D10 (microns)	D50 (microns)	D90 (microns)
1.87	165	0.36	54.33	31.66	76.82	163.50	
1.75	162	0.34	53.27	31.26	73.36	156.90	
1.62	149	0.28	57.19	34.34	77.66	161.50	
1.19	110	0.15	98.95	58.93	144.60	285.60	
0.88	80	0.08	266.30	164.00	353.30	671.30	

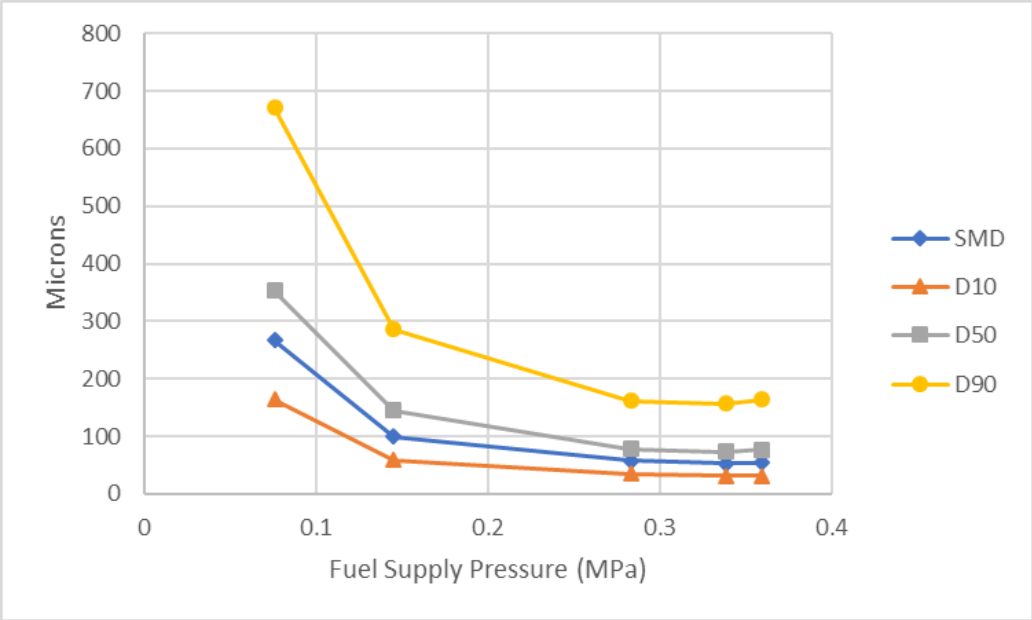

Figure 5: Spray Droplet Size vs Fuel Supply Pressure

The severe differences between the droplet size values of Conditions F3 and F4 was accompanied by a slight change in the spray cone angle, the cone narrowing to roughly a 45-degree spray angle. Between Conditions F4 and F5 however, the spray pattern changed dramatically. Whereas the other conditions exhibited either 'tulip'[31] or 'fully-developed' spray structures, the spray structure at Condition F5 was of the 'onion' type[31]. The breakup region of this structure was located immediately before the axial location of the Malvern measurement. This breakup region was not hollow, and the spray was not symmetrical with respect to the injection axis. This difference in spray

structure between Conditions F1-F3 and F4/F5 was likely due to the difference in fuel supply pressure as similar behavior has been documented previously in pressure-swirl nozzles in which atomization quality will increase with respect to an increase in fuel pressure up to a certain pressure value, beyond which point the atomization quality becomes constant[19].

Chapter V: Time-Resolved Particle Imaging Velocimetry under Nonreacting Conditions

Figures 6 and 7 plot the normalized mean axial velocity fields for the nonreacting conditions of A1 and A4, while Figures 8 and 9 show the normalized mean radial velocity fields. Trials of Conditions A2, A3, and A5 were taken and can be found in Appendix A. Figures 10-15 further compare the radial profiles of normalized mean radial velocity and normalized mean axial velocity for Conditions A1–A5 at four different axial locations, namely y/D=0.28, 1.24, 2.05, and 2.93.

As can be seen in Figures 6-9, the airflow of the swirler-injector assembly maintained a consistent structure in terms of both normalized mean velocity and flow shape across all tested conditions. This can clearly be seen in the isolated velocity profiles at y/D=0.28, as shown in Figures 10 and 11. The largest deviances between testing cases were found within the outer 10% of the radial domain in either direction, in the high velocity regions close to the confinement wall suggesting interference between the chamber wall and the airflow.

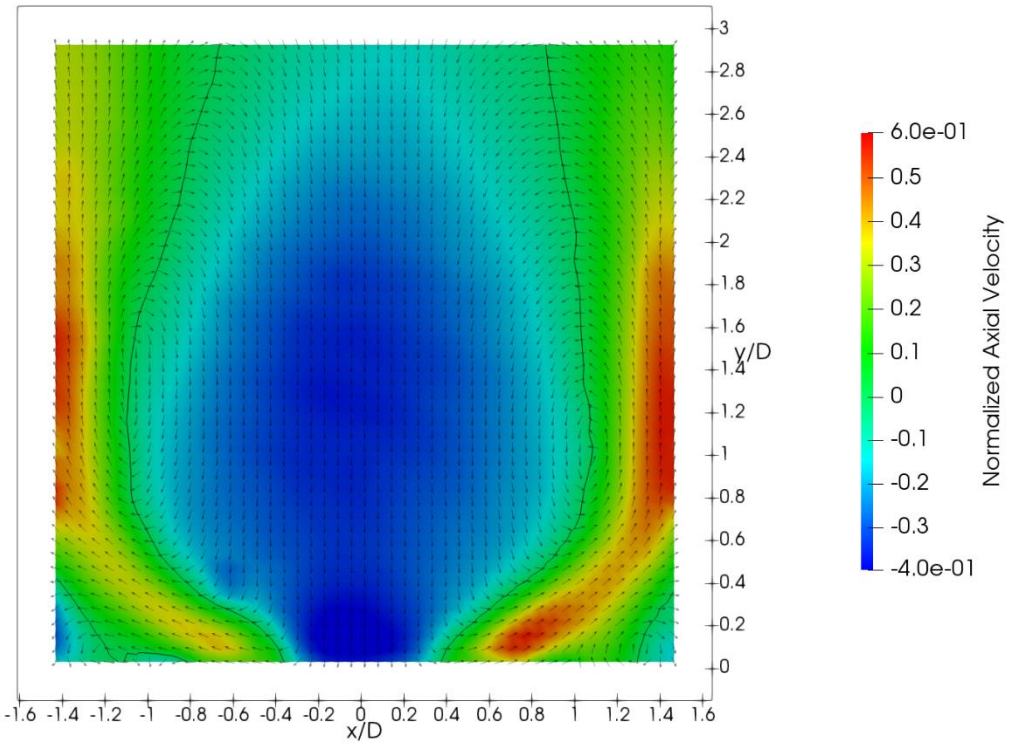

Figure 6: Normalized mean axial velocity mapping at Condition A1. Black line indicates contour of zero axial velocity.

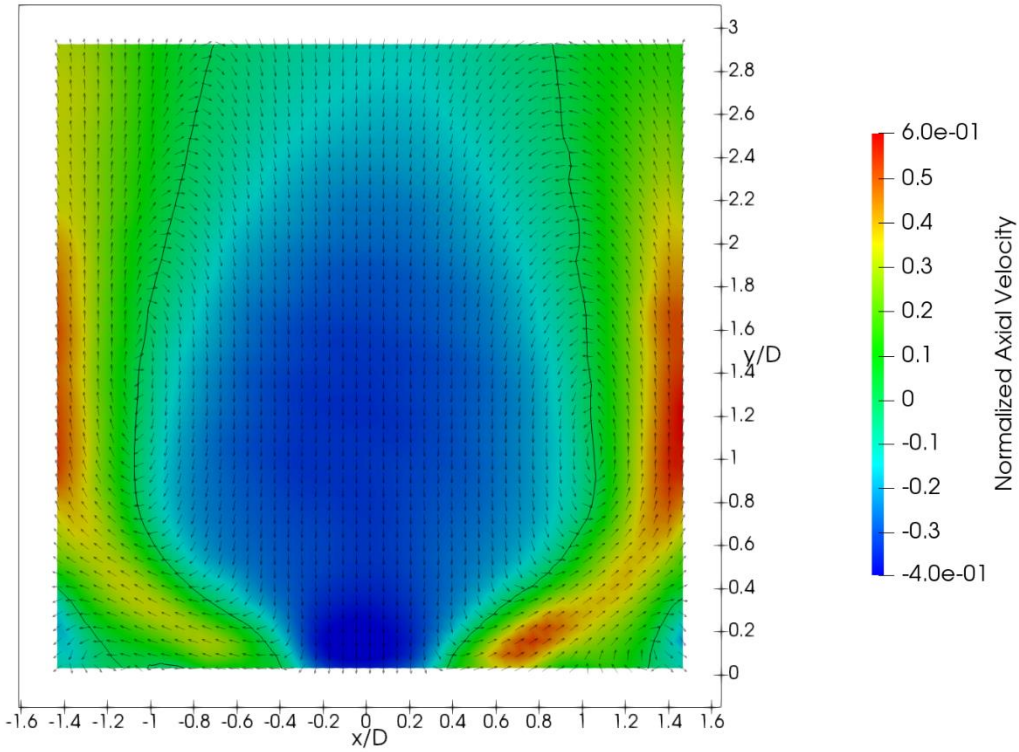

Figure 7: Normalized mean axial velocity mapping at Condition A4. Black line indicates contour of zero axial velocity.

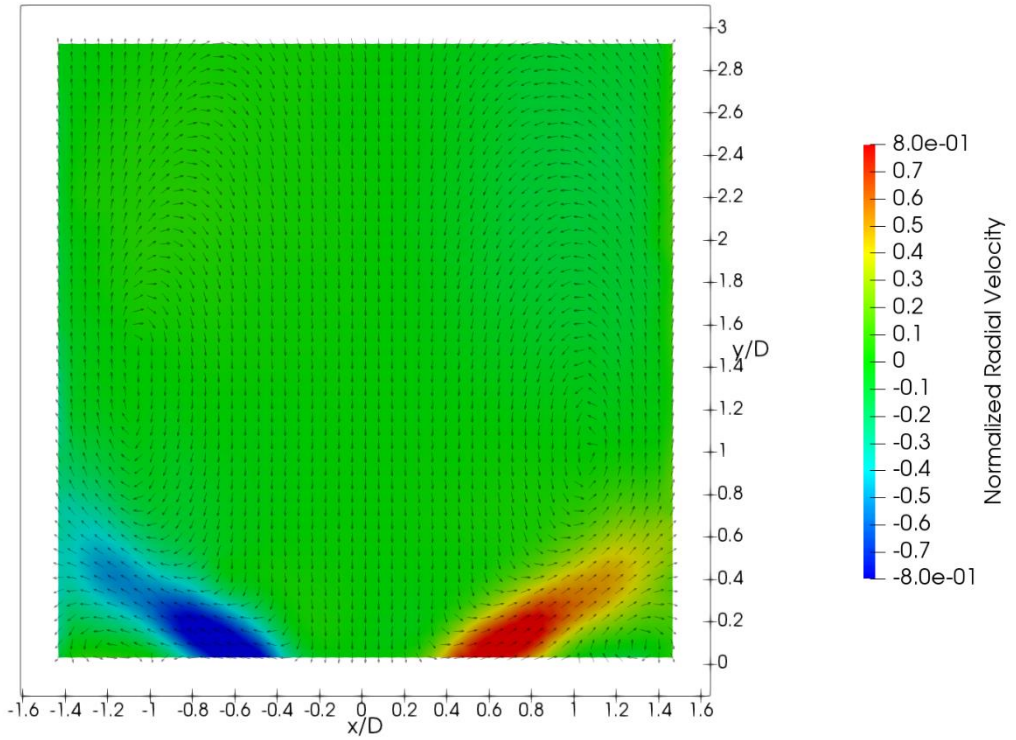

Figure 8: Normalized mean radial velocity mapping at Condition A1.

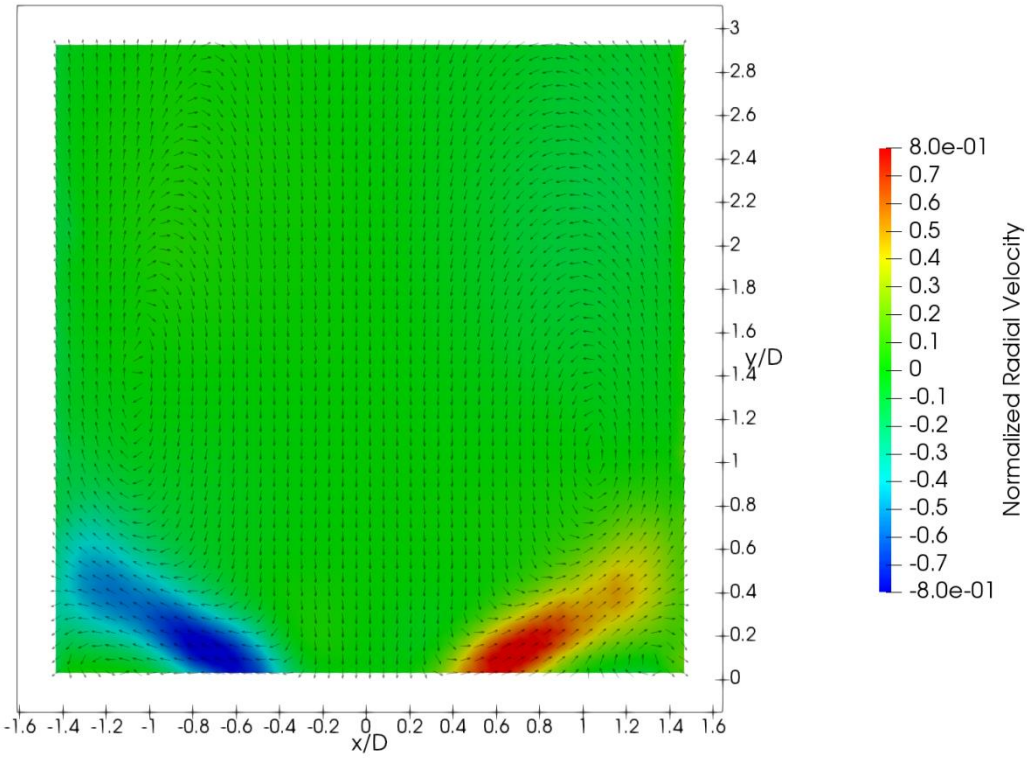

Figure 9: Normalized mean radial velocity mapping at Condition A4.

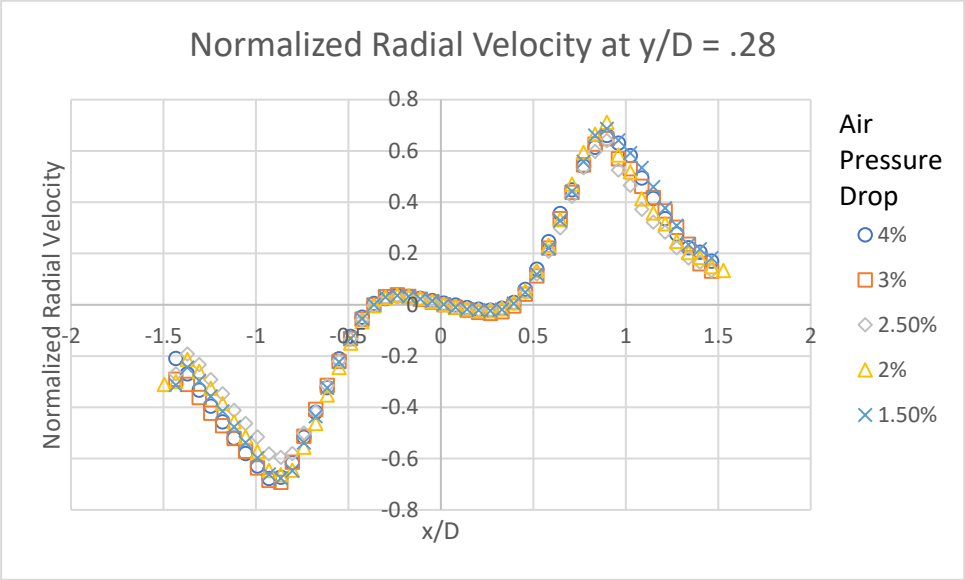

Figure 10: Comparison of radial profiles of normalized mean radial velocity for all pressure drop conditions at y/D=0.28.

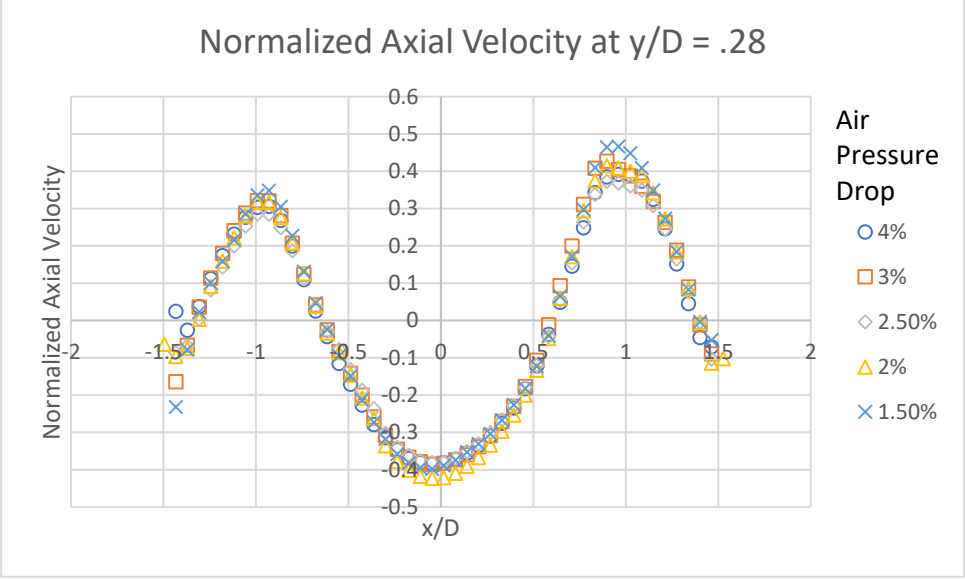

Figure 11: Comparison of axial profiles of normalized mean axial velocity for all pressure drop conditions at y/D=0.28.

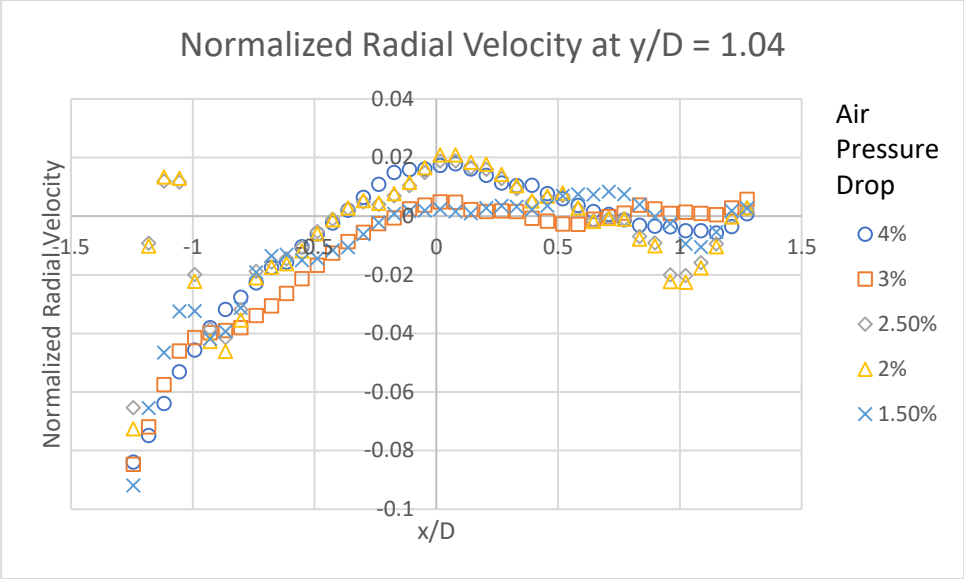

Figure 12: Comparison of radial profiles of normalized mean radial velocity for all pressure drop conditions at y/D=1.04.

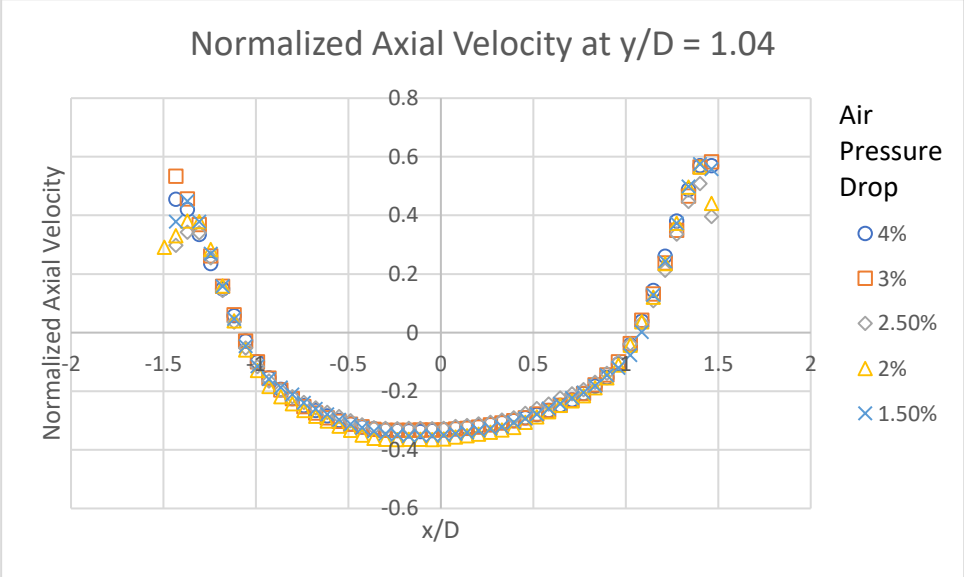

Figure 13: Comparison of axial profiles of normalized mean axial velocity for all pressure drop conditions at y/D=1.04.

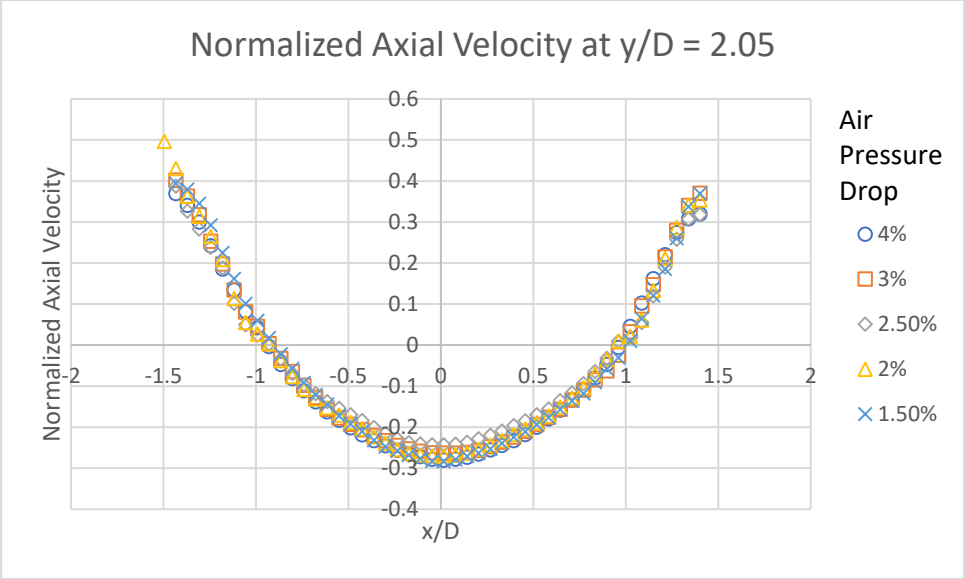

Figure 14: Comparison of axial profiles of normalized mean axial velocity for all pressure drop conditions at y/D=2.05.

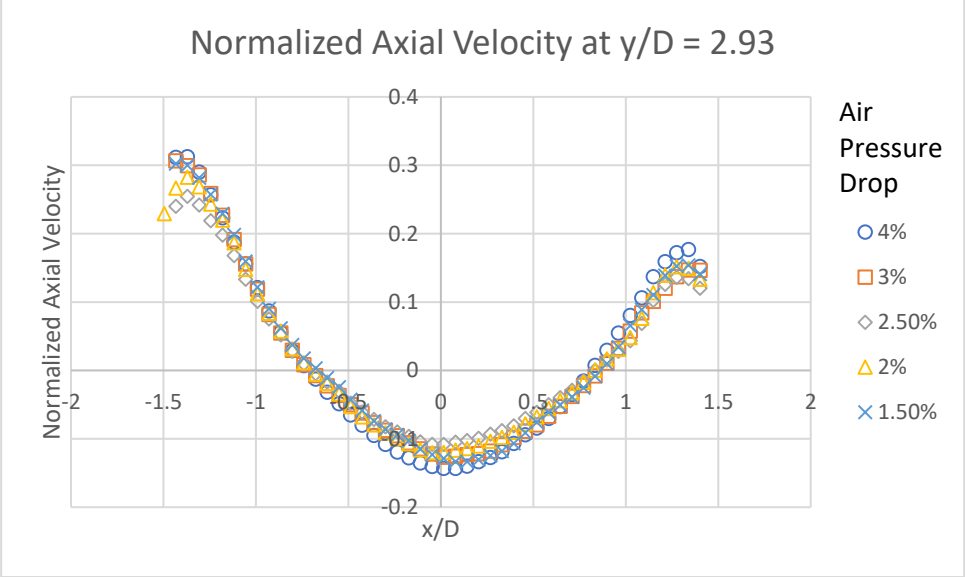

Figure 15: Comparison of axial profiles of normalized mean axial velocity for all pressure drop conditions at y/D=2.93.

As can be seen in Figures 6 and 7, the mean axial velocity profiles downstream of the injection plane do not maintain a high degree of symmetry. While the axial and radial profiles near the swirler-injector assembly exit (e.g., *y/D*=0.28) were dominated by the swirler flow itself, and were therefore fairly symmetrical as expected, the same could not be said for the profiles at further

downstream. In all succeeding axial locations shown here, i.e. y/D=1.04, 2.05, and 2.93, there was a high degree of deviance between radial points and testing conditions in terms of normalized mean radial velocity.

The radial velocity profile at y/D=1.04 displayed two interesting characteristics. First, the degree of agreement between the various tested pressure drop conditions was far lower than that of the axial profiles. This suggests that the normalization utilized, being that of a mean axial velocity, may not have been appropriate for application to the radial velocity. The second phenomenon displayed in this profile was a change in sign of the radial velocity for the A2 and A3 conditions at points along the negative radial direction. It was found that these two conditions exhibited recirculating vortices located at a slightly lower axial location than the other conditions, placing the center of each vortex below the profile location, thus resulting in this change in sign.

Despite the asymmetry present in the mean velocity profiles, the overall structure of the flow field, specifically the location, shape, and length of the recirculation zone, was relatively constant between testing cases. This can clearly be seen in Figures 16 and 17, comparing the conditions of A1 and A5 respectively to the design condition of A4, defined by the manufacturer of the swirler, in terms of normalized mean axial velocity. These three conditions represent the widest range of tested percent pressure drop values across the swirler, and yet the composite of the recirculation zones of the two cases in each comparison displays a high degree of symmetry.

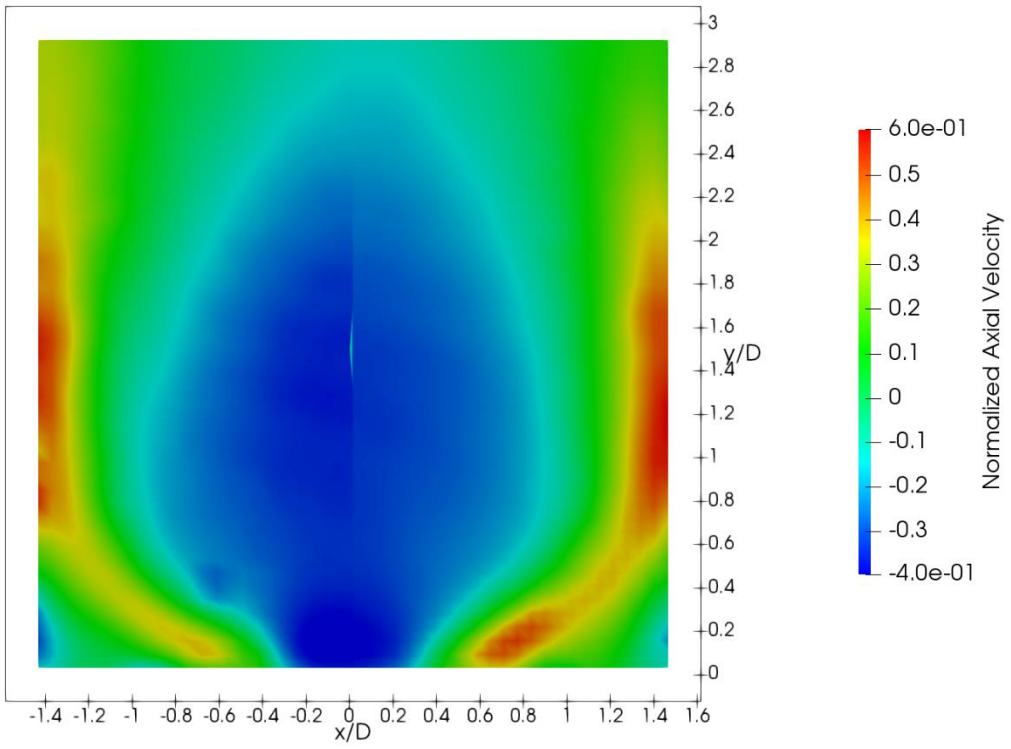

Figure 16: Normalized mean axial velocity comparison at Conditions A1 (left) and A4 (right).

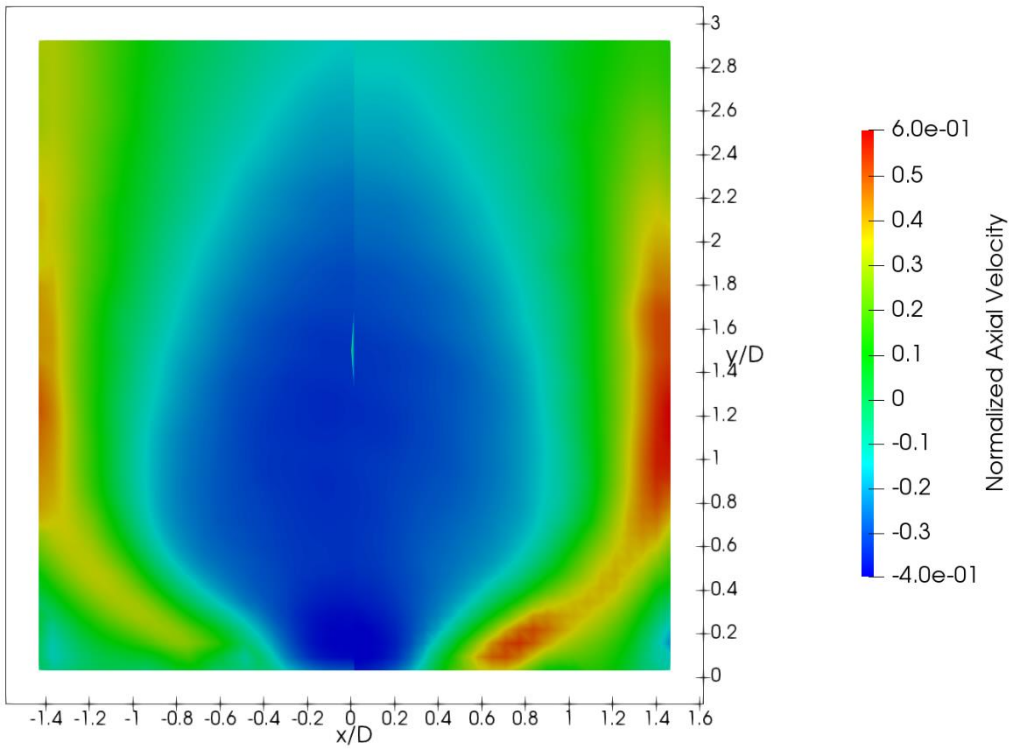

Figure 17: Normalized mean axial velocity comparisons at Conditions A5 (left) and A4 (right).

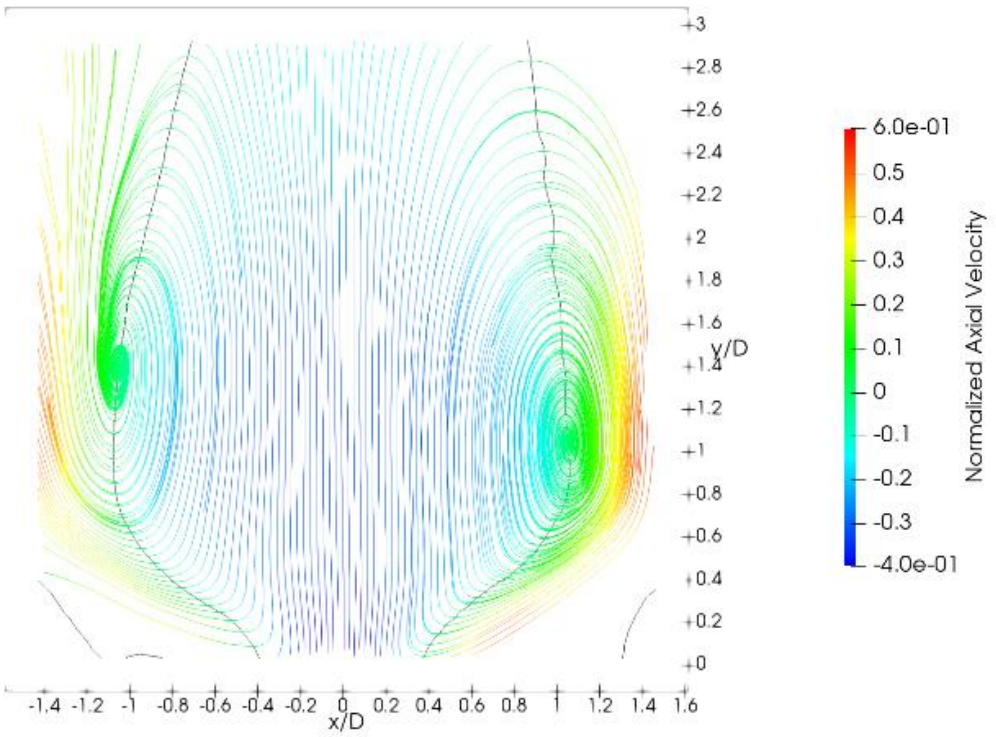

Figure 18: Streamlines and normalized mean axial velocity of Condition A4. Black line indicates contour of zero axial velocity.

In an effort to uncover the cause of the asymmetry present in the axial locations of the two recirculating vortices additional PIV trials were taken at various radial location as list in Table 7 below.

Table 7: Radial Plane Locations		
Location	Distance from Centerline	
	mm	D
V1	0	0.00
V2	-5	-0.19
V3	-20	-0.74
V4	-25	-0.93
V5	-35	-1.30
V6	5	0.19
V7	20	0.74
V8	25	0.93
V9	35	1.30

Trials were taken at Conditions A2, A4, and A5 at each location. The radial and axial velocity plots for Condition A4 at locations V1, V4, and V8 can be found in Figures 19-23 below. All other plots can be found in Appendix B. It should be noted that the injector and swirler assemblies were dismounted, cleaned, and remounted to the plenum before this test series began, thus changing both the swirler rotational orientation and the concentricity of the assembly due to mounting tolerances.

As can be seen in Figures 19-23, the axial and radial velocity structures at locations V4 and V8 were very similar to each other, though mirrored across the injection axis, indicating a general degree of symmetry of the flow with respect to the injection axis. While all other locational pairs mirrored this trend, these locations were of particular interest in that they were located in the same radial region as the vortices of the central recirculating zone. In particular it was found that while the radial velocities and overall flow structures at these locations were similar, the axial velocities in the area around the recirculating zone were found to be slightly higher in magnitude at location V4 than at location V8.

At location V1, the central plane, the central recirculating zone was not symmetrical close to the injection plane. Specifically the lower bound of the recirculating zone defined by the black zero axial velocity line was located axially higher at all negative radial point than the positive radial points. The axial velocity was also slightly higher at these negative radial points than the positive radial points. As this region was located directly after the swirler assembly, this velocity asymmetry was attributed to the asymmetrical swirler area along the radial axis caused by the slight inconcentricity and rotation of the swirler assembly mounting. It was conjectured that the momentum interaction between this axial velocity asymmetry and the flow within the recirculating region was the cause of the asymmetrical recirculating zone close to the injection axis.

As the recirculating vortex of the negative radial direction was located at a much lower axial point than that of the positive radial direction it was further conjectured that the increased axial velocity in the negative radial direction close to both the wall and the central recirculating zone altered the rotational interaction between the wall and the vortex, thus forcing the vortex to a lower axial location.[22] As the current PIV data in the region of the wall could not be collected due to laser sheet scattering, and the existing PIV data is only 2D in nature further investigation would be required to establish the definite cause of the asymmetry in vortex location.

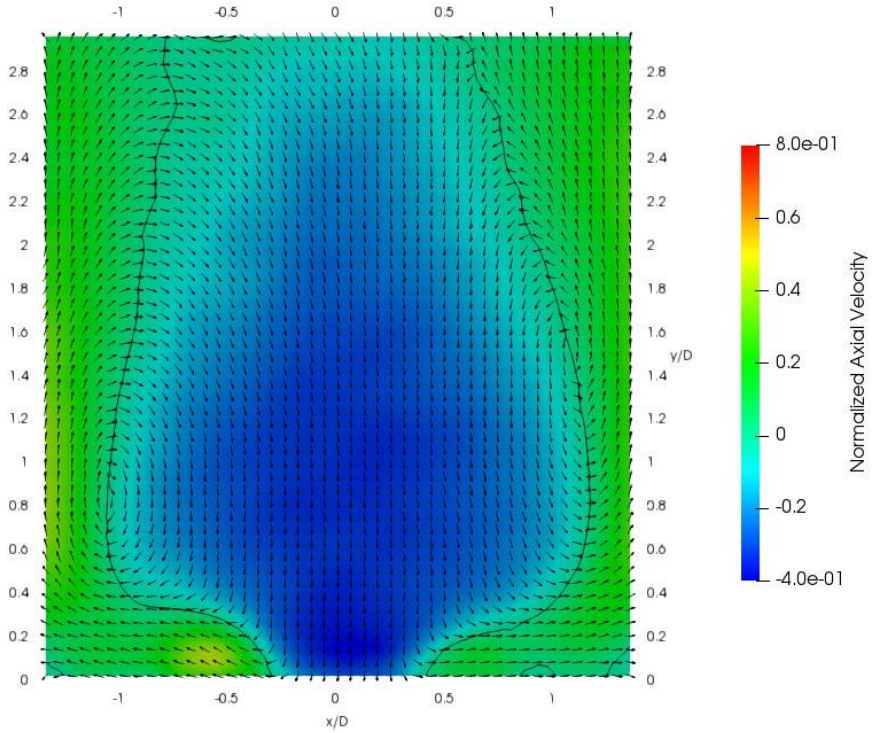

Figure 19: Axial velocity profile at Condition A4, location V1. Black line indicates contour of zero axial velocity.

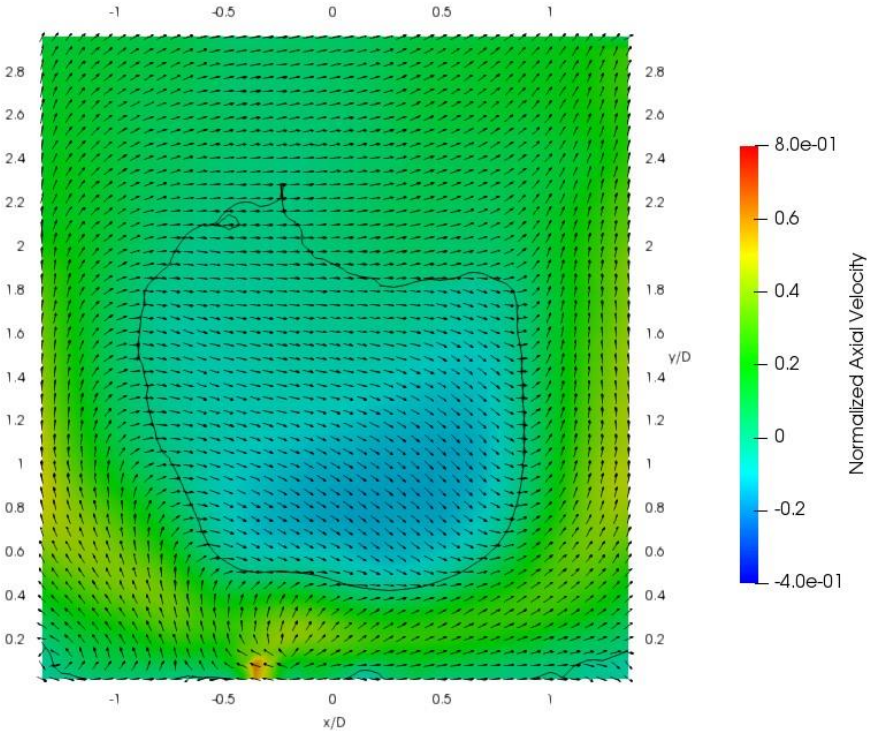

Figure 20: Axial velocity profile at Condition A4, location V4. Black line indicates contour of zero axial velocity.

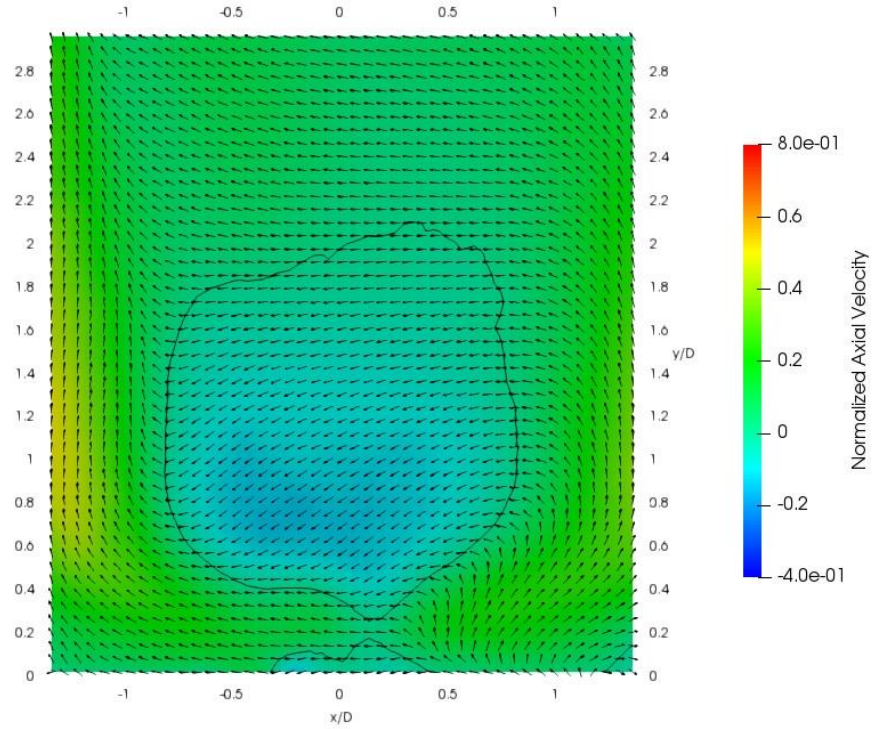

Figure 21: Axial velocity profile at Condition A4, location V8. Black line indicates contour of zero axial velocity.

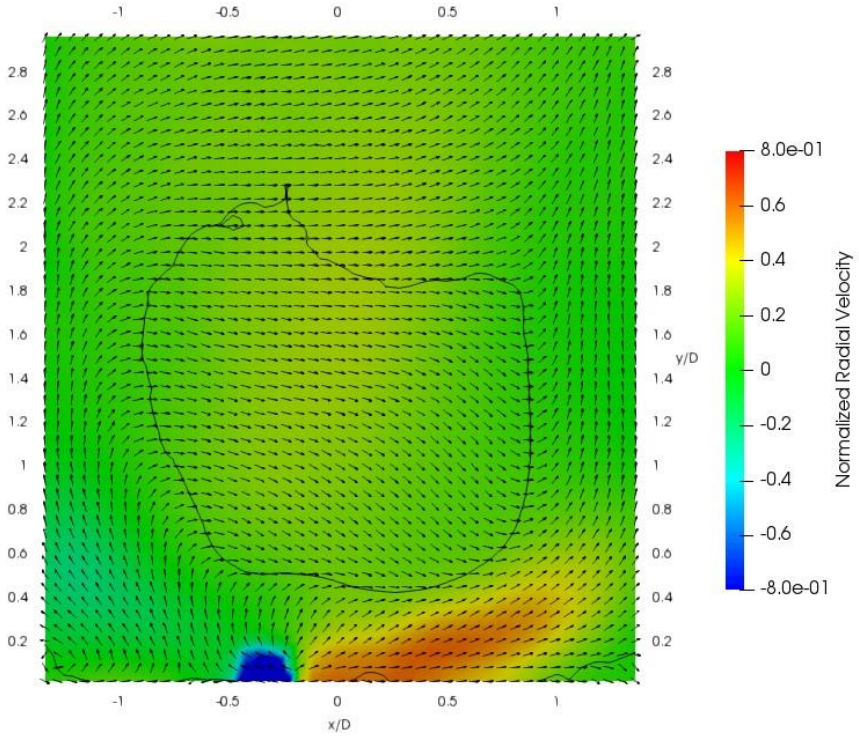

Figure 22: Radial velocity profile at Condition A4, location V4. Black line indicates contour of zero axial velocity.

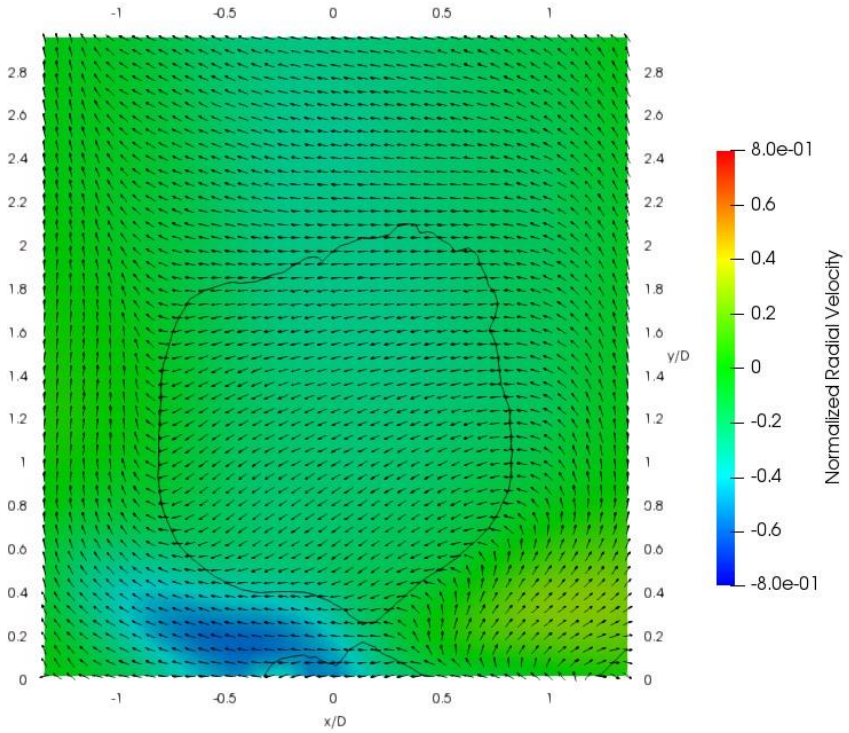

Figure 23: Radial velocity profile at Condition A4, location V8. Black line indicates contour of zero axial velocity.

Figures 24 and 25 show the experimental turbulent kinetic energy (TKE) distributions for Conditions A1 and A3 as calculated utilizing equation (7).

$$TKE = \frac{1}{2}\left({u'_{RMS}}^2 + {v'_{RMS}}^2\right) \qquad (7)$$

Figures 26-29 plot the distributions of root-mean-square (RMS) axial velocity fluctuations (v'_{RMS}) for Conditions A1 and A3, while Figures 35–39 plot those of RMS radial velocity fluctuations (u'_{RMS}) as calculated utilizing equations (8) and (9).

$$u'_{RMS} = \sqrt{\frac{1}{n}\sum_{i=1}^{n}(u'_i)^2} \qquad (8)$$

$$v'_{RMS} = \sqrt{\frac{1}{n}\sum_{i=1}^{n}(u'_i)^2} \qquad (9)$$

As can be seen from Figures 26–40, the turbulent kinetic energy profile, as well as the component axial and radial fluctuation velocity profiles, maintained consistent structures across all tested conditions. All of these profiles exhibited symmetry with respect to the injection axis downstream of the centroids of the recirculating vortices. Near the injection plane however, the positive radial direction exhibited values higher than the negative radial direction in all cases at all points along the axial direction.

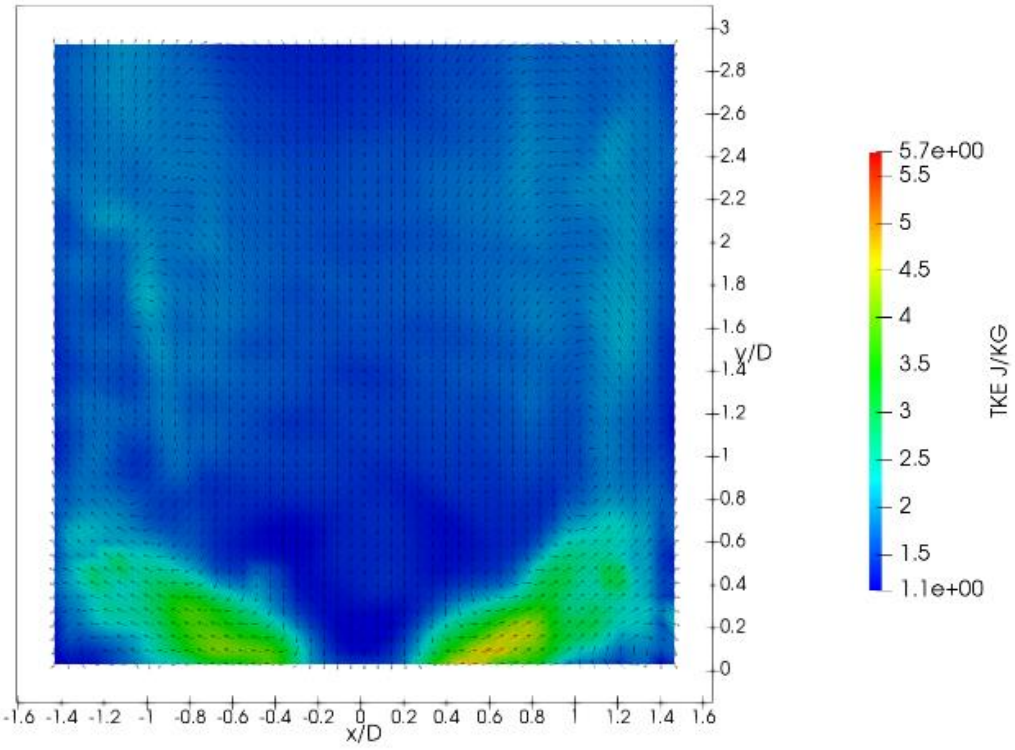

Figure 24: Turbulent kinetic energy mapping of Condition A1.

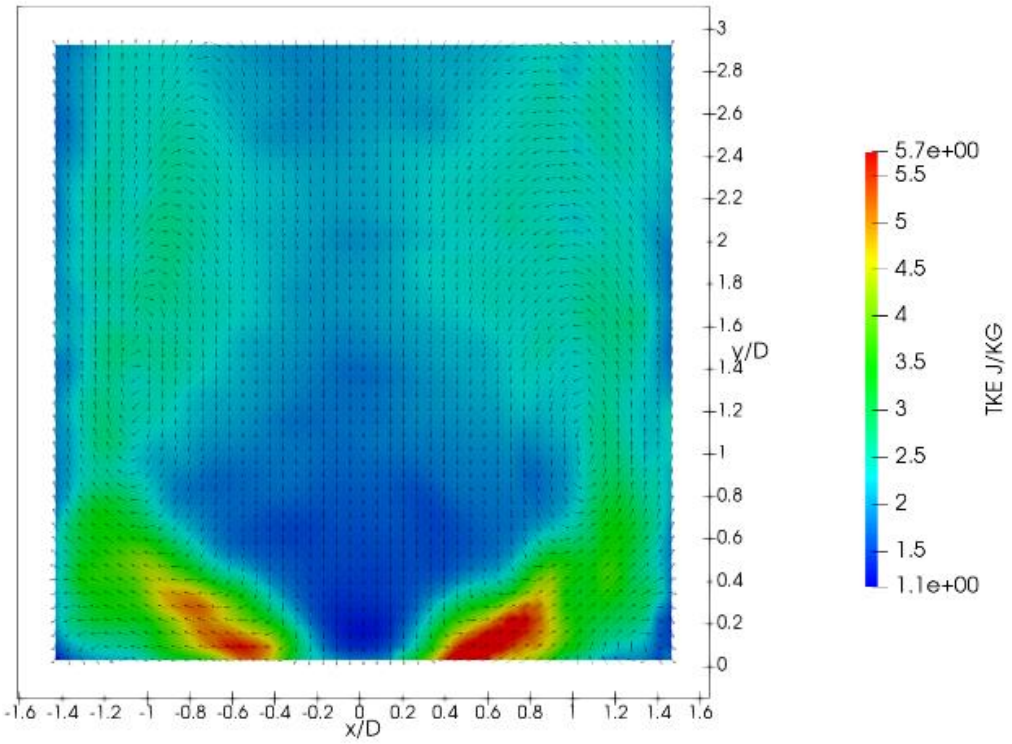

Figure 25: Turbulent kinetic energy mapping of Condition A4.

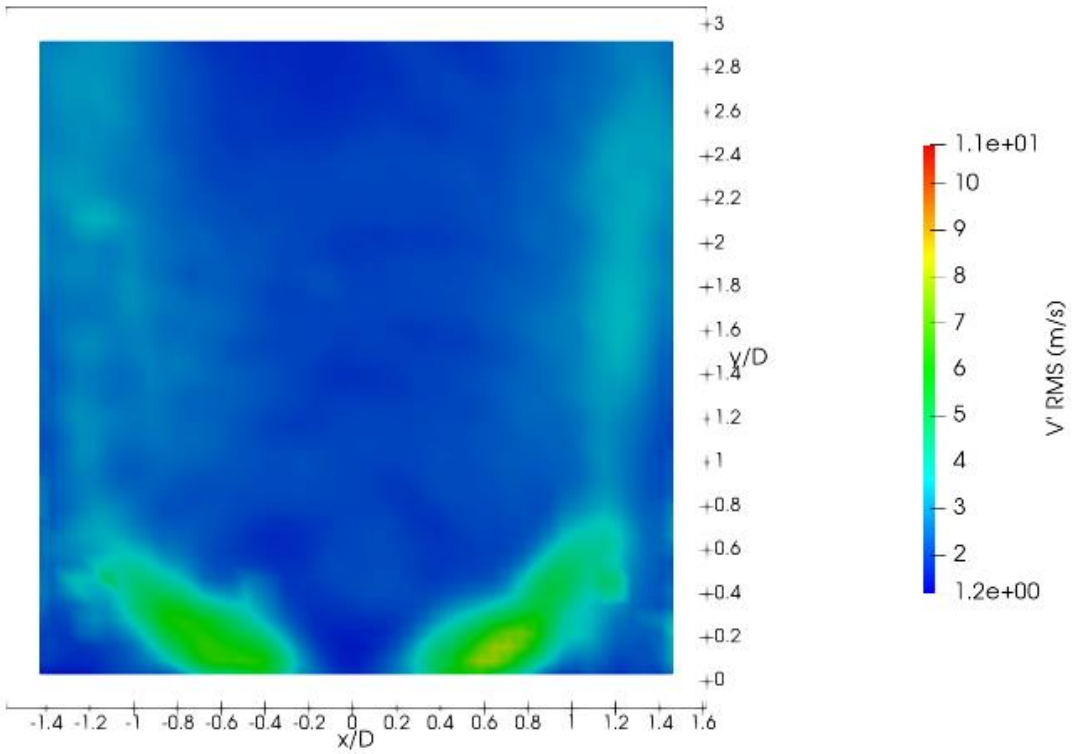

Figure 26: Mapping of root-mean-square of axial velocity fluctuations at Condition A1.

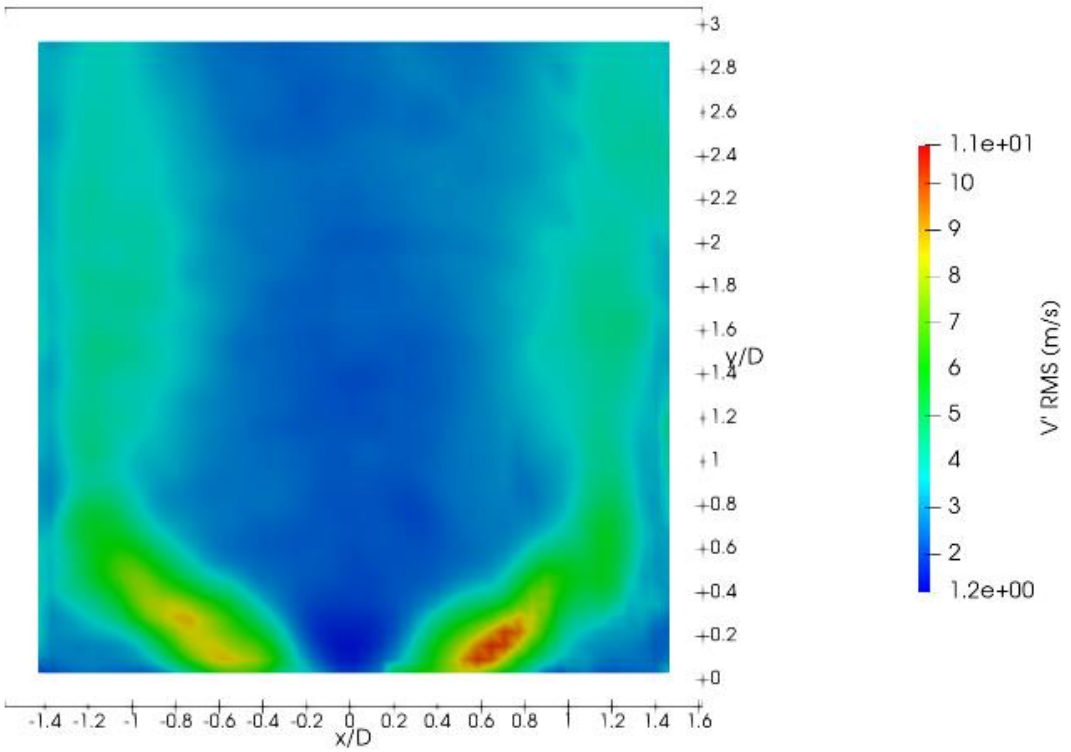

Figure 27: Mapping of root-mean-square of axial velocity fluctuations at Condition A4.

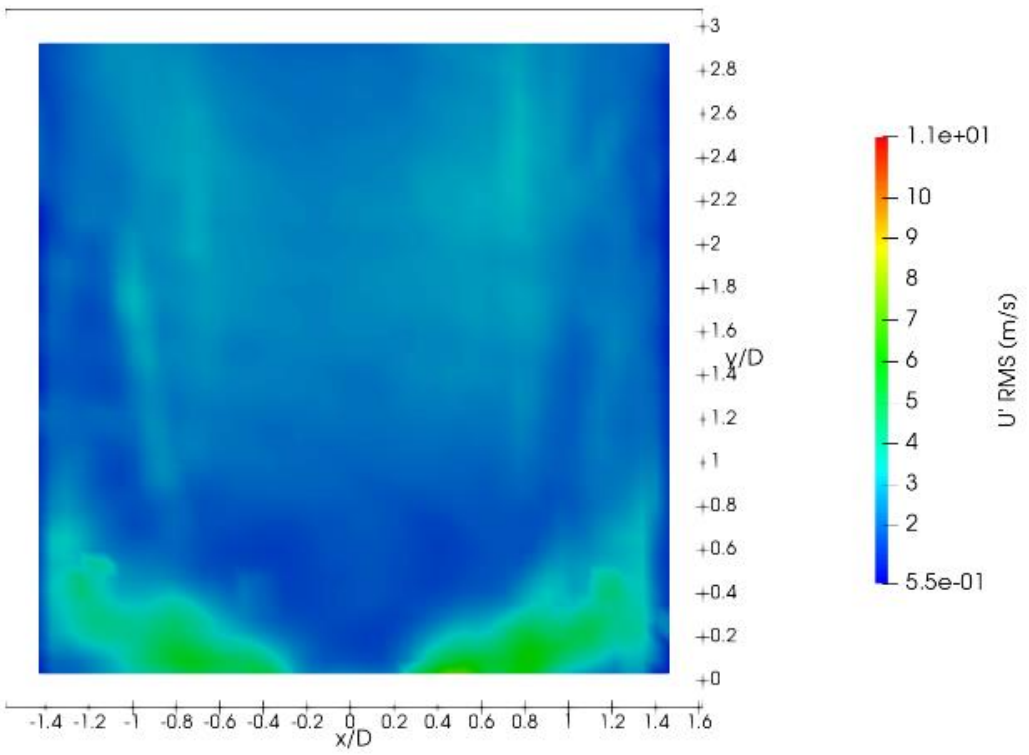

Figure 28: Mapping of root-mean-square of radial velocity fluctuations at Condition A1.

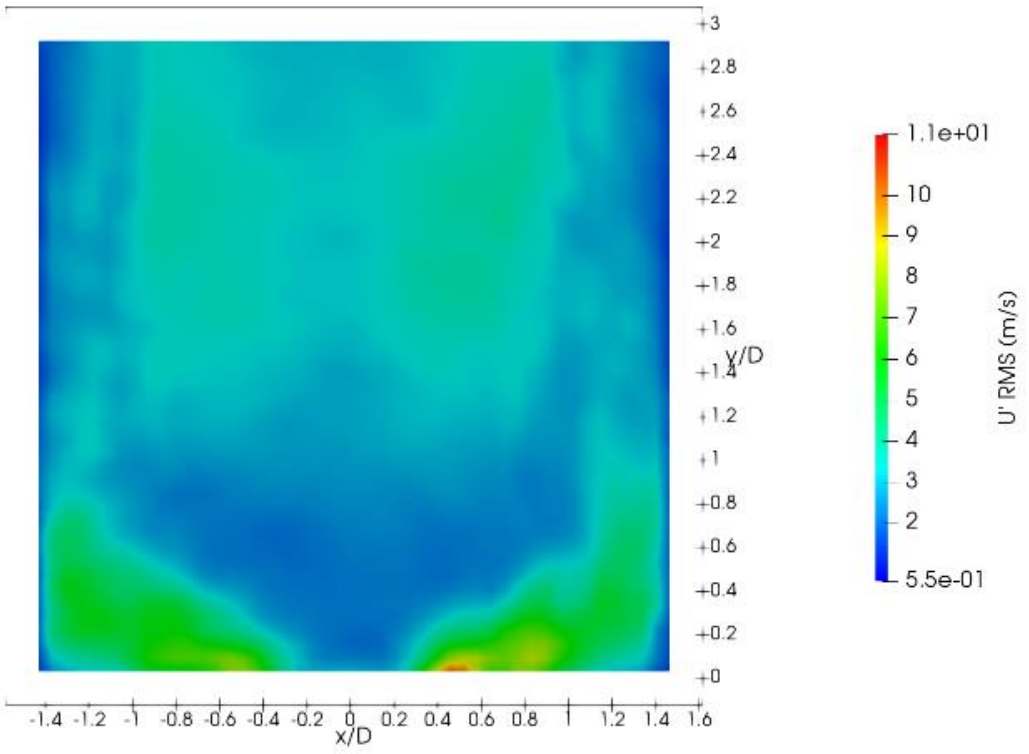

Figure 29: Mapping of root-mean-square of radial velocity fluctuations at Condition A4.

Chapter VI: Time-Resolved Particle Imaging Velocimetry under Reacting Conditions

Figures 30-33 plot the normalized mean axial velocity fields of Conditions F1, F3, and F5, respectively. As can be seen in Figures 30 and 31, the recirculating zone for the reacting cases detached from the injection plane. Crucially the farthest axial point of the recirculating zone remained unchanged compared to the TR-PIV nonreacting measurements. All reacting cases also exhibited large high velocity regions propagating outward from the primary swirler. It was noticed that large amounts of droplets were carried into this region, causing interference in the measurement due to obscuration of the seeding particles. This obscuration was produced in two ways. First, fuel droplets directly entrained seeding particles or blocked them from view of the camera, preventing these seeding particles from being tracked. Second, the fuel droplets themselves scattered a significant amount of light to the camera, thus illuminating pixels around the droplet. In some image pairs this scattering illuminated enough pixels to prevent tracking in a limited number of interrogation areas. In a small percentage of the latter case the droplets were interpreted as seeding particles themselves by the software package, resulting in incorrectly calculated vectors. These effects all reduced the fidelity of the measurement within this region.

Figures 32 and 33 further show the normalized mean radial velocity fields of Conditions F1 and F3, respectively. These figures also exhibited large high-velocity regions when compared to the nonreactive results. Despite the loss of measurement fidelity caused by droplet interference it would make physical sense for these axial and radial high velocity regions to be larger than their nonreactive counterparts due to the acceleration of the flow caused by the presence of the flame.

In addition to the loss of fidelity caused by the obscuration of seeding particles, further loss of detail was caused by the interactions of fuel particles and the solid seeding particles, leading to the formation of large ‘clumps’ of seeding media with far longer lag times than that of an individual seeding particle. This wetting interaction also reduced the seeding particle density throughout the

flow field, with the effect becoming more severe as distance from the injection plane increased due to the cumulative entrainment and wetting effects as the particles moved through the chamber. As the interference cause by the spray increased dramatically with the size of the spray droplets, the poor atomization of Conditions F4 and F5 prevented the measurement of these conditions.

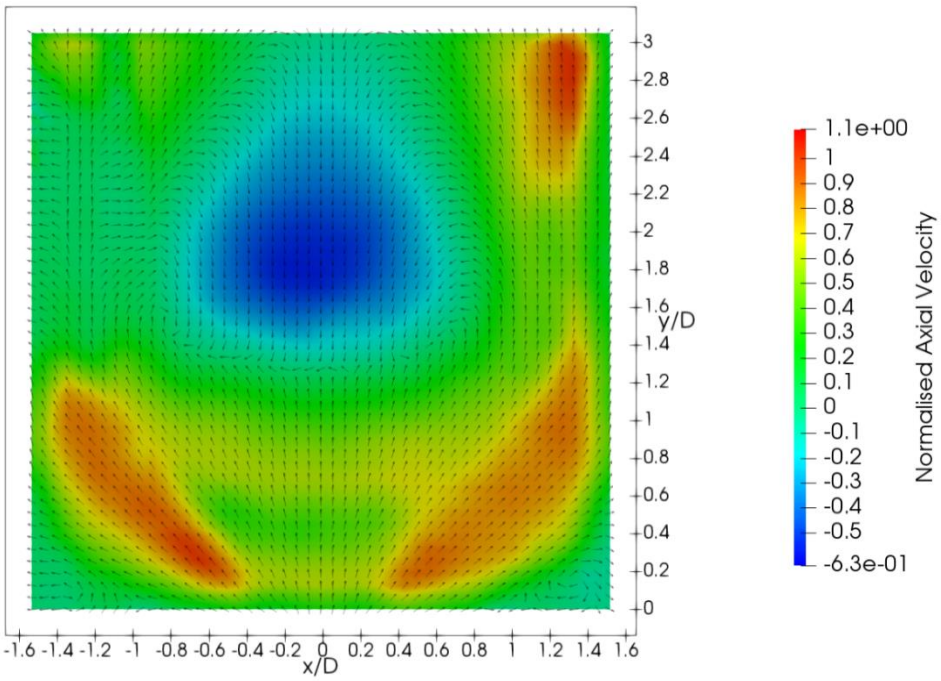

Figure 30: Normalized mean axial velocity mapping at Condition F1.

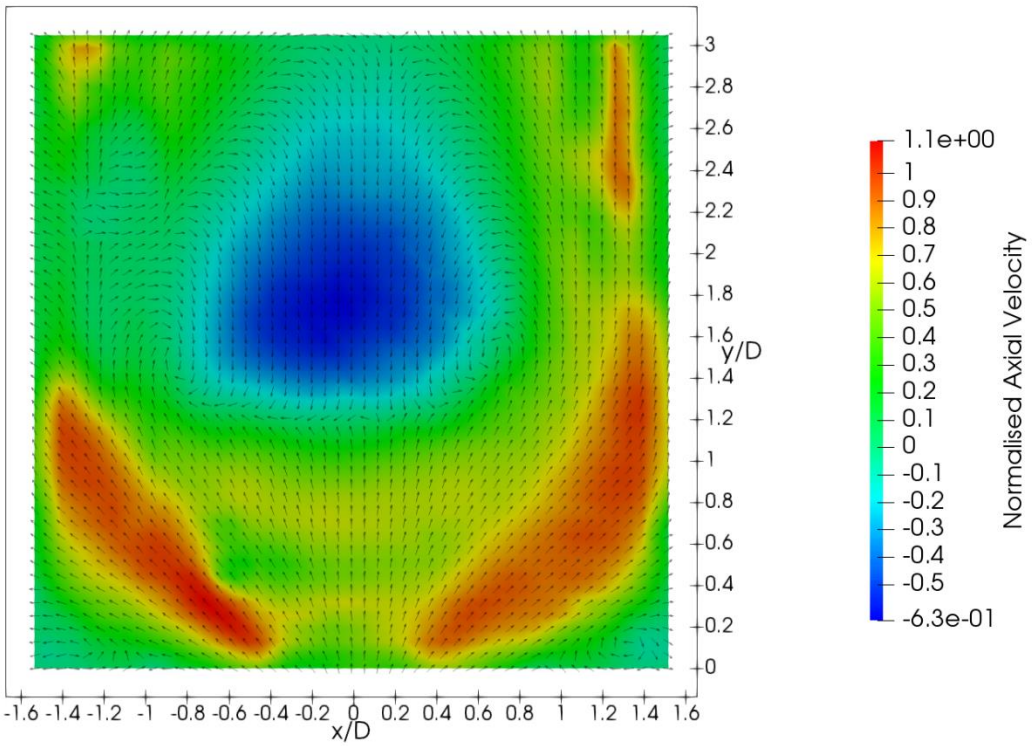

Figure 31: Normalized mean axial velocity mapping at Condition F3.

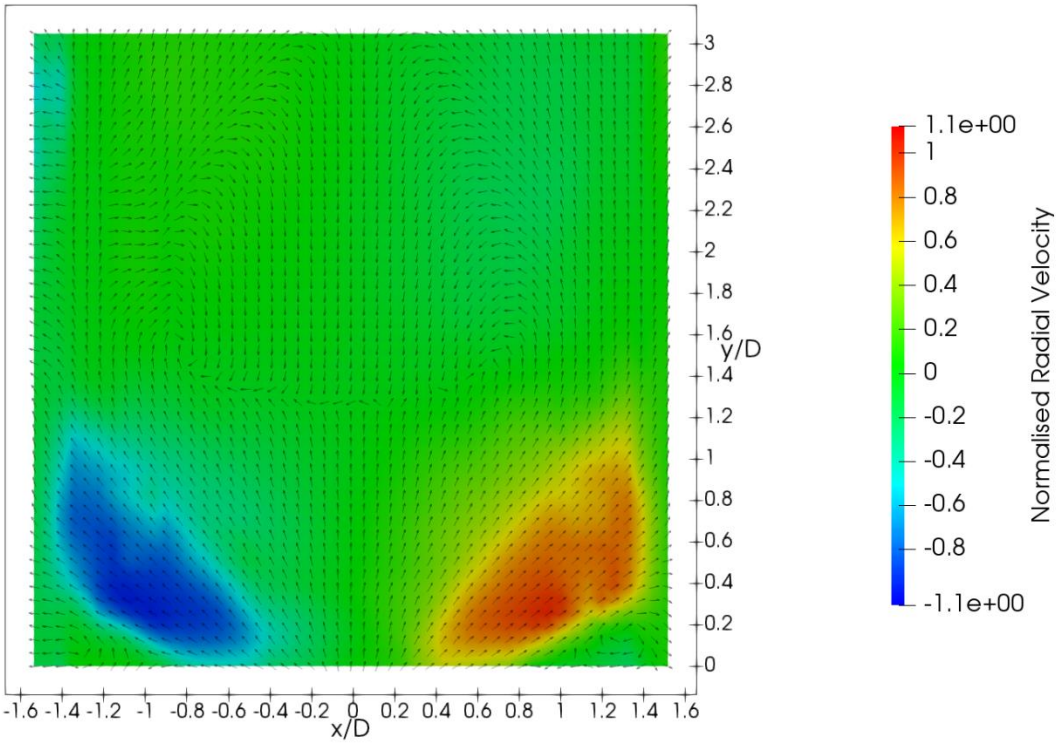

Figure 32: Normalized mean radial velocity mapping at Condition F1.

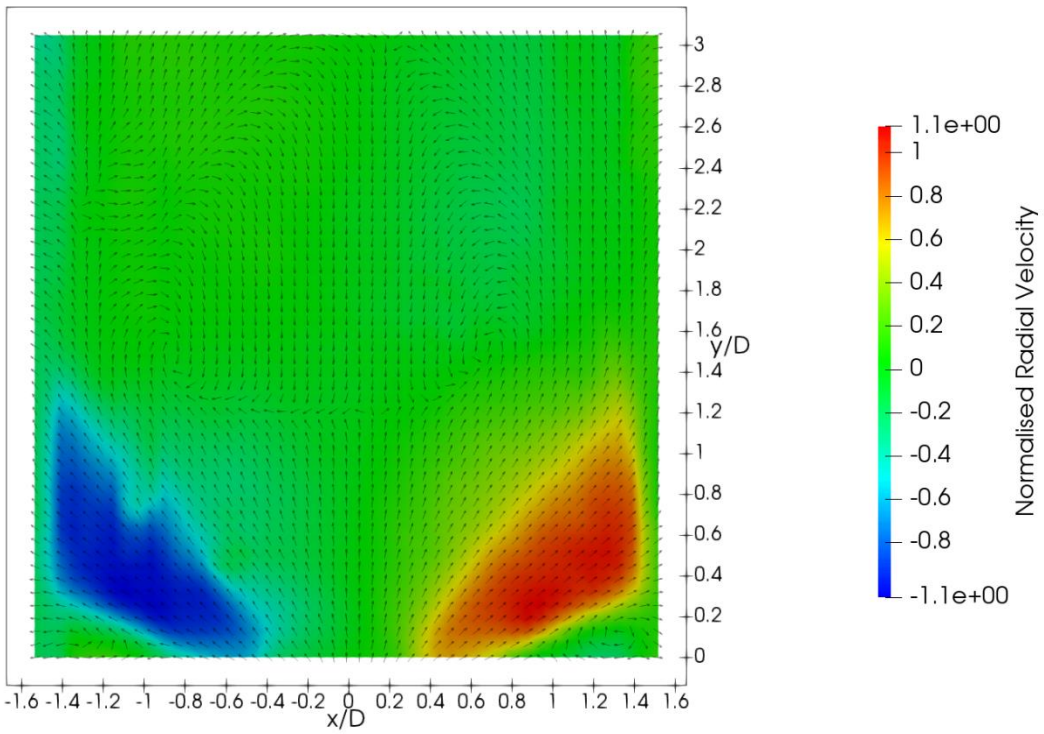

Figure 33: Normalized mean radial velocity mapping at Condition F3.

Chapter VII: Chemiluminescence Analysis

As can be seen below in Figures 34–38, the structure of the CH* emittance profile changed dramatically from case to case. Conditions F4 and F5 exhibited CH* emittance structures similar in geometry to the portion of the central recirculating zone closest to the injection axis. Conditions F1–F3, however, displayed emittance structures very similar in geometry to the spray cones produced by these conditions.

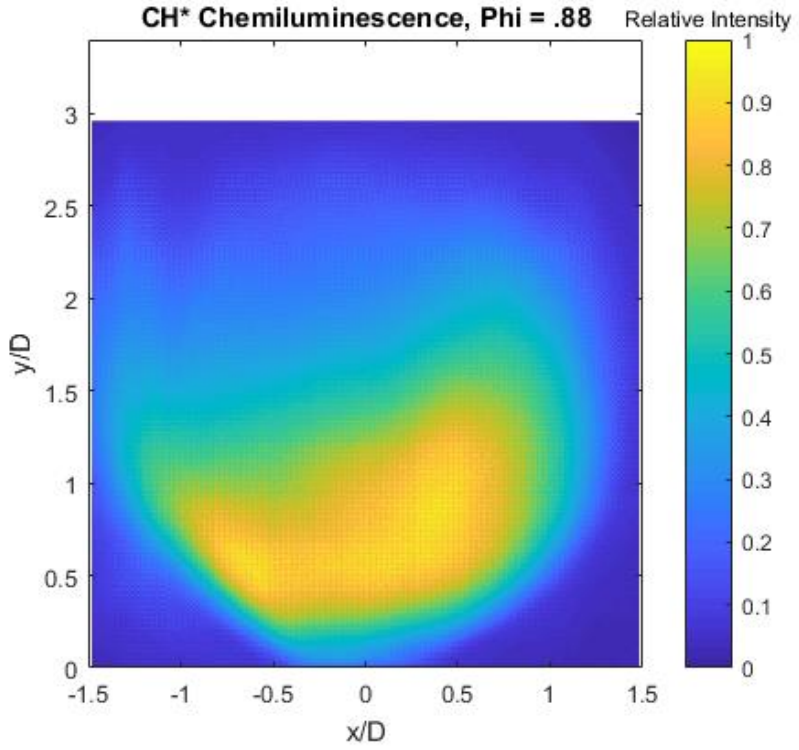

Figure 34: CH chemiluminescence mapping at Condition F5.*

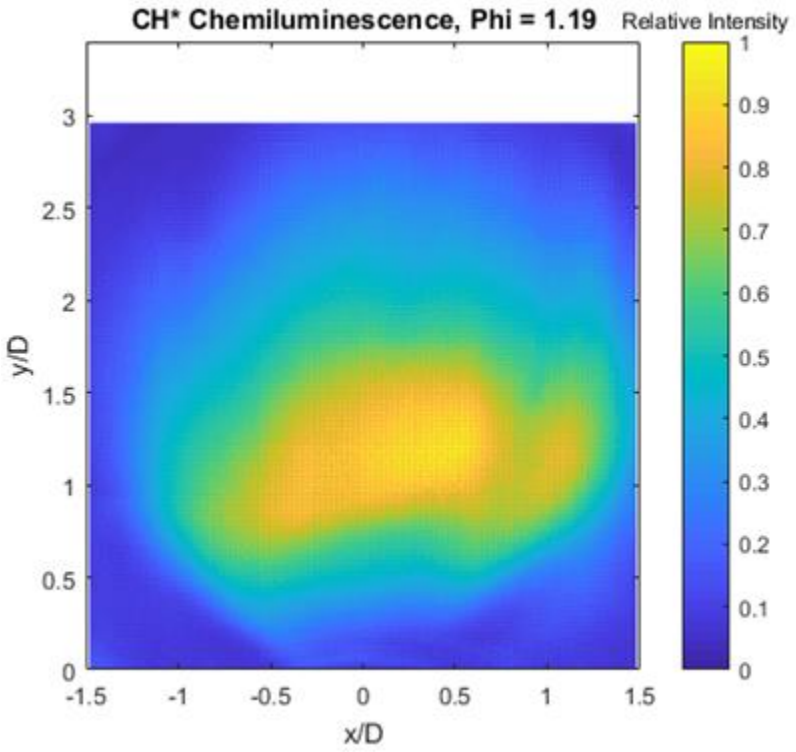

Figure 35: CH chemiluminescence mapping at Condition F4.*

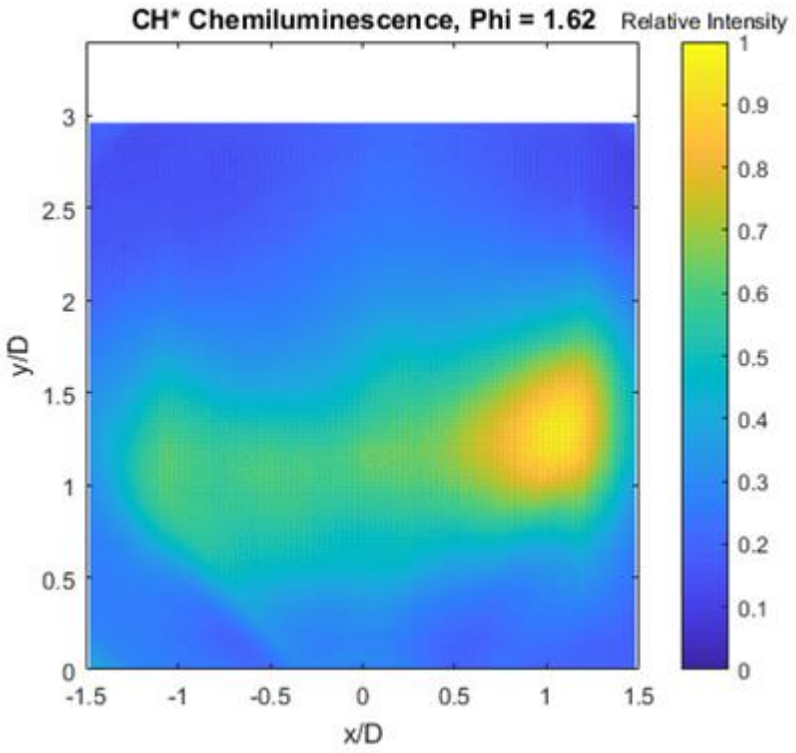

Figure 36: CH chemiluminescence mapping at Condition F3.*

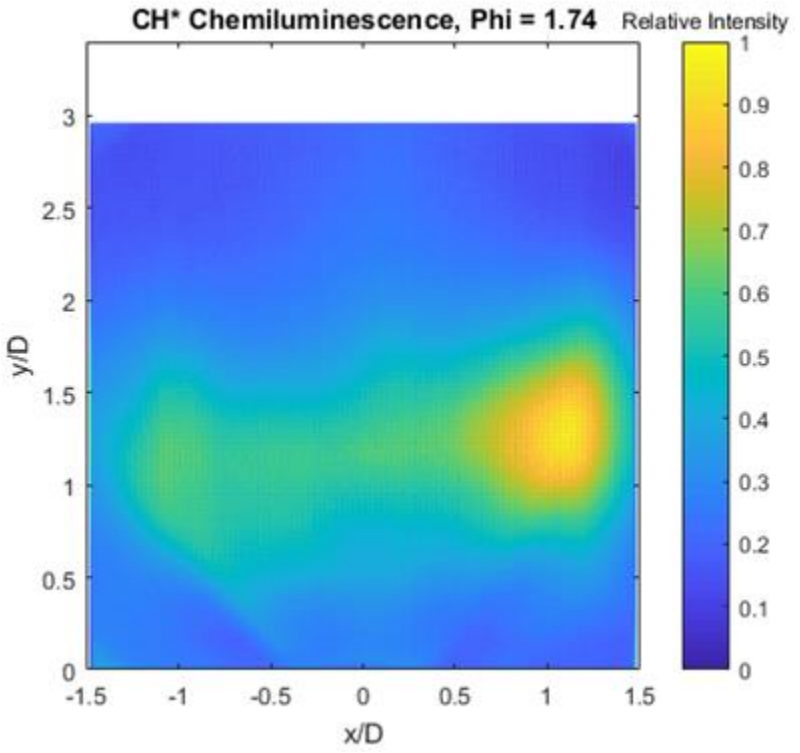

Figure 37: CH chemiluminescence mapping at Condition F2.*

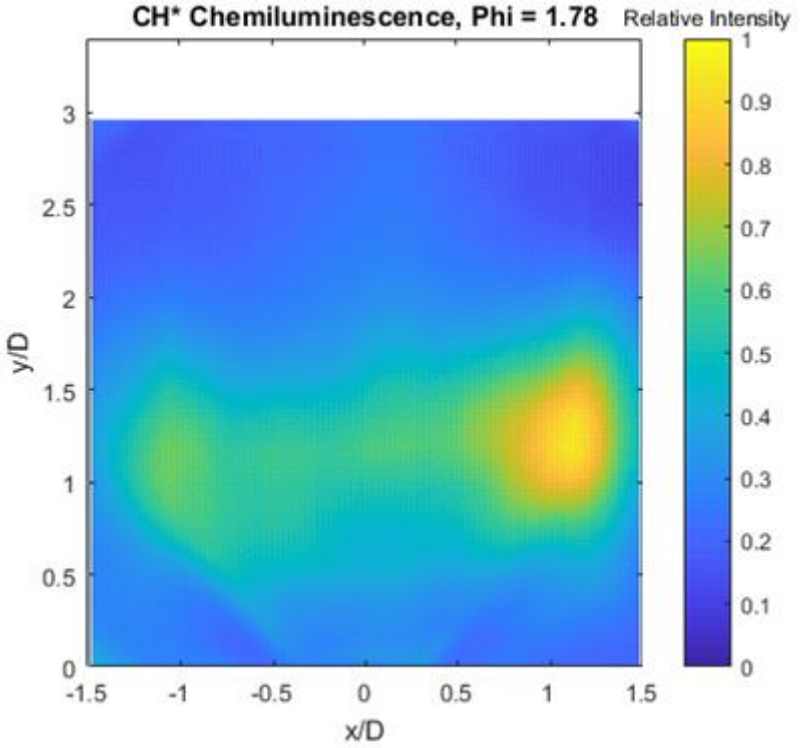

Figure 38: CH chemiluminescence mapping at Condition F1.*

As shown in Figures 39-42, the NO_2* and OH* emittance profiles of Conditions F4 and F5 were very similar in structure and point-to-point relative intensity values. In both cases, the emittance structures seemed to follow the geometry of the central recirculating zone. In both measurements the profiles of Condition F4 were centered along the injector axis, although these profiles were asymmetrical, whereas the profiles of Condition F5 were biased toward the positive radial direction. It should also be noted that while the OH* and NO_2* profiles of Conditions F4 and F5 were similar to each other, the signal-to-noise ratio of these measurements was extremely low due to the low sensitivity of the camera utilized at these wavelengths.

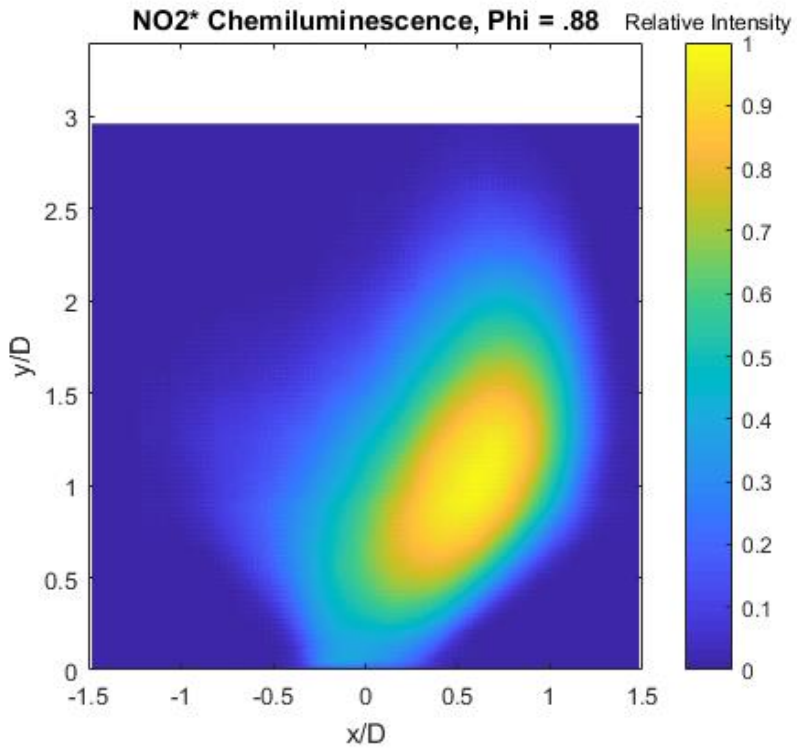

Figure 39: NO_2 chemiluminescence mapping at Condition F5.*

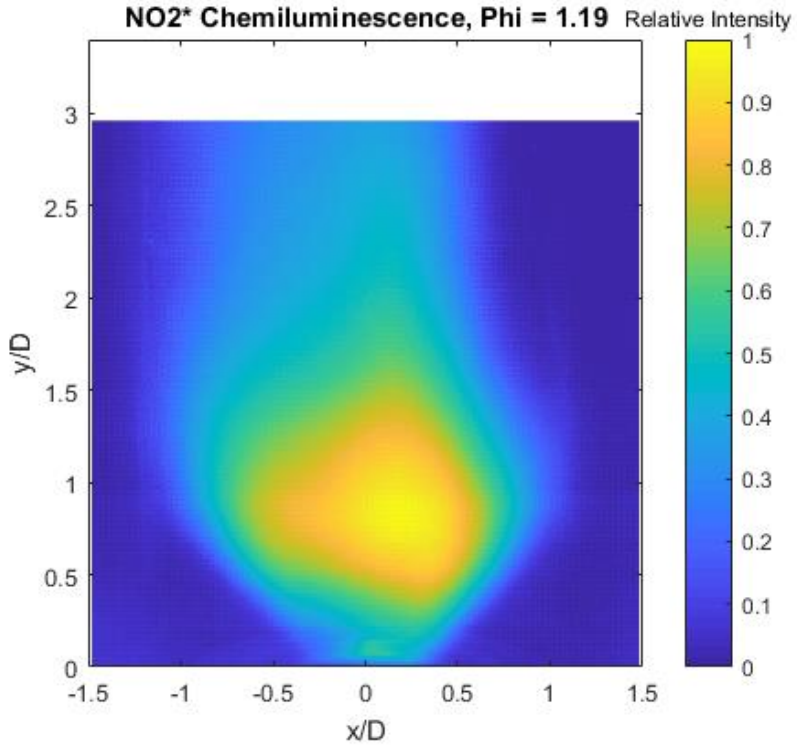

Figure 40: NO_2 chemiluminescence mapping at Condition F4.*

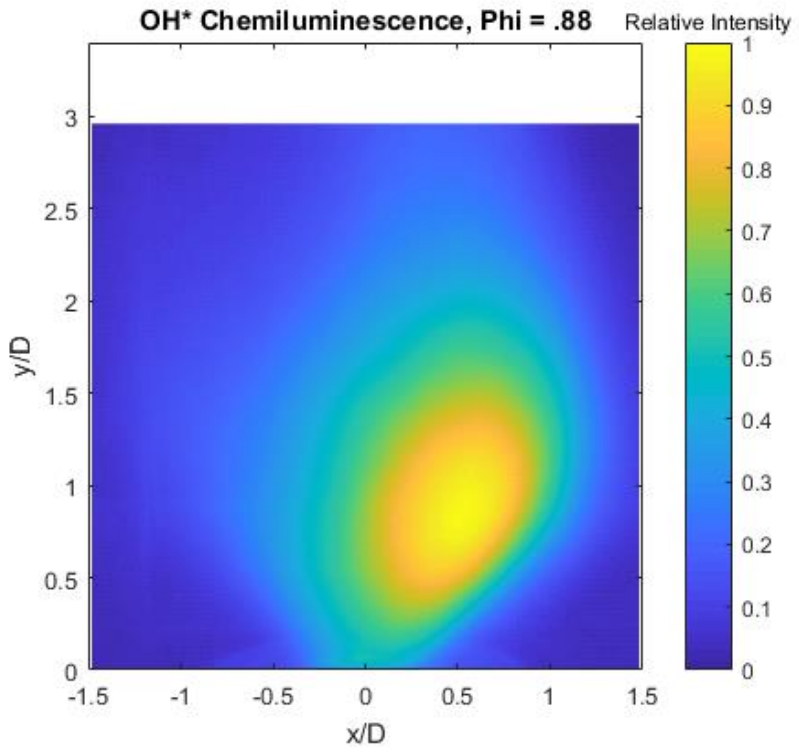

Figure 41: OH chemiluminescence mapping at Condition F5.*

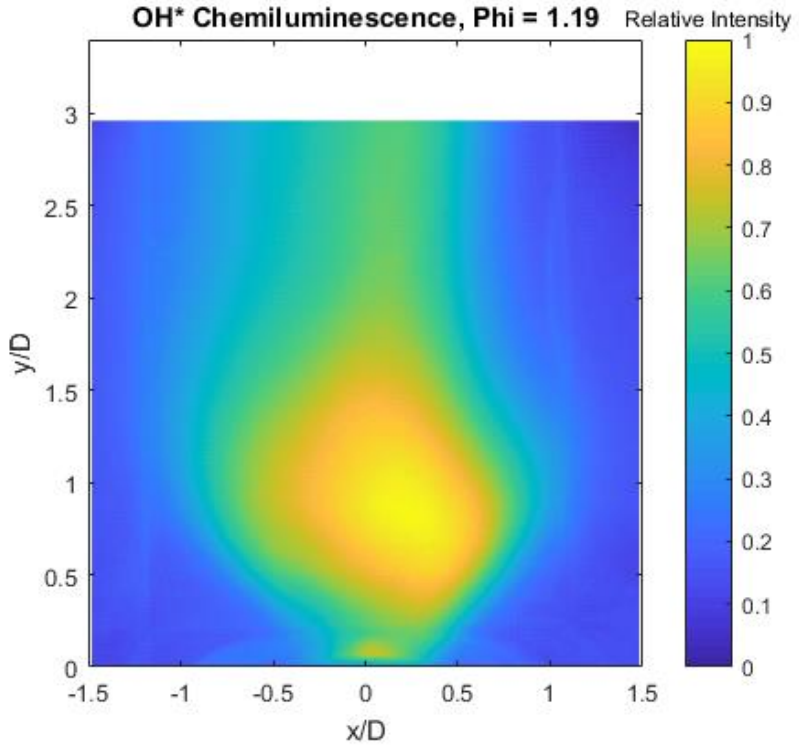

Figure 42: OH chemiluminescence mapping at Condition F4.*

Chapter VIII: Visual Spectrum Analysis

As seen in Figures 43–47 below, the visible flame shapes of the tested conditions exhibited two types of structures. Conditions F4 and F5 both exhibited similar visible flame geometry, being an asymmetric shape bounded on all sides by the extents of the central recirculating zone. The flame of Condition F5 was also biased heavily toward the positive radial direction.

Conditions F1–F3, however, shared a completely different flame geometry. These cases all exhibited a central, swirling, highly turbulent vortex of moderate luminosity in the area of the central recirculating zone, followed by a large region of extremely high luminosity farther in the axial direction. Through careful analysis of the raw AVI files from which Figures 43–47 were formed, it was found that while the luminosity of any given point within the central vortex was highly time dependent, the integral of the luminosity of Condition F3 across the entire image set was higher than those of F1 and F2 within this central region. This was likely due to the fact that the F3 condition produced more soot than the F1 and F2 conditions, thus providing more medium for incandescence in the visible spectrum.[33]

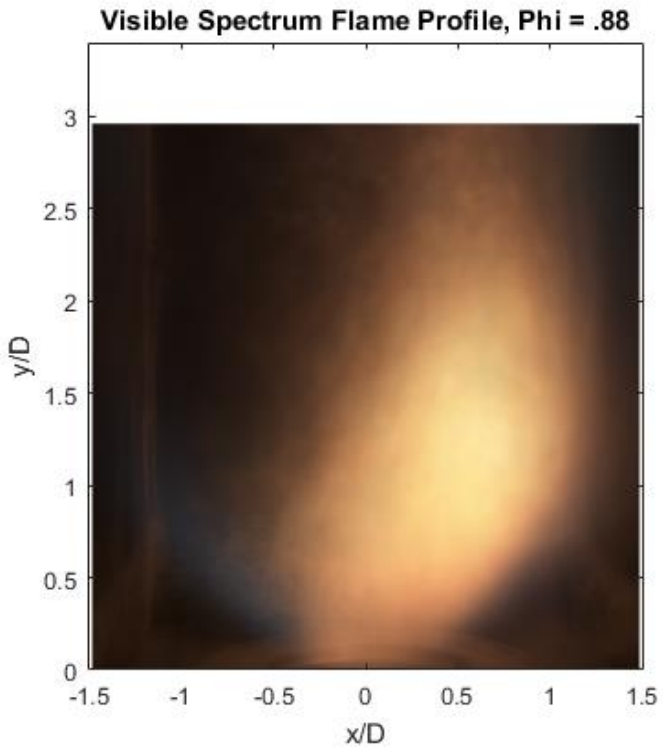

Figure 43: Visible spectrum flame profile at Condition F5.

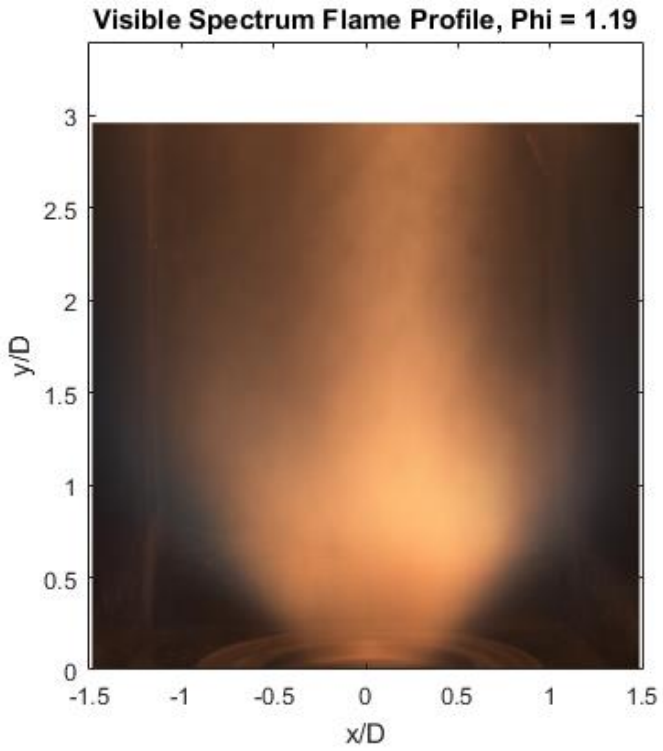

Figure 44: Visible spectrum flame profile at Condition F4.

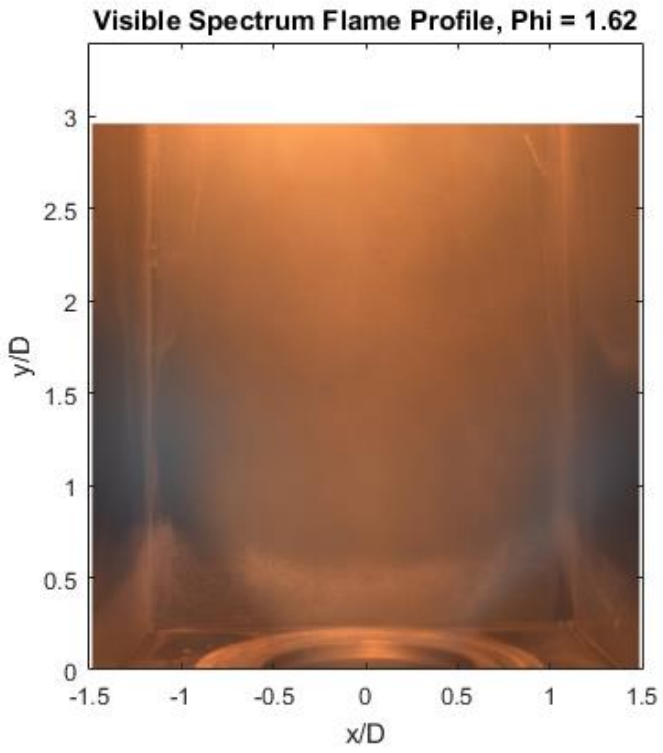

Figure 45: Visible spectrum flame profile at Condition F3.

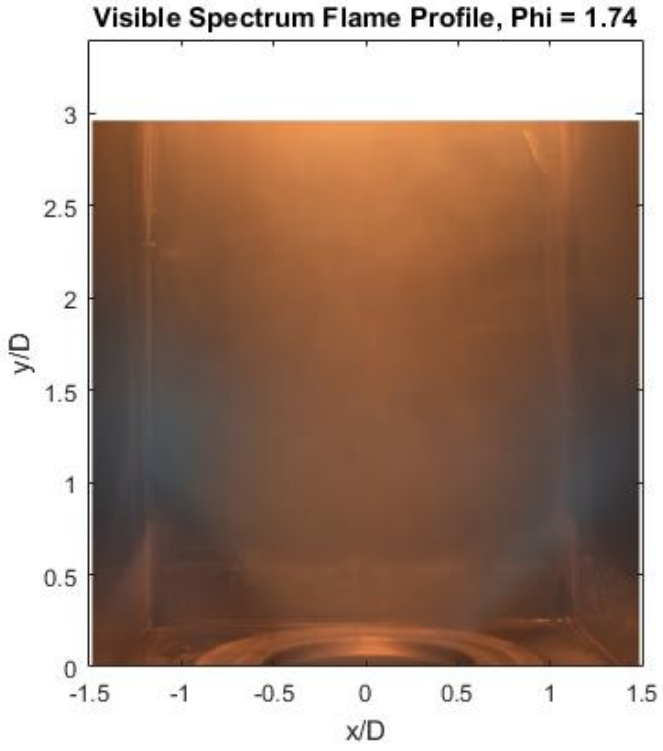

Figure 46: Visible spectrum flame profile at Condition F2.

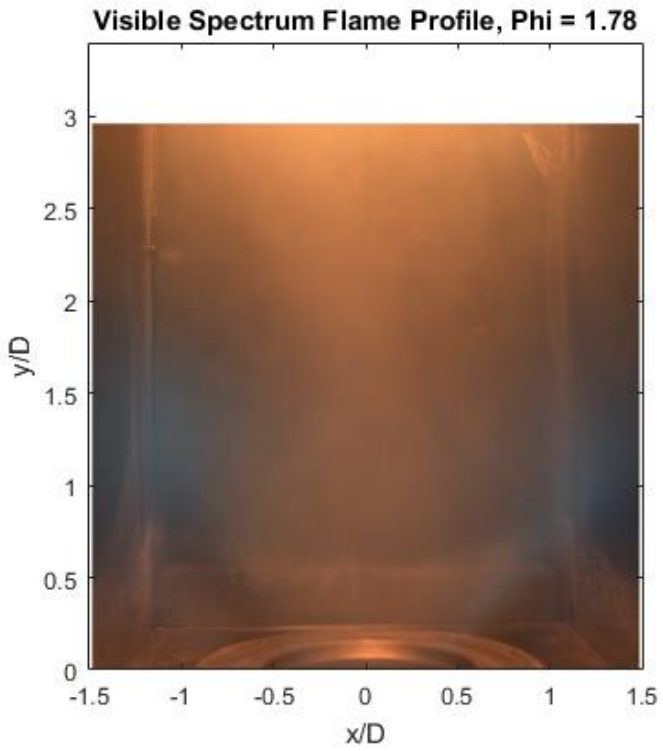

Figure 47: Visible spectrum flame profile at Condition F1.

Chapter IX: CH_2O Planar Laser Induced Fluorescence

As seen in Figures 48–51 below, the formaldehyde (CH_2O) PLIF profiles of Conditions F4 and F5 were very similar to each other in structure, each being bounded by the geometry of the central recirculating zone, with the difference that the F5 case was biased to the positive radial direction to a far greater degree and did not penetrate as far in the axial direction as the F4 case. This mirrored the behavior found in the chemiluminescence and visible spectrum testing for these two cases.

Conditions F3 and F1 both exhibited similar emissions profiles, consisting what appeared a central cone shape that expanded outwards as the axial dimension increased. In both cases the strongest regions of emittance were located far from the injection plane in the axial direction. This mirrored the behavior found in the visible spectrum analysis of these two cases, as the most luminous part of the flame was also located in this region.

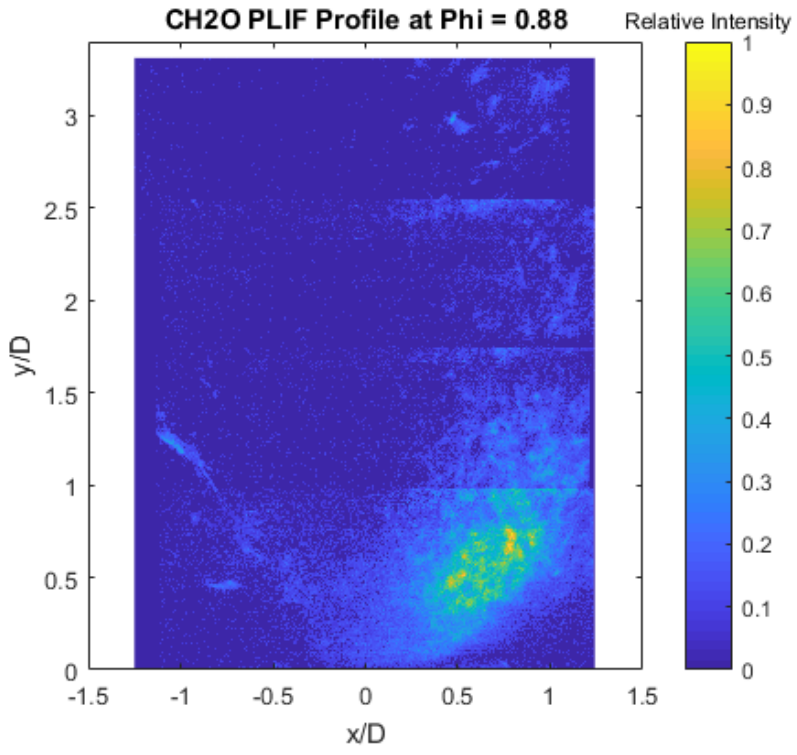

Figure 48: CH_2O PLIF profile at Condition F5.

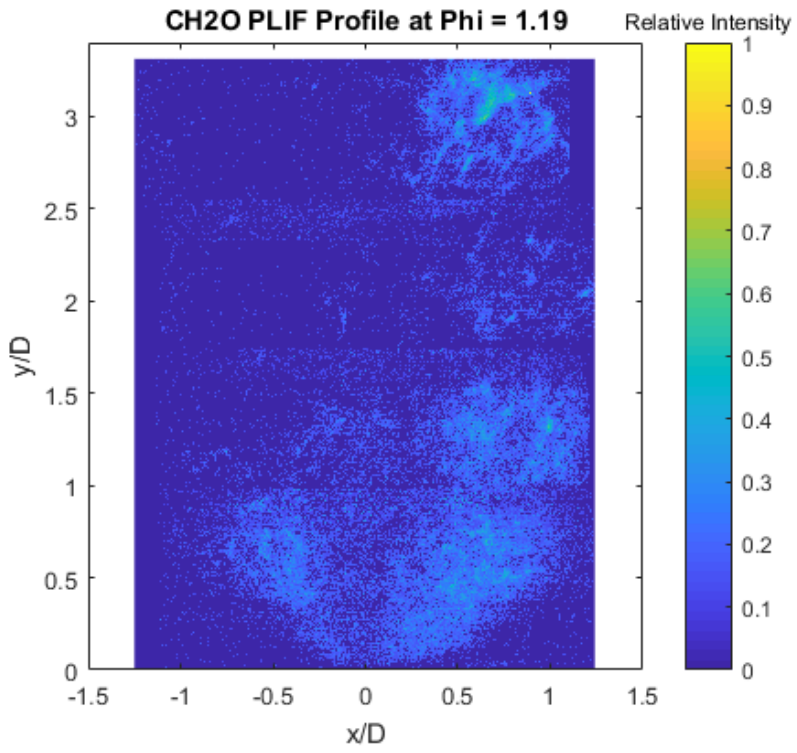

Figure 49: CH_2O PLIF profile at Condition F4.

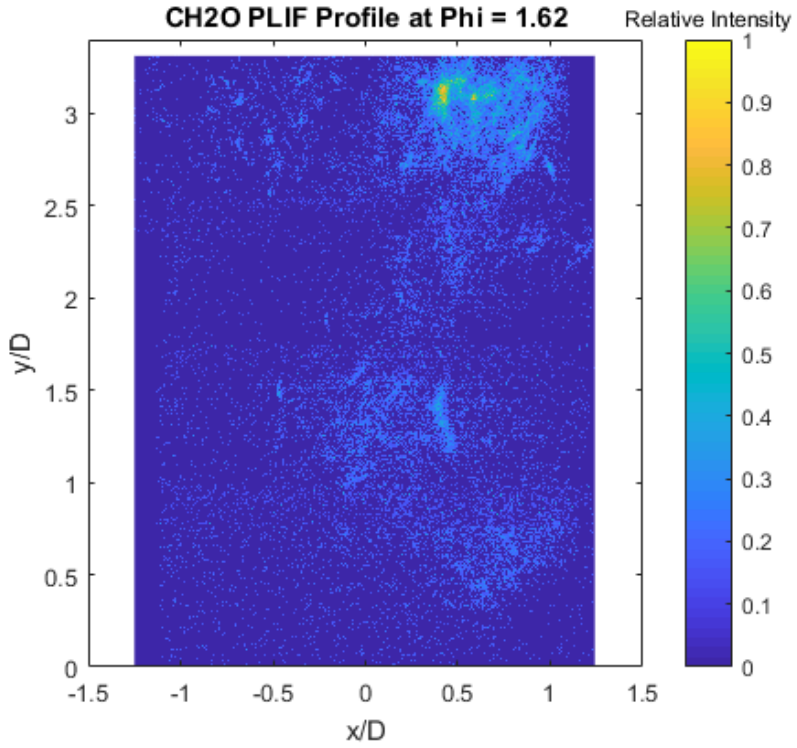

Figure 50: CH_2O PLIF profile at Condition F3.

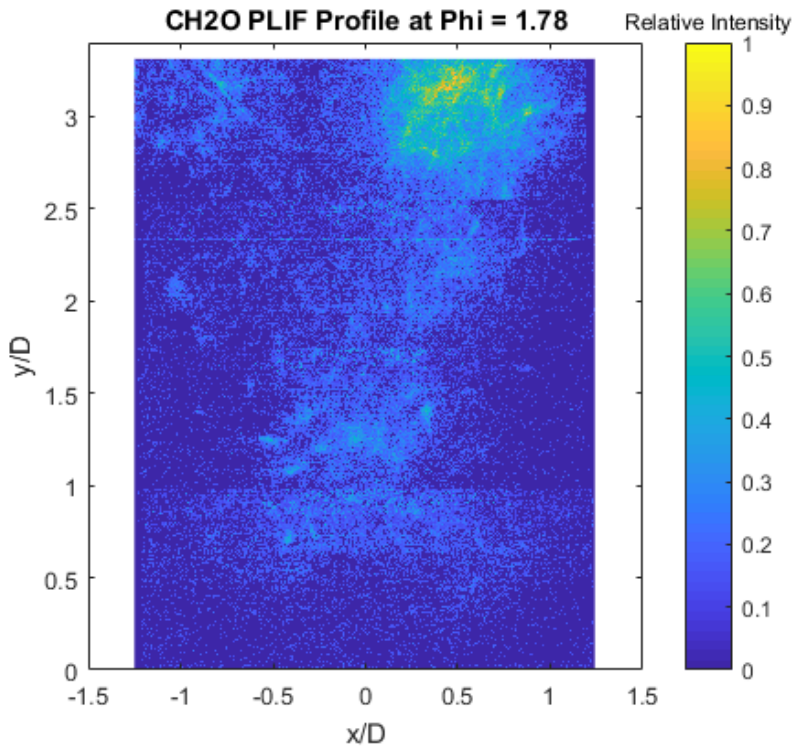

Figure 51: CH_2O PLIF profile at Condition F1.

Chapter X: OH Planar Laser Induced Fluorescence

The OH PLIF signals in all conditions were strongest in the positive radial direction. This was not expected, as the laser was being introduced to the chamber from the negative face. As the OH signal would have been weakest in the positive radial direction if laser attenuation had been the issue, due to the decrease in laser energy as the sheet traveled through the chamber, it was concluded that laser attenuation due to wall fouling was not the cause of the phenomenon. Similarly, since the difference in signal strength was not symmetrical with respect to the injection axis it was concluded that obscuration of the OH signal by wall fouling was not the cause, as wall fouling would not have only existed on one half of the *x* axis. This result is in good agreement with the OH* chemiluminescence results.

Although the OH PLIF profiles did not match those of CH_2O PLIF, this was to be expected. While both CH2O and OH form in the preheat region of the flame, the concentration of CH2O peaks within the preheat region while the concentration of OH peaks after the heat release region.[33] Therefore OH was expected to exist throughout much of the downstream measurement domain. The OH and CH_2O signals overlapped within the region close to the injection axis at y/D = .5 at low fuel flow rates, as can be seen in Figures 52–54 by the lower bound of the OH region, and along the boundaries of the central recirculating zone at $y/D = 1.5$ for higher fuel flow rates, as seen in Figures 55 and 56. These regions of intersection correspond to the areas of blue flame found in the visual analysis. At low fuel flow rate conditions, these regions are very faint and extend toward the boundaries of the chamber, as can be seen in Figures 52 and 53. At higher fuel flow rate conditions, while the blue regions still radiate to the chamber boundaries, they are much stronger and propagate toward the boundaries of the central recirculating zone. Together these measurements conclude that the heat release region of the higher flow rate was located around the axial location of y/D=1.5 It should be noted here that the darkened band at y/D = 1.3 was an artifact of the averaging process

between the two ‘stitched’ images of each trial, caused by a slight difference laser power across the sheet profile.

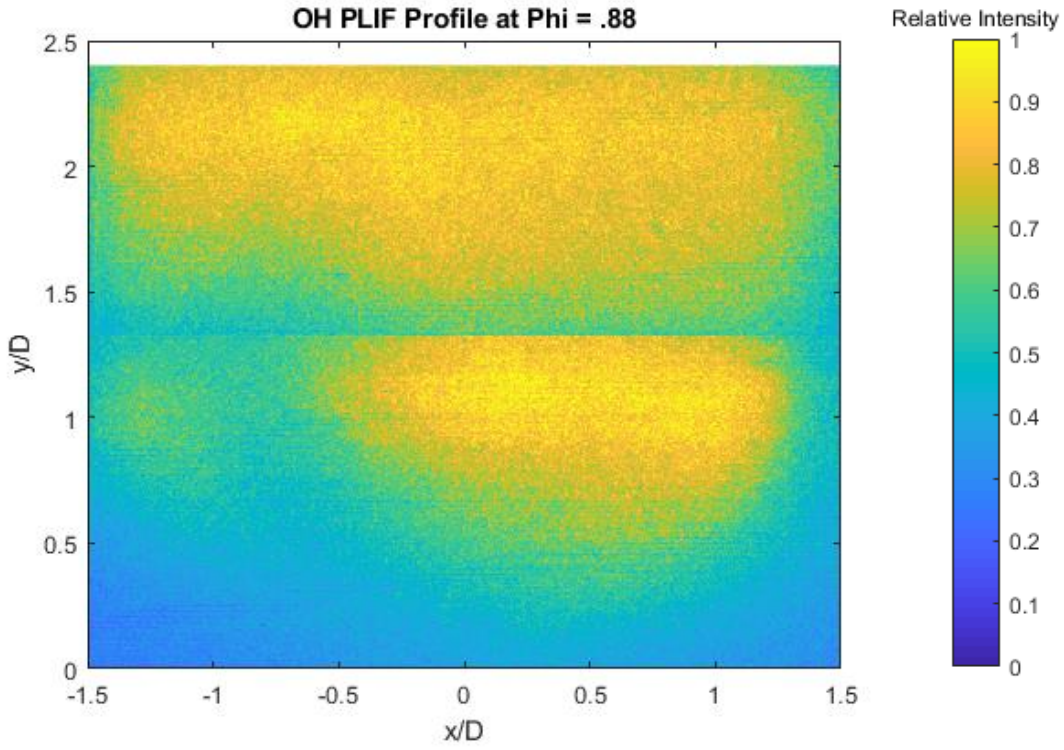

Figure 52: OH PLIF profile at Condition F5.

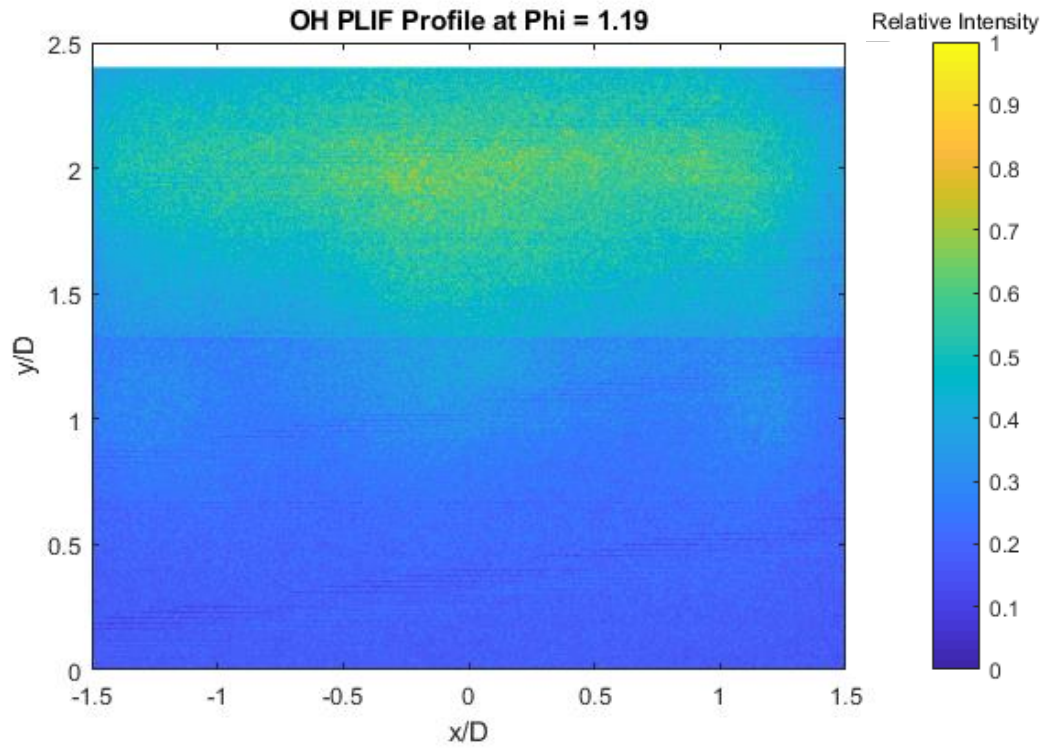

Figure 53: OH PLIF profile at Condition F4.

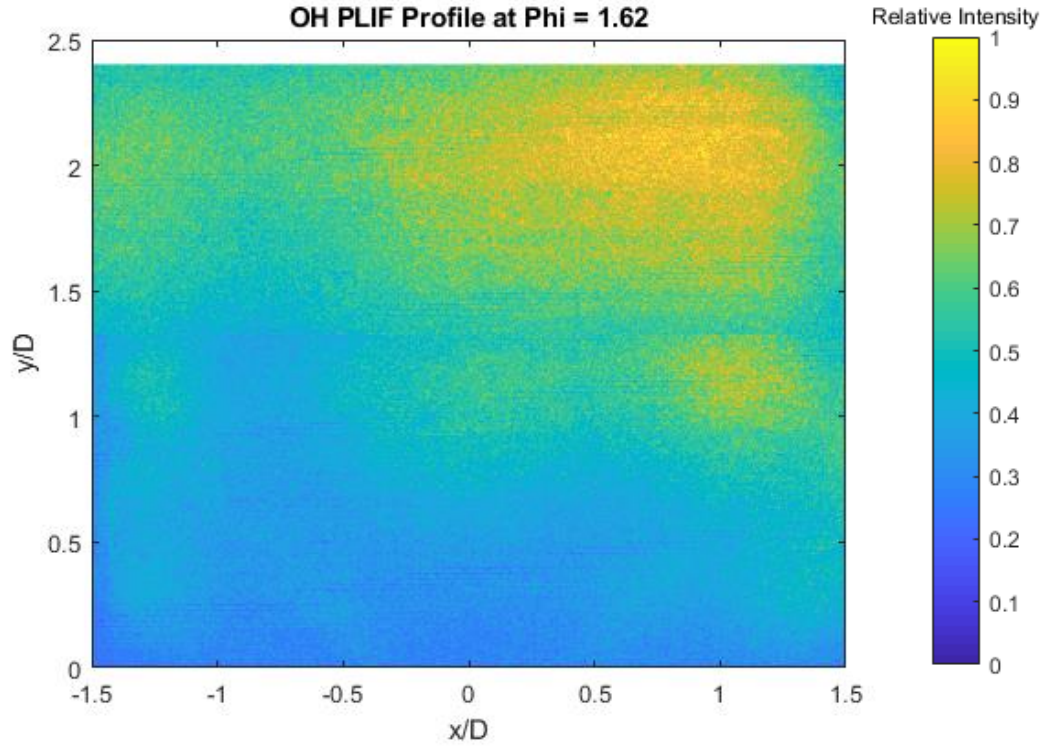

Figure 54: OH PLIF profile at Condition F3.

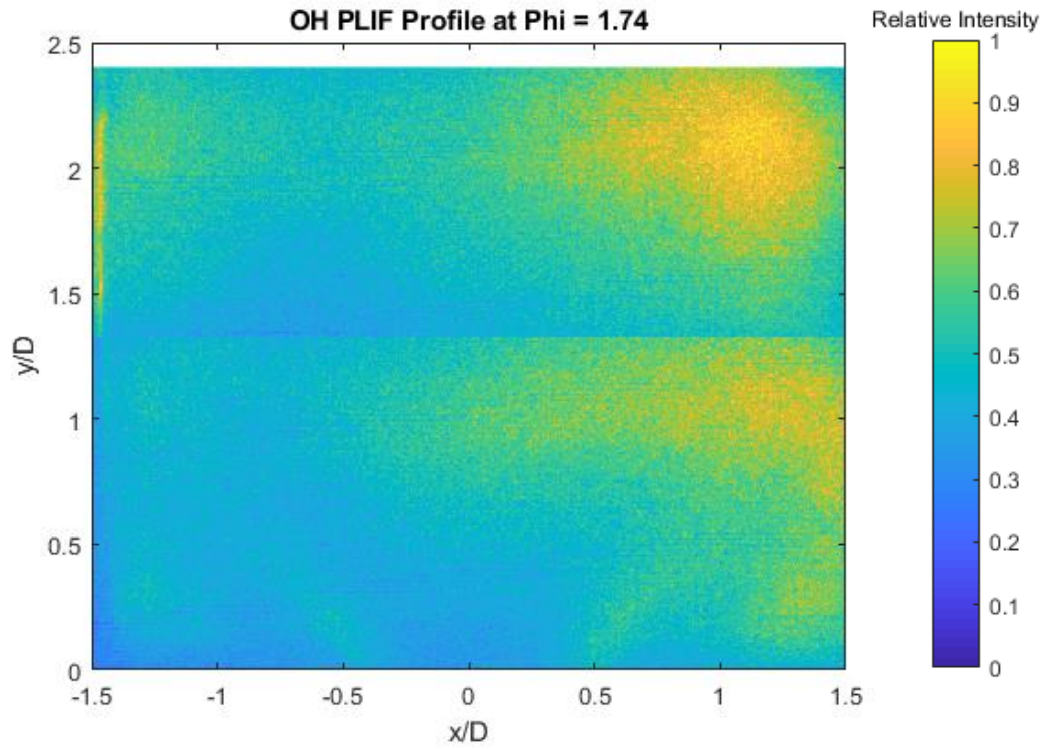

Figure 55: OH PLIF profile at Condition F2.

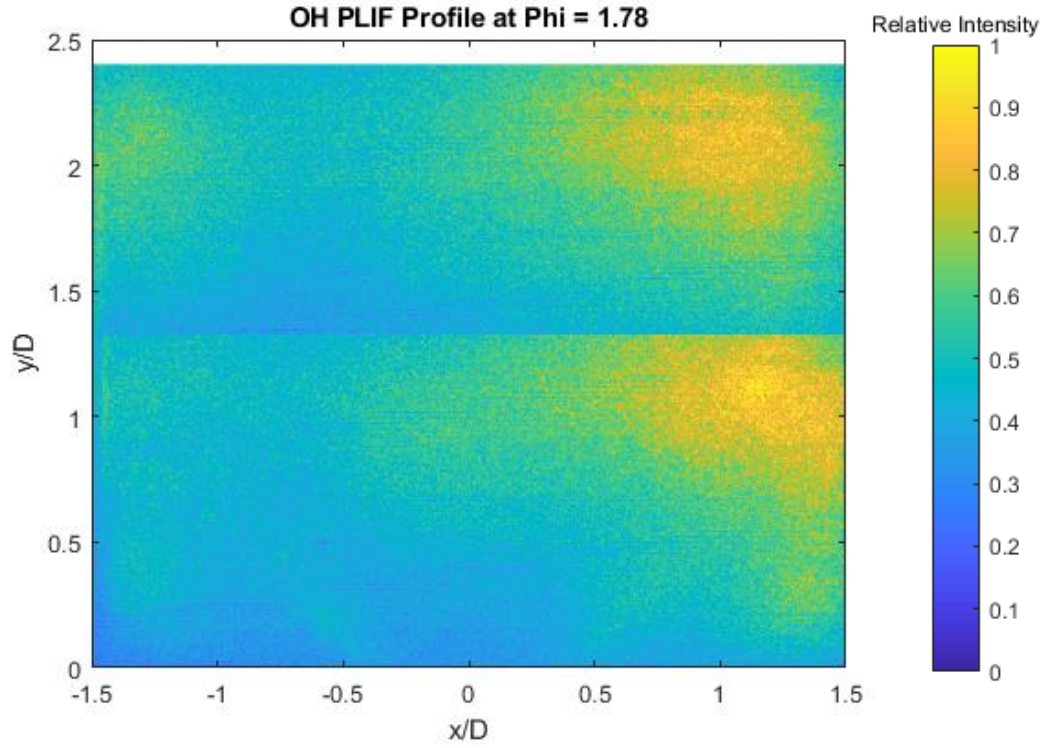

Figure 56: OH PLIF profile at Condition F1.

Chapter XI: Conclusions

11.1 Diagnostics Results and Experimental Rig Configuration

Though this effort it was found that the available diagnostics tools were in good agreement with each other in terms of flow structure, flame structure, and reaction zone location despite these diagnostics methods being utilized independently rather than simultaneously. This led to the conclusions that the air and fuel delivery systems utilized in this rig were consistent enough as to establish repeatable flame conditions within the confinement chamber and that the diagnostics methods utilized were properly configured and deployed so as to establish truly time-resolved measurements of the flame. This conclusion extends to the entire design of the rig itself, including the translation system utilized to change the measurement plane location and/or diagnostic methods between tests, as well as the scripts utilized to plot individual measurements to physical coordinates.

The largest source of variance found in this experimental setup was in the mounting location of the swirler-injector assembly. It was found that even slight differences in mounting location produced large changes in the flow field, even within the margin of error of the factory mounting system. It has been determined that a new mounting system will have to be produced for future injection systems, likely limiting the modularity of the plenum configuration.

11.2 Injector Characterization Results

The normalized mean axial velocity profiles clearly showed that the nonreacting flow field of this injector and swirler was of a fair degree of symmetry with respect to the injection axis. More importantly this flow field maintained its structure and symmetry across a wide range of pressure drop conditions bracketing the 3% design condition. This led to the conclusion that mixing performance, as well as flow/flame stabilization behavior, should remain relatively constant across these pressure drop conditions. Although asymmetries were present they were located downstream of the injection axis and at the farthest radial points of the domain or were determined to have been caused by the uncertainty present in the mounting of the swirler assembly. Moreover, the degree of

asymmetry increased as the axial and radial location of the point of measurement increased. This suggests that an interaction between the wall and the swirling field is the root cause of the asymmetry.

The normalized mean radial velocity profiles did not display the same degree of symmetry throughout the measurement region. Near the injection plane it was found that the radial velocity profile was dominated by the swirler rather than any recirculating or wall effects, as was expected. As the axial distance from the injection plane increased however, the degree of symmetry with respect to the injection axis decreased. Around the location y/D=1, the signs of the radial velocity components were found to have reversed for Conditions A2 and A3 due to the location of the centroid of the recirculating vortices. In analyzing the position of the recirculating vortices between various pressure drop and mounting conditions it was conjectured that the axial velocity of the airflow near the confinement wall and boundary of the central recirculating zone effected the axial location of the vortices.

The nonreactive cases all displayed areas of low turbulent kinetic energy in the region of the recirculating zone. Moreover, the velocity fluctuation components in this region were all equal to or less then than those of the surrounding low velocity region. These low fluctuation values lead to the conclusion that the flow within the recirculating zone is highly stable compared to the rest of the flow.

The present TR-PIV results show that the behavior of the reacting flow was found to be quite different from that of the nonreacting case as expected. Across all tested fuel flow conditions the reacting flow exhibited a short ‘bubble shaped’ central recirculating zone located downstream from the injection plane and high velocity swirling regions emanating from the primary swirler. It was found that the geometry of these structures was partially dictated by the presence of high velocity spray particles in those regions of the flow field. It was also determined that the asymmetries present

in the high fuel flow cases (Conditions F1 and F3) were likely due to the interference of the fuel particles themselves on the TR-PIV measurement. This was supported by the spray cone analysis, as the spray cones of both of those cases were found to have been both hollow and symmetrical.

The poor data quality exhibited in the low fuel flow conditions, F4 and F5, was found to be due to interference from the fuel particles on the TR-PIV measurement. The spray cone for Condition F4 was narrower than those of the higher spray conditions and consisted of far larger particles. The spray structure for Condition F5 was found to be of the 'onion' type, being highly unstable in terms of both particle size and geometry. These facts lead to the conjecture that the flame structure of these conditions is likely dominated by the spray structure and particle size rather than by differences in air flow or delivery.

Based on the overall shape of the chemiluminescence, PLIF, and visible spectrum profiles for Condition F5, it can be concluded that the main reacting region of this flame was likely being dominated by the central recirculating zone. In this case atomization quality was extremely poor, as can be seen in Table 6, and the resulting particles were injected at low velocity relative to the other cases. Moreover, the spray pattern for this case was highly asymmetrical. As such, it is likely that since the fuel particles were being injected favoring one radial direction that these particles were being entrained by the recirculating flow within that region. This would allow for a long residence time within the recirculating zone, thus creating the strongly biased flame found in this condition.

It can also be concluded that a similar effect was taking place for Condition F4, though to a lesser extent. The spray atomization quality for this condition was still quite poor, however the resulting pattern was far more symmetrical than that of the F5 condition. As such, the increase in flame symmetry across all tests was to be expected.

Based on the combination of the CH_2O PLIF, OH PLIF, and visual analysis results, it was found that the flame was located within the measurement domain and exhibited two distinct

structures. At low fuel flow rates (F3–F5), these measurements all placed the flame near the wall of the chamber. It should be noted that the atomization of these conditions was quite poor, meaning that fuel did not immediately evaporate, allowing it to be carried to the wall and burn within the wall region.

At higher fuel flow rates (F1 and F2), the flame was placed within the region of the wall, but starting along the boundary of the central recirculating zone. It was conjectured that the improved atomization at these conditions allowed the fuel to begin evaporating within the recirculating zone, thus allowing it to burn within the region of the recirculating zone.

Both of these theories are in agreement with the operator's observations of slight fuel impingement on the wall of the chamber at the F5 condition and the presence of large droplets being visible via high speed cameras within the region of the wall in the F3–F5 conditions.

Chapter XII: Recommendations for Future Work

12.1 Experimental Rig Improvements

Efforts should be made to improve the mounting system utilized for the swirler-injector assembly so as to decrease the margin of error in the concentricity of mounting between experiments. This improvement should be made so that the margin of concentricity would be no more than 0.25mm in any given direction with respect to the swirler and confinement centerlines.

Efforts should be made to allow for simultaneous PLIF measurements so as to allow for 'single-shot' comparisons of the OH and CH_2O zones. This would allow for the visualization of individual flame surfaces within the turbulent flow, in turn allowing for analysis of their structure(s)[34,35]. Simultaneous PIV should also be employed so as to analyze the behavior of these surfaces both compared to the time resolved flow structure and the flow structures at each point in time.

12.2 Further Injector Study Recommendations

Additional PIV study should be conducted under nonreacting conditions utilizing a higher shear (increased horizontal component) swirler assembly at various pressure drop conditions as was done in this effort. The resulting flow should then be compared to the current swirler assembly so as to determine if any changes to the recirculation zone develop. Reacting experiments should then be carried out as was done in this effort so as to determine if the atomization quality increases with the increased shear of the airflow and if the flame structure changes in response.

Should this swirler change not result in an increased atomization quality, further testing should be conducted utilizing a pressure-swirl injector capable of higher atomization quality at the tested fuel flow rates. These tests should be conducted so as to determine if the flame structure changes as a function of the atomization quality, as concluded in this effort, or if other factors dominate this flame structure once the atomization quality improves.

LES should be conducted on the existing swirler and confinement geometries using the captured velocity and TKE profiles, ACd measurements, and global flow rates as boundary and initial conditions. This work should be carried out in three distinct steps. In the first step it would be recommended that RANS be employed so as to verify the convergence of the experimental inputs. In the second step LES would be employed in a fine mesh so as to reproduce the nonreacting flow field under cold conditions. In the final step the experimental spray characteristics should be utilized as the boundary conditions of a discrete phase spray model so as to attempt to reproduce the flame structure of the experimental element. Should the flame structure produced in this final step not agree with the experimental data it would be recommended that additional geometries be attempted, as well as alternative spray models.

References

1. Verkamp, F. J., Verdouw, A. J., Tomlinson, J.G. “Impact of Emission Regulations of Future Gas Turbine Engine Combustors.” *Journal of Aircraft*, vol 11, issue 6, 1974, pp. 340-344.

2. Lefebvre, A., Ballal, D. *Gas Turbine Combustion*. Boca Taton. CRC Press. 2010.

3. Liu, Y., Sun, X., Sethi, V., Nalianda, D., Li, Y., Wang, L., “Review of Modern Low Emissions Combustion Technologies for Aero Gas Turbine Engines.” *Progress in Aerospace Sciences*, vol. 94, 2017, pp. 12-45.

4. Smiljanovski, V., Brehm, N., “CFD Liquid Spray Combustion Analysis of a Single Annular Gas Turbine Combustor.” *Turbo Expo*, Indianapolis, Indiana, USA, ASME, 1999.

5. Singh, S., N., Seshadri, V., Singh, R., K., Mishra, T., “Flow Characteristics of an Annular Gas Turbine Combustor Model for Reacting Flows using CFD.” *Journal of Scientific and Industrial Research*, vol. 65, issue 11, 2006, pp. 921-934.

6. Wolf, P., Balakrishnan, R., Staffelbach, G., Gicquel, L., Poinsot, T., “Using LES to Study Reacting Flows and Instabilities in Annular Combustion Chambers.” *Flow, Turbulence and Combustion*, vol. 88, 2012, pp. 191-206.

7. Boudier, G., Gicquel, L., Poinsot, T., “Effects of Mesh Resolution on Large Eddy Simulation of Reacting Flows in Complex Geometry Combustors.” *Combustion and Flame*, vol. 155, issue 1-2, 2008, pp.196-214.

8. Johnson, M. R., Littlejohn, D., Nazeer, W. A., Smith, K. O., Cheng, R. K., “A Comparison of the Flowfields and Emissions of High-Swirl Injectors and Low-Swirl Injectors for Lean Premixed Gas Turbines.” *Proceedings of the Combustion Institute*, vol. 30, issue 2, 2005, pp. 2867-2874.

9. Han, X., Laera, D., Morgans, A., Lin, Y., Sung, C., "The Effect of Stratification Ratio on the Macrostructure of Stratified Swirl Flames: Experimental and Numerical Study." *Turbo Expo,* Olso, Norway, ASME, 2018.

10. Wick, A., Priesack, F., Pitsch, H., "Large-Eddy Simulation and Detailed Modeling of Soot Evolution in a Model Aero Engine Combustor." *Turbo Expo*, Charlotte, NC, USA, ASME, 2017.

11. Chterev, I., Rock, N., Ek, H., Smith, T., Noble, D., Mayhew, E., Lee, T., Jiang, N., Roy, S., Seitzman, J., Lieuwen, T., "Reacting Pressurized Spray Combustor Dynamics: Part 2 – High Speed Planar Measurements." *Turbo Expo,* Seoul, South Korea, ASME, 2016.

12. Grohmann, J., O'Loughlin, W., Meier, W., Aigner, M., "Comparison of the Combustion Characteristics of Liquid Single-Component Fuels in a Gas Turbine Model Combustor." *Turbo Expo,* Seoul, South Korea, ASME, 2016.

13. Sadanandan, R., Stohr, R., Meier, W., "Simultaneous OH-PLIF and PIV Measurements in a Gas Turbine Model Combustor." *Applied Physics B*, vol. 90, issue. 3-4, 2008, pp. 609-618.

14. Temme, J., Allison, P., Driscoll, J., "Combustion Instability of a Lean Premixed Prevaporized Gas Turbine Combustor Studied using Phase-Averaged PIV." *Combustion and Flame,* vol. 161, issue 4, 2014, pp. 958-970.

15. Melling, A., "Tracer Particles and Seeding for Particle Image Velocimetry." *Measurement Science and Technology,* vol. 8, no. 12, 1997, pp. 1406-1416.

16. Wernet, M., "Fundamentals of Digital Particle Imaging Velocimetry". Print.

17. Hadad, T., Gurka, R., "Effects of Particle Size, Concentration, and Surface Coating on Turbulent Flow Properties Obtained Using PIV/PTV." *Experimental Thermal and Fluid Science,* vol. 5, 2013, pp. 203-212.

18. Acevedo, Miguel, AFPET. Wright-Patterson AFB. Experimental Report.

19. Sivakumar, D., Vankeswaram, S., Sakthikumar, R., Raghunandan, B., "Analysis on the Atomization Characteristics of Aviation Biofuel Discharging from Simplex Swirl Atomizer." *International Journal of Multiphase Flow*, vol. 72, 2015, pp. 88-96.

20. Hirasawa, T., Sung, C., Joshi, A., Yang, Z., Wang, H., Law, C., "Determination of Laminar Flame Speeds Using Digital Particle Image Velocimetry: Binary Fuel Blends of Ethylene, n-Butane, and Toluene." *Proceedings of the Combustion Institute*, vol. 29, 2002, pp. 1427-1434.

21. Westerweel, J., "Fundamentals of Digital Particle Image Velocimetry." *Measurement Science and Technology*, vol. 8, 1997, pp. 1379-1392.

22. Twarog, K., CDL_Liquid_Fuel_Diagnostics, (2018), GitHub repository, https://github.com/RougeLeader1/CDL_Liquid_Fuel_Diagnostics.git

23. Lee, K., Puri, I., "NO_2 Chemiluminescent Emission from Flames Induced by Acoustic Noise." *KSME International Journal*. Vol. 12, issue 4, 1998, pp. 728-733.

24. Chowdhury, B., Cetegen, B., "Experimental Study of the Effects of Free Stream Turbulence on Characteristics and Flame Structure of Bluff-Body Stabilized Conical Lean Premixed Flames." *Combustion and Flame*, vol. 178, 2017, pp. 311-328.

25. Allison, P., Chen, Y., Thme, M., Driscoll, J., "Coupling of Flame Geometry and Combustion Instabilities based on Kilohertz Formaldehyde PLIF Measurements." *Proceedings of the Combustion Institute*, vol. 35, issue 3, 2015, pp. 3255-3262.

26. Scgbeuderm A, Mantzaras, J., Bombach, R., Schenker, S., Tylli, N., Janson, P., "Laser Induced Fluorescence of Flormaldehyde and Raman Measurements of Major Species during

Partial Catalytic Oxidation of Methane with large H2O and CO2 Dilution at Pressures up to 10 bar." *Proceedings of the Combustion Institute,* vol. 31, issue 2, 2007, pp. 1973-1991.

27. Hammack, S., Carter, C., Skiba, A., Fugger, C., Felver, J., Miller, J., Gord, J., Lee, T., "20 KHz CH2o and OH PLIF with Sereo PIV." *Optics Letters*, vol. 43, issue 5, 2018, pp. 1115-1118.

28. Burket, A., Paa, W., Reimert, M., Klinkov, K., Eigenbrod, C., "Formaldehyde LIF detection with Background Subtraction Around Signel Igniting GTL Diesel Droplets." *Fuel*. Vol. 111, 2013, pp. 384-392.

29. Bockle, S., Kazenwadel, J., Kunzelmann, T., Shin, D., Schulz, C., Wolfrum, J., "Simultaneous Single-Shot laser-Based Imaging of Formaldehyde, OH, and Temperature in Turbulent Flames." *Proceedings of the Combustion Institute,* vol. 28, issue 1, 2000, pp. 279-286.

30. Chaudhuri, S., Kostka, S., Renfro, M., Cetegen, B., "Blowoff Dynamics of Bluff Body Stabilized Turbulent Premixed Flames." *Combustion and Flame,* vol. 157, issue 4, 2010, pp. 970-802.

31. Lefebvre, A., *Atomization and Sprays*. New York. Hemisphere Publishing Corporation. 1989.

32. Kundu, P., Cohen, I., *Fluid Mechanics*. London. Academic Press. 2002.

33. Glassman, I., Yetter, R., *Combustion*. London. Academic Press. 2008.

34. Chaudhuri, S., Kostka, S., Renfro, M., Cetegen, B., "Blowoff Dynamics of Bluff Body Stabilized Turbulent Premixed Flames." *Combustion and Flame,* vol. 157, issue 4, 2010, pp. 970-802.

35. Rosell, J., Bai, X., Sjoholm, J., Zhou, B., Li, Z., Wang, Z., Pettersson, P., Li, Z., Richter, M., Alden, M., “Multi-Species PLIF Study of the Structures of Turbulent Premixed Methane/Air Jet Flames in the Flamelet and Thin-Reacting Zones Regimes.” *Combustion and Flame*, Vol. 182, 2017, pp. 324-338.

APPENDIX A: Nonreacting PIV Results for Conditions A2, A3, and A5

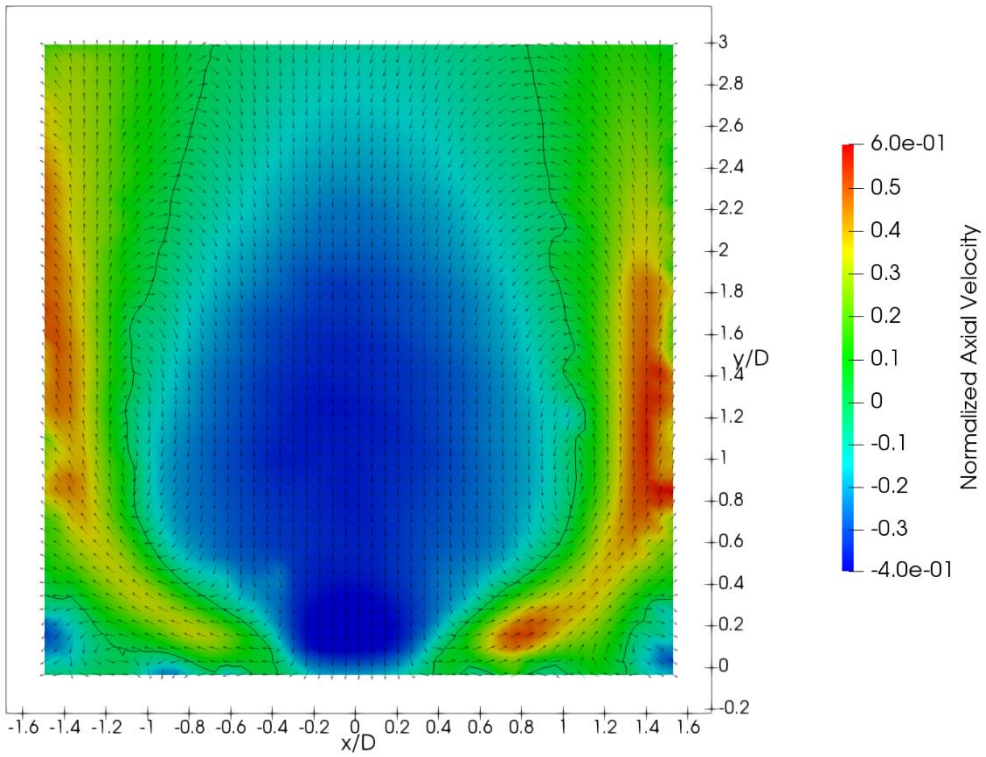

Figure A1: Normalized mean axial velocity mapping at Condition A2. Black line indicates contour of zero axial velocity.

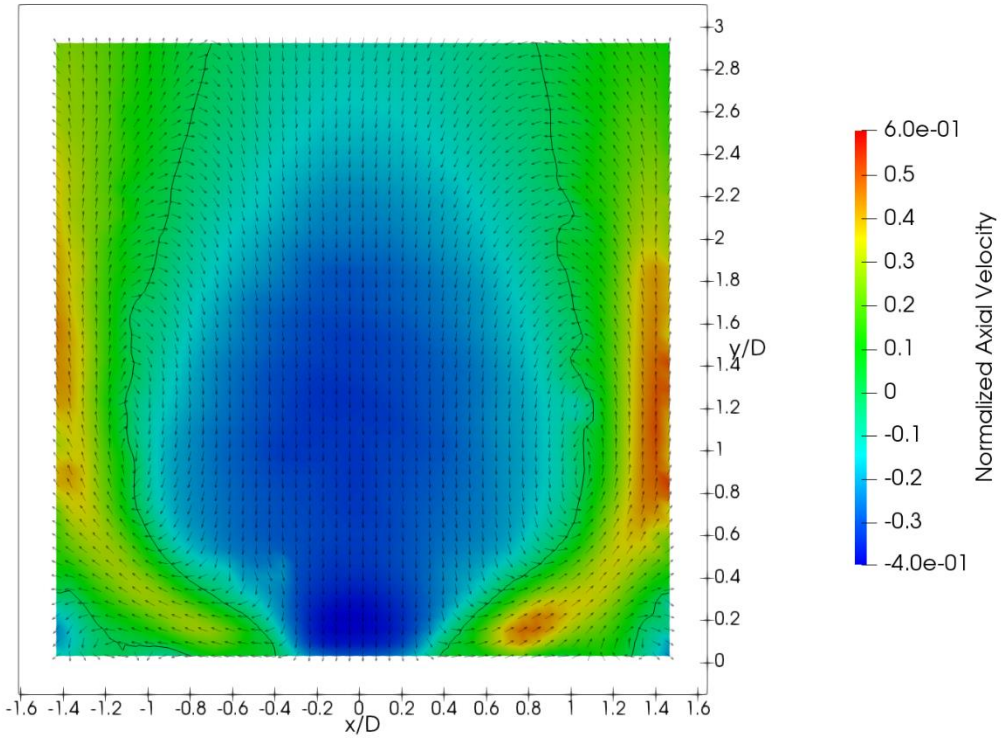

Figure A2: Normalized mean axial velocity mapping at Condition A3. Black line indicates contour of zero axial velocity.

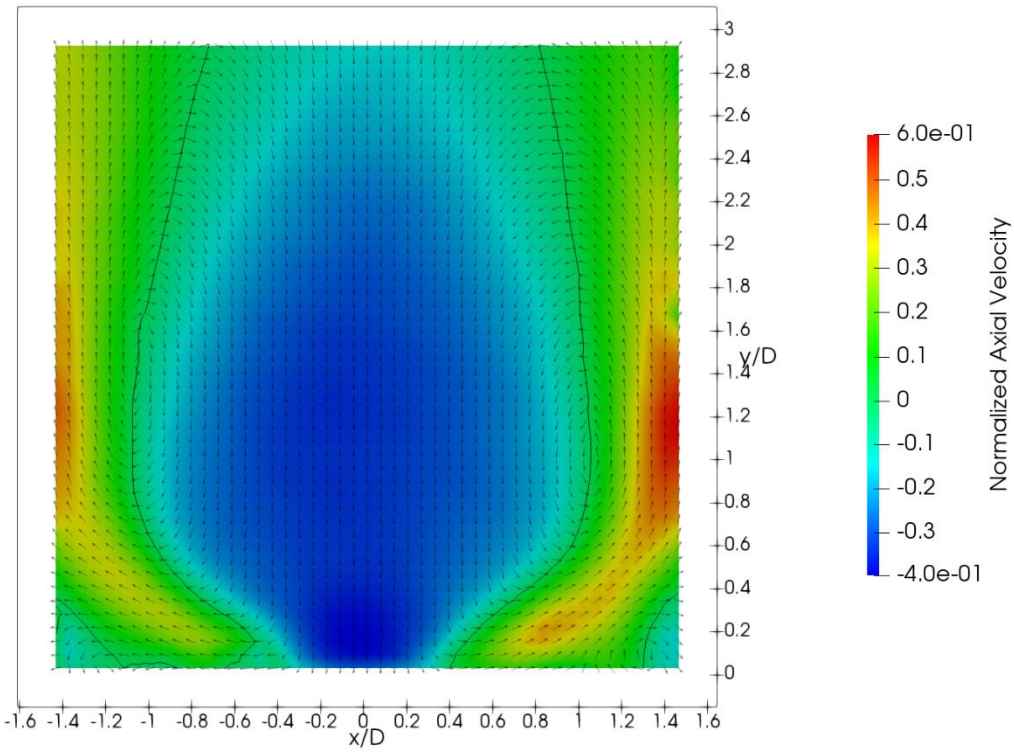

Figure A3: Normalized mean axial velocity mapping at Condition A5. Black line indicates contour of zero axial velocity.

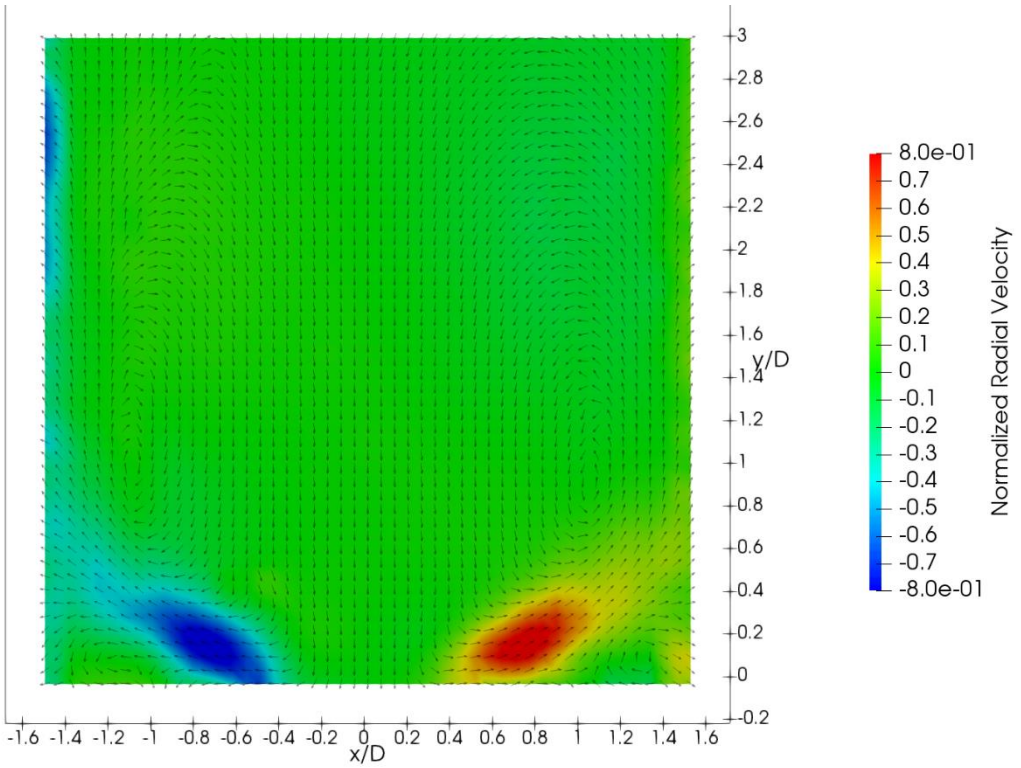

Figure A4: Normalized mean radial velocity mapping at Condition A2.

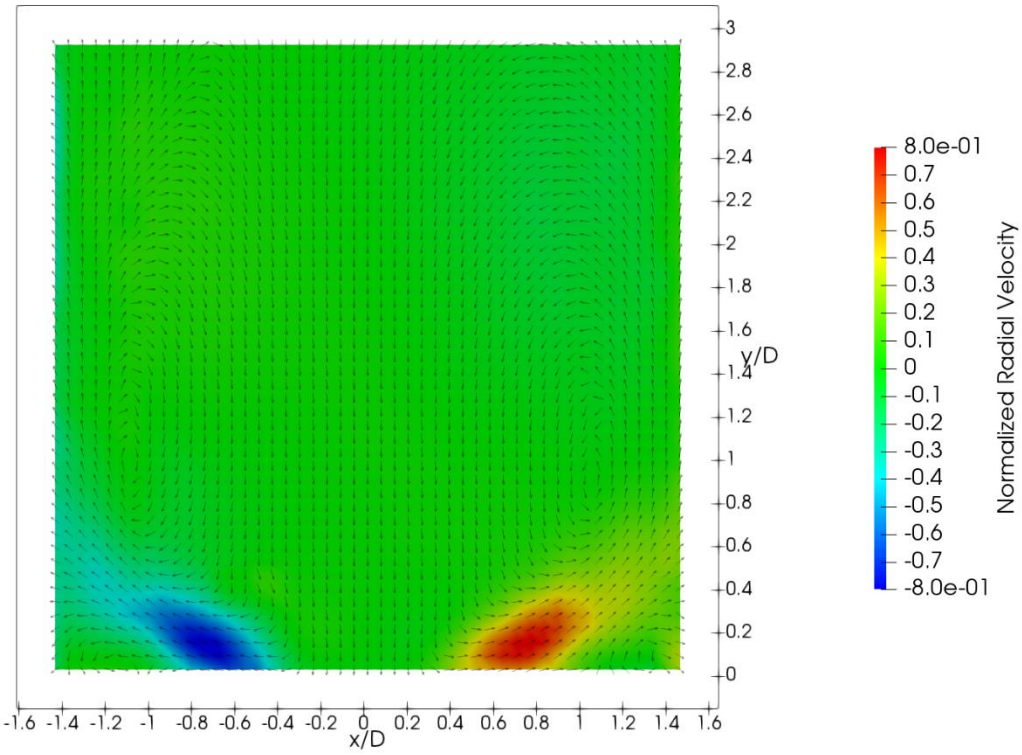

Figure A5: Normalized mean radial velocity mapping at Condition A3.

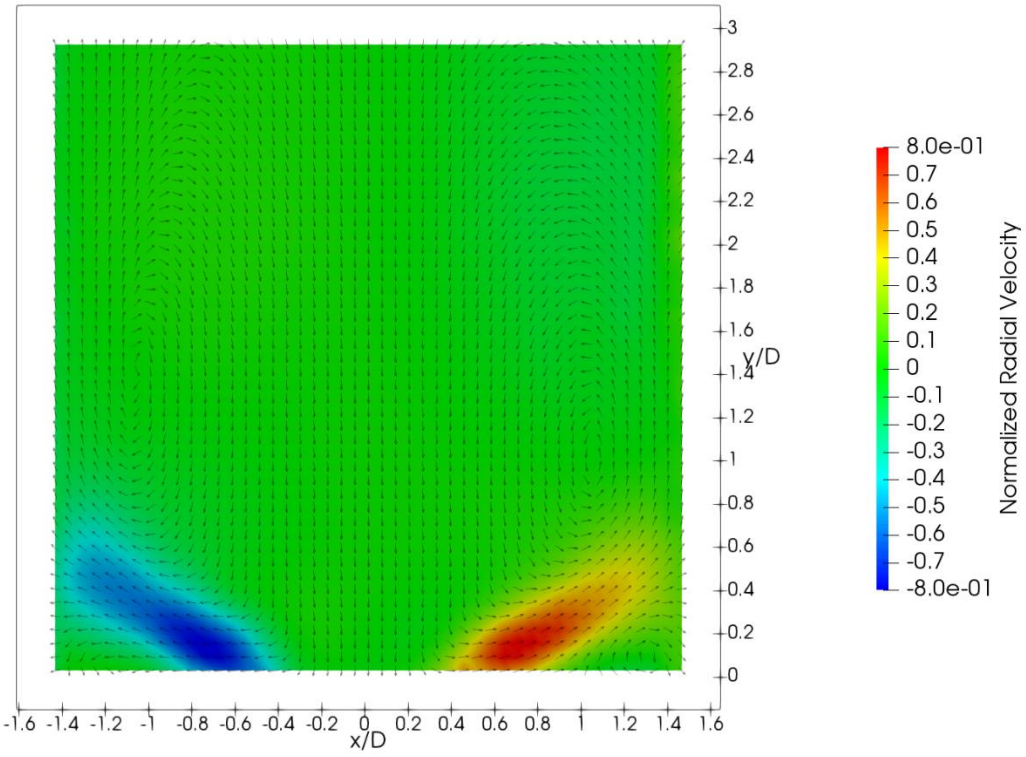

Figure A6: Normalized mean radial velocity mapping at Condition A5.

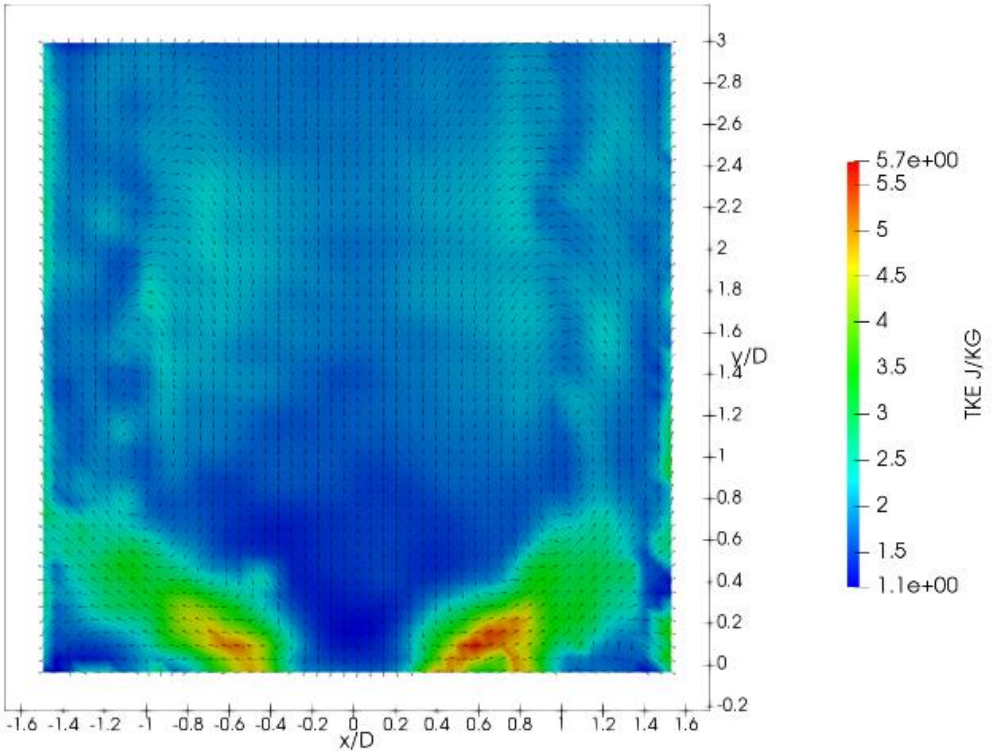

Figure A7: Turbulent kinetic energy mapping of Condition A2.

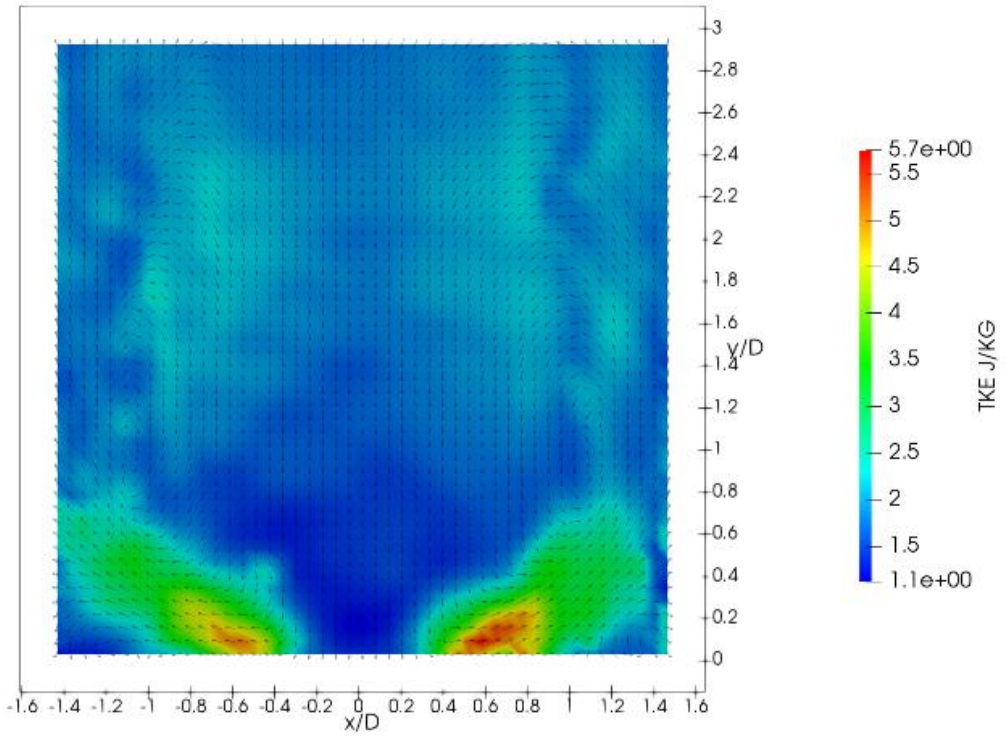

Figure A8: Turbulent kinetic energy mapping of Condition A3.

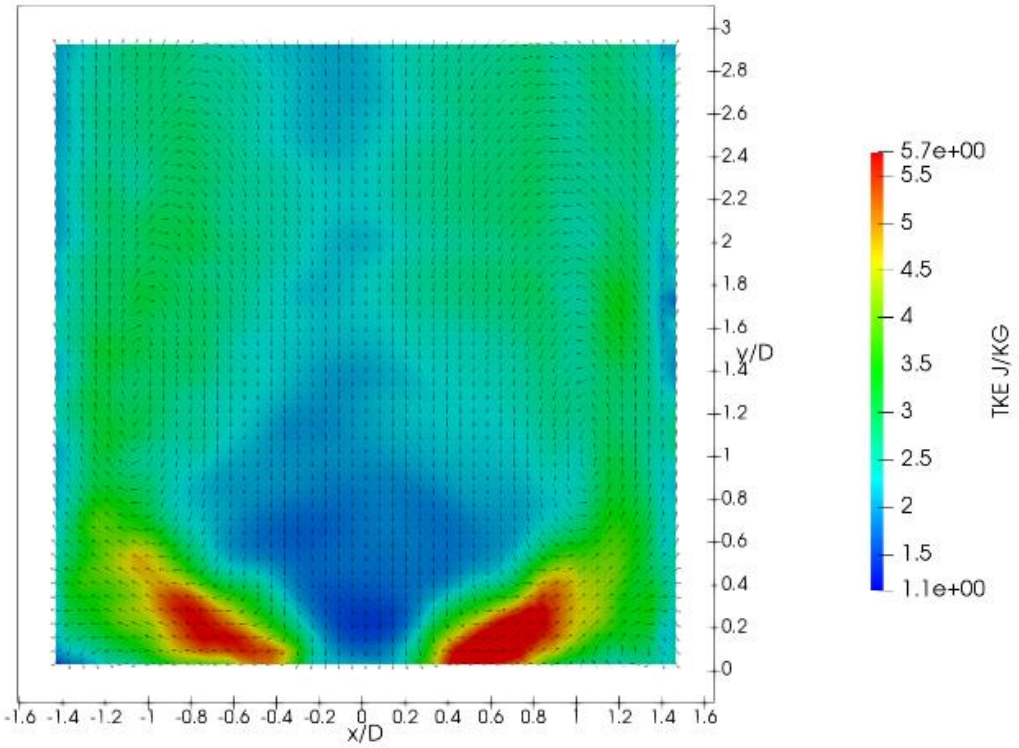

Figure A9: Turbulent kinetic energy mapping of Condition A5.

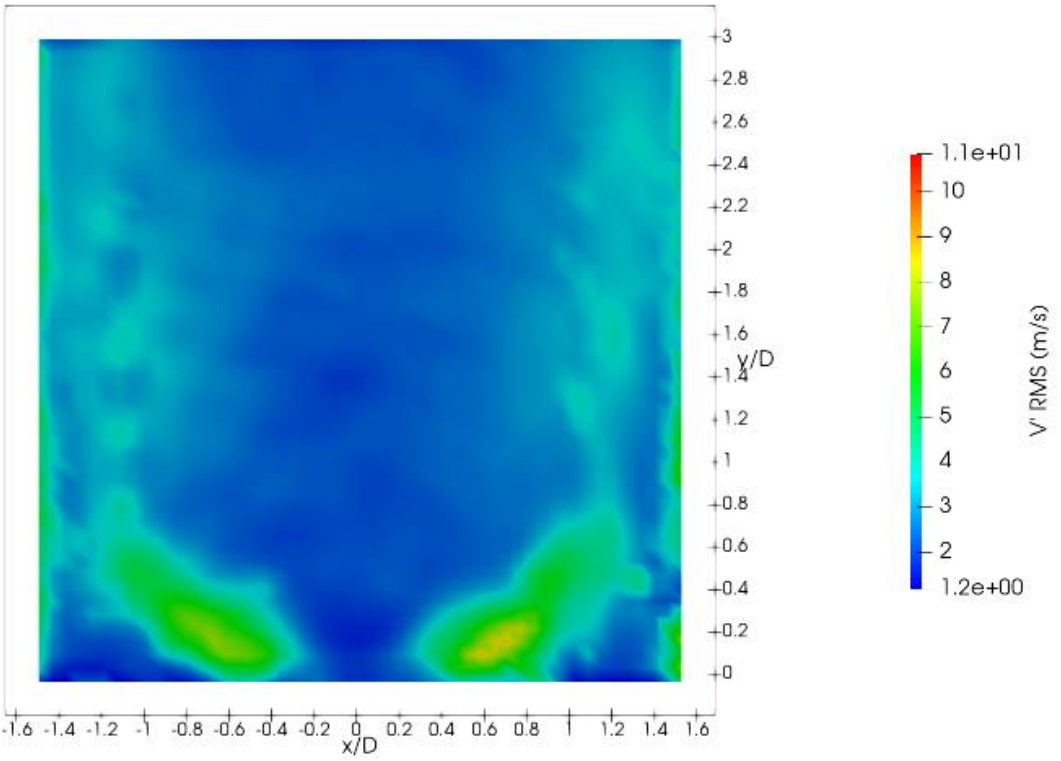

Figure A10: Mapping of root-mean-square of axial velocity fluctuations at Condition A2.

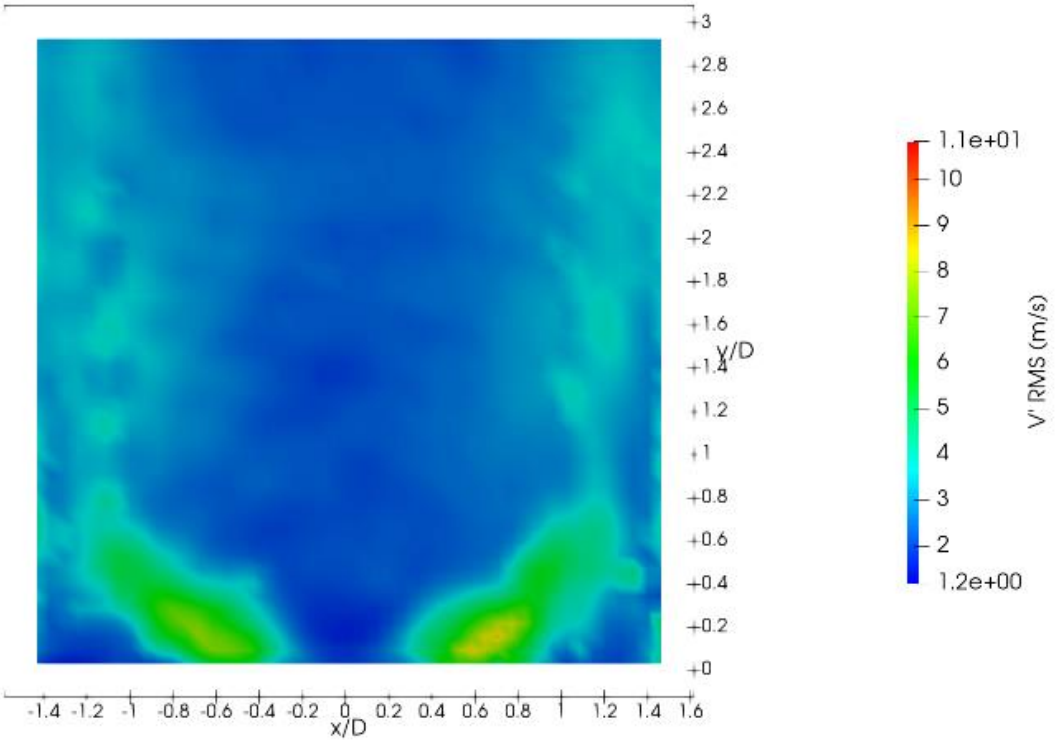

Figure A11: Mapping of root-mean-square of axial velocity fluctuations at Condition A3.

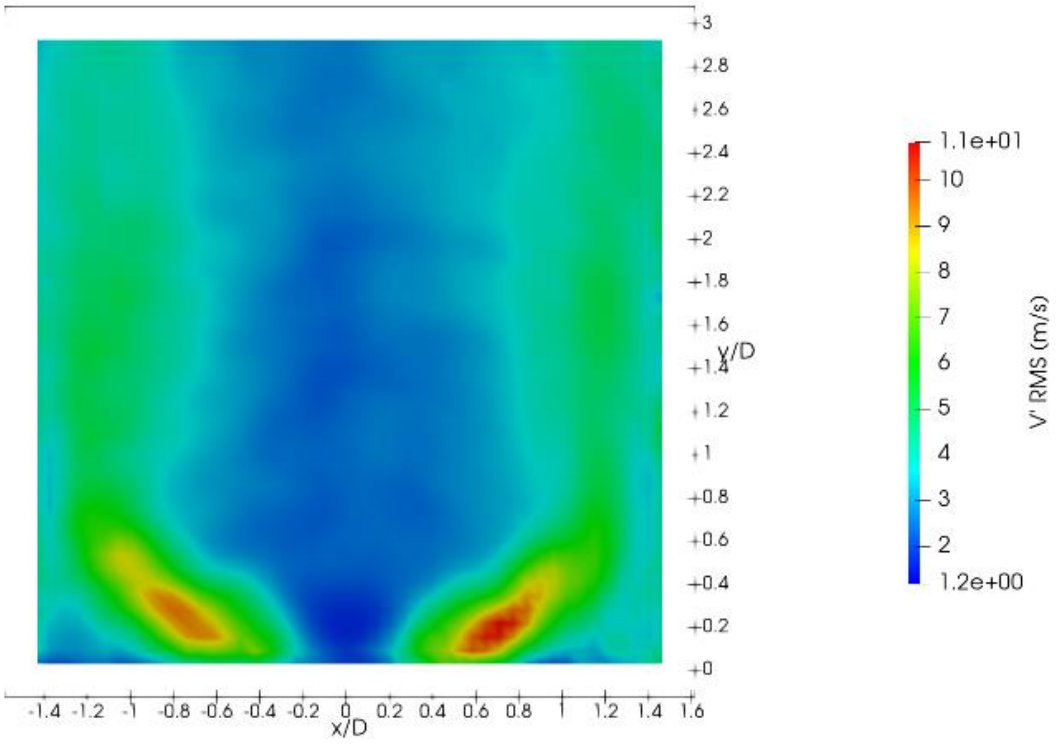

Figure A12: Mapping of root-mean-square of axial velocity fluctuations at Condition A5.

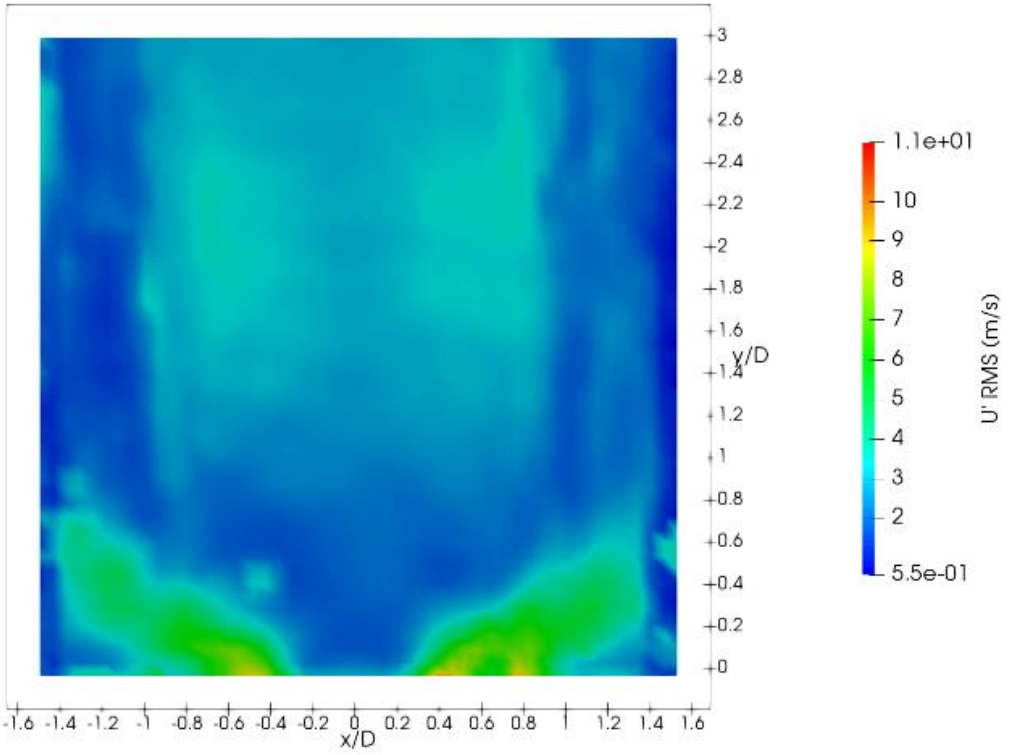

Figure A13: Mapping of root-mean-square of radial velocity fluctuations at Condition A2.

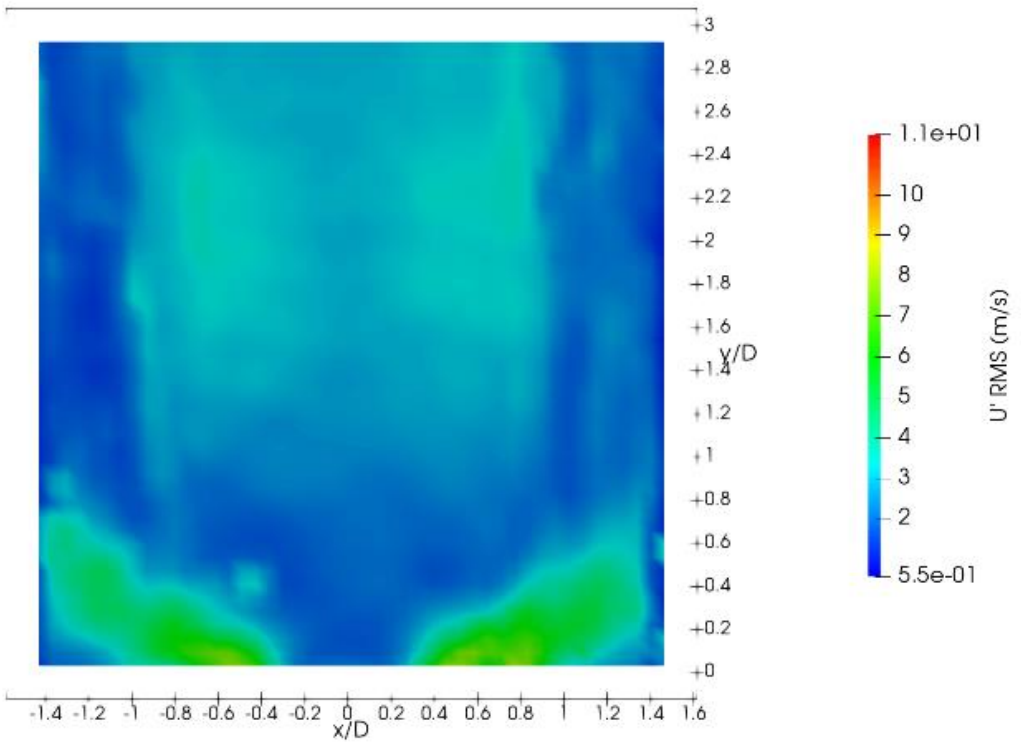

Figure A14: Mapping of root-mean-square of radial velocity fluctuations at Condition A3.

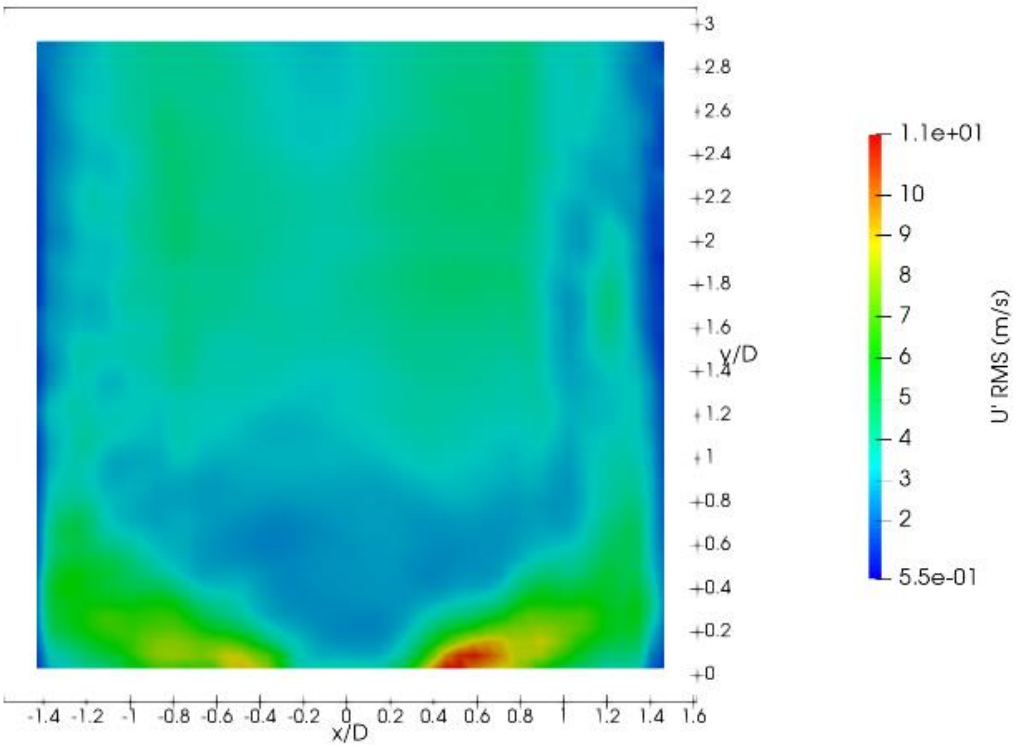

Figure A15: Mapping of root-mean-square of radial velocity fluctuations at Condition A5.

APPENDIX B: Nonreacting PIV Results of Second Mounting

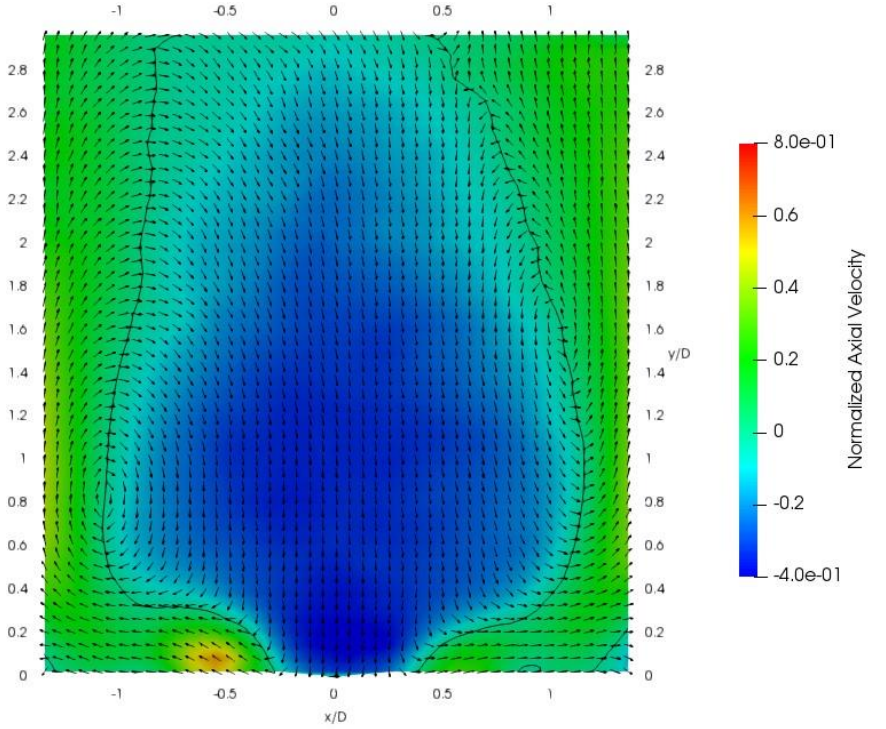

Figure B1: Axial velocity profile at Condition A2 (2% ΔP), location V1. Black line indicates contour of zero axial velocity.

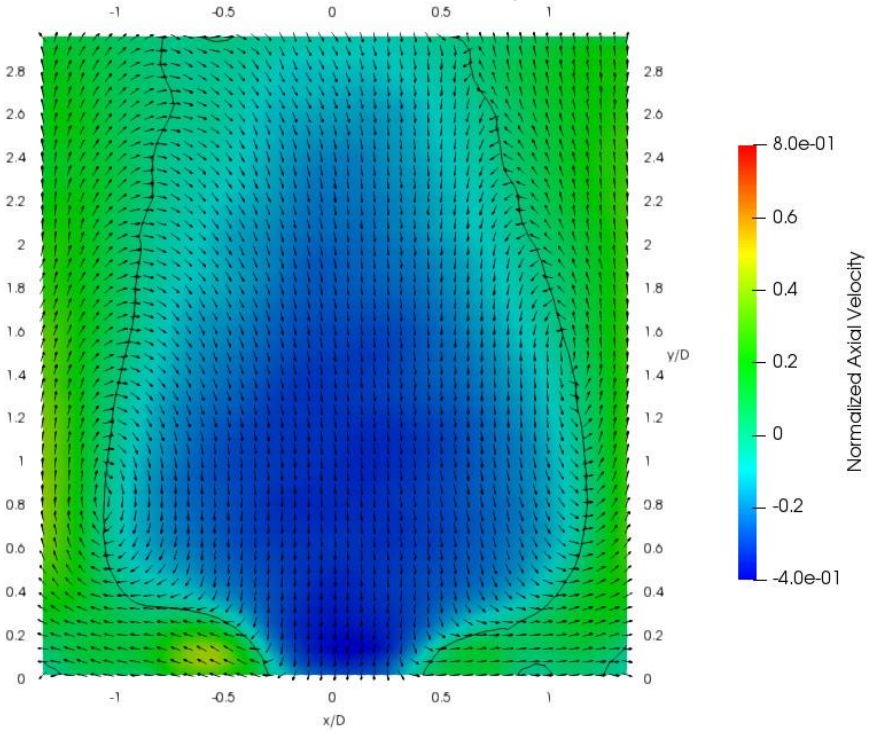

Figure B2: Axial velocity profile at Condition A4 (3% ΔP), location V1. Black line indicates contour of zero axial velocity.

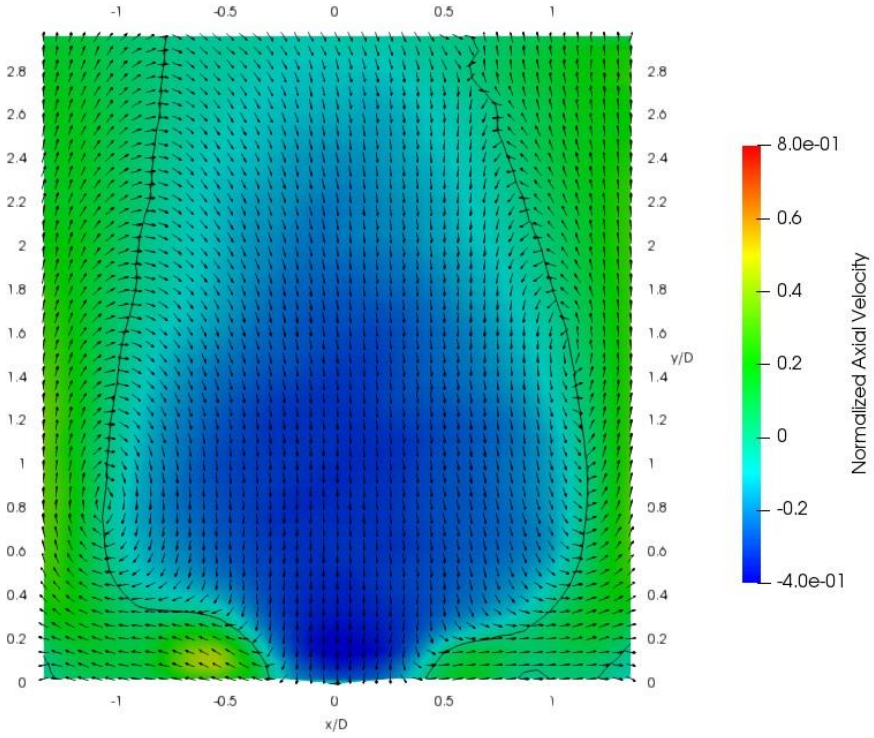

Figure B3: Axial velocity profile at Condition A5 (4% ΔP), location V1. Black line indicates contour of zero axial velocity.

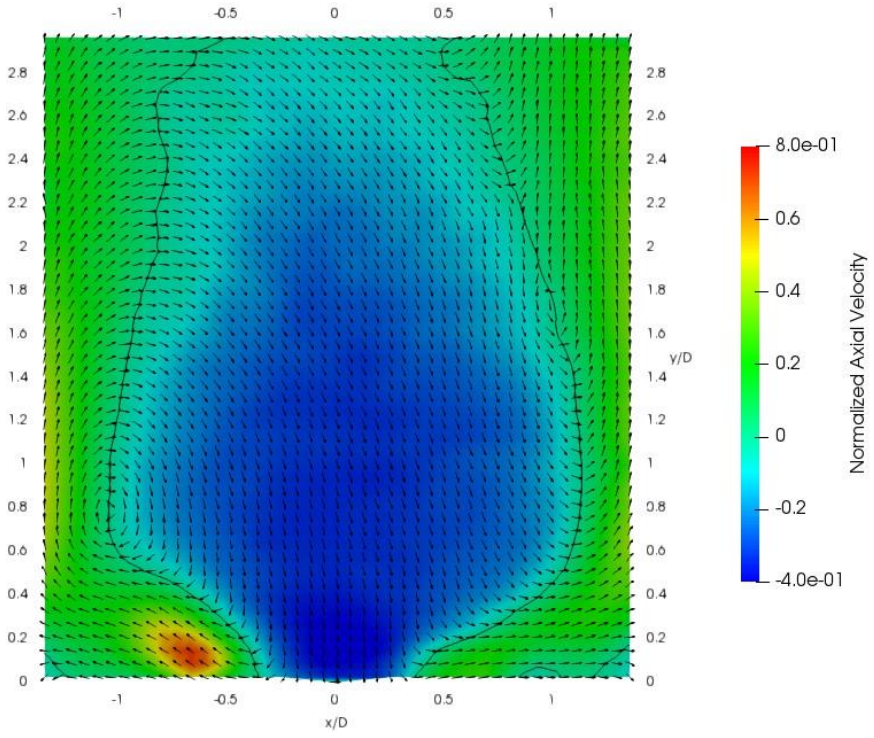

Figure B4: Axial velocity profile at Condition A2 (2% ΔP), location V2. Black line indicates contour of zero axial velocity.

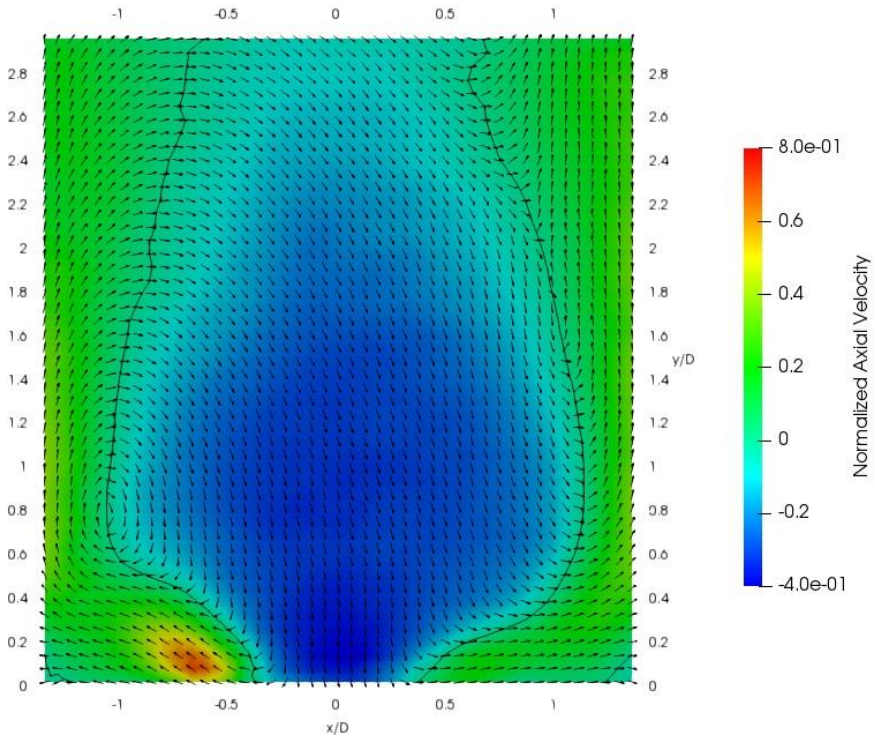

Figure B5: Axial velocity profile at Condition A4 (3% ΔP), location V2. Black line indicates contour of zero axial velocity.

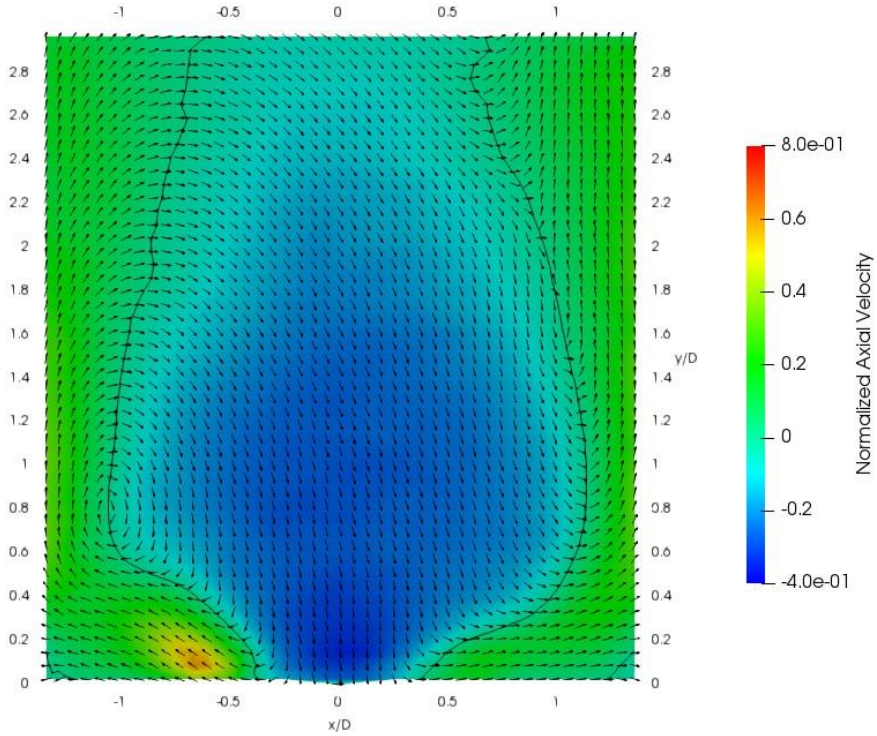

Figure B6: Axial velocity profile at Condition A5 (4% ΔP), location V2. Black line indicates contour of zero axial velocity.

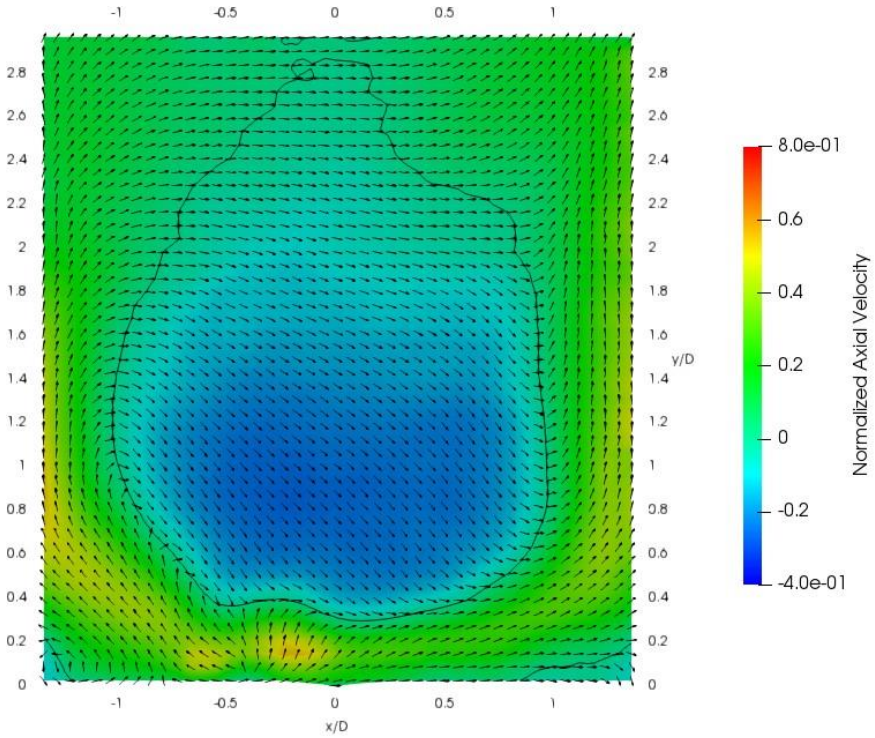

Figure B7: Axial velocity profile at Condition A2 (2% ΔP), location V3. Black line indicates contour of zero axial velocity.

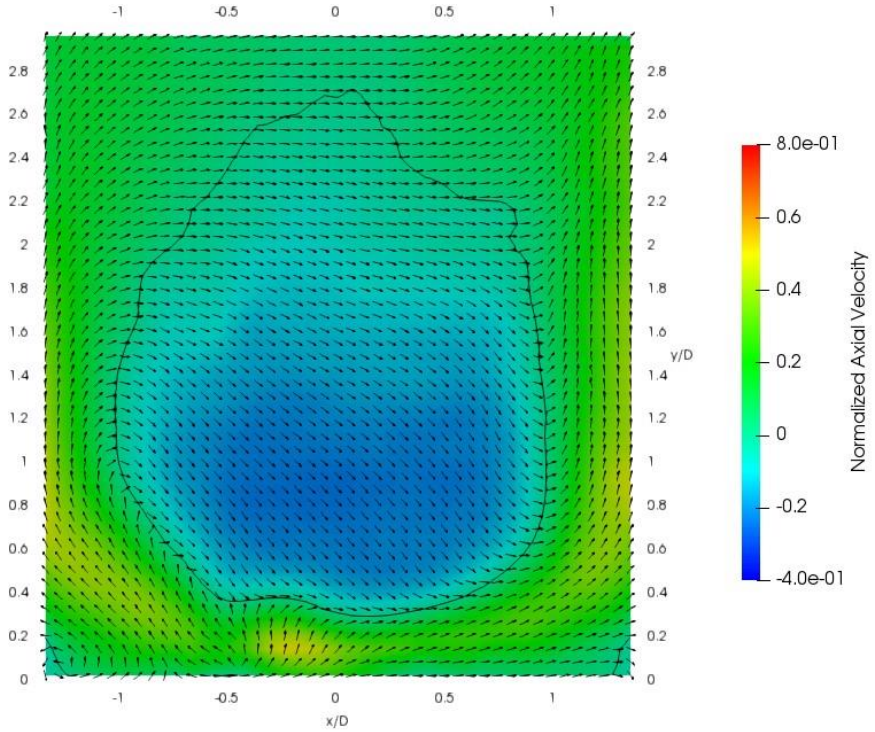

Figure B8: Axial velocity profile at Condition A4 (3% ΔP), location V3. Black line indicates contour of zero axial velocity.

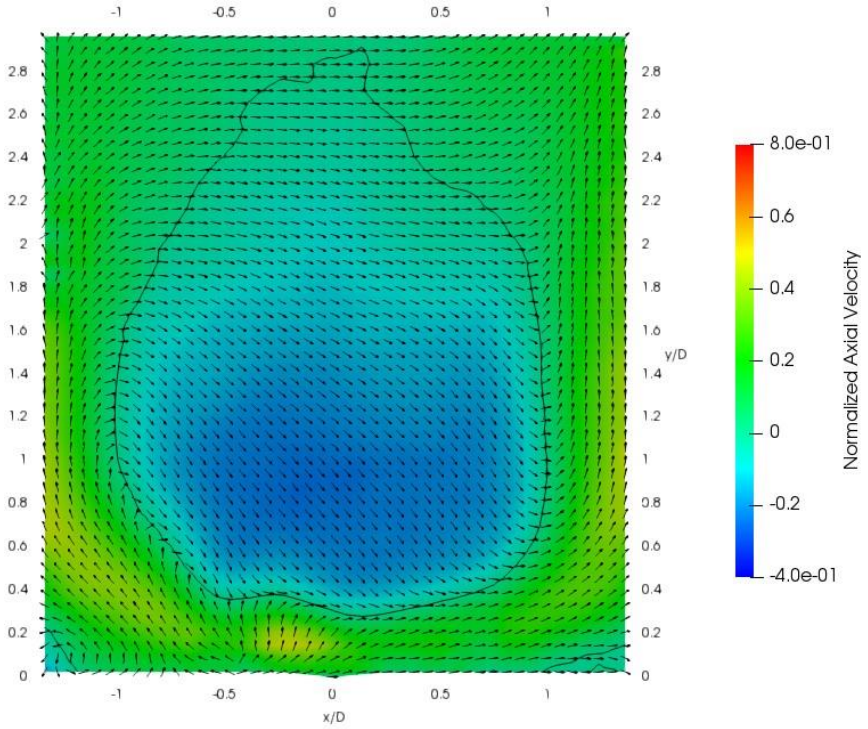

Figure B9: Axial velocity profile at Condition A5 (4% ΔP), location V3. Black line indicates contour of zero axial velocity.

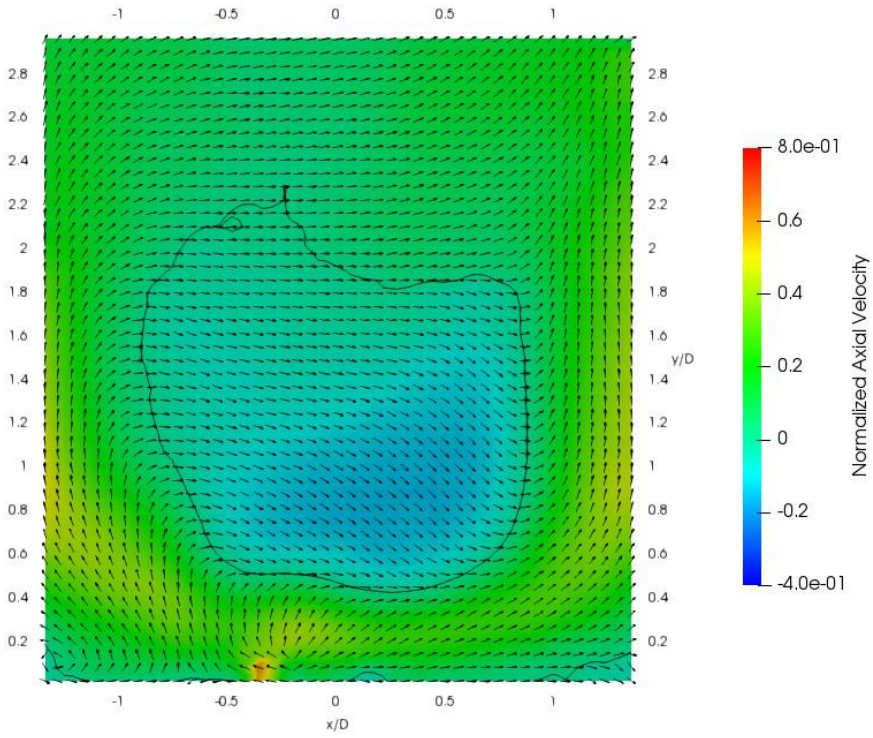

Figure B10: Axial velocity profile at Condition A4 (3%ΔP), location V4. Black line indicates contour of zero axial velocity.

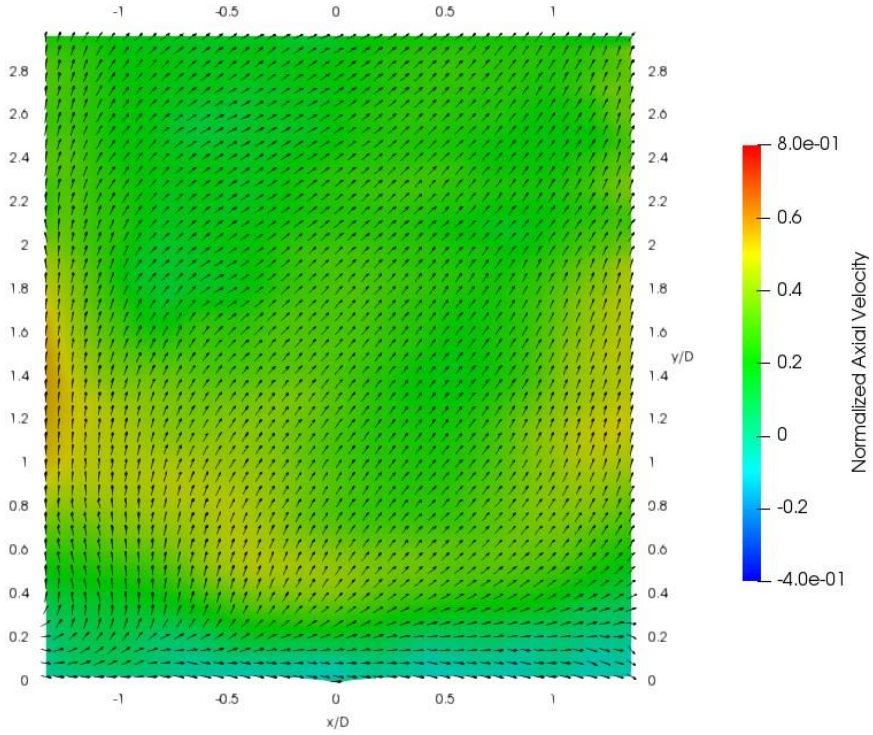

Figure B11: Axial velocity profile at Condition A2 (2%ΔP), location V5.

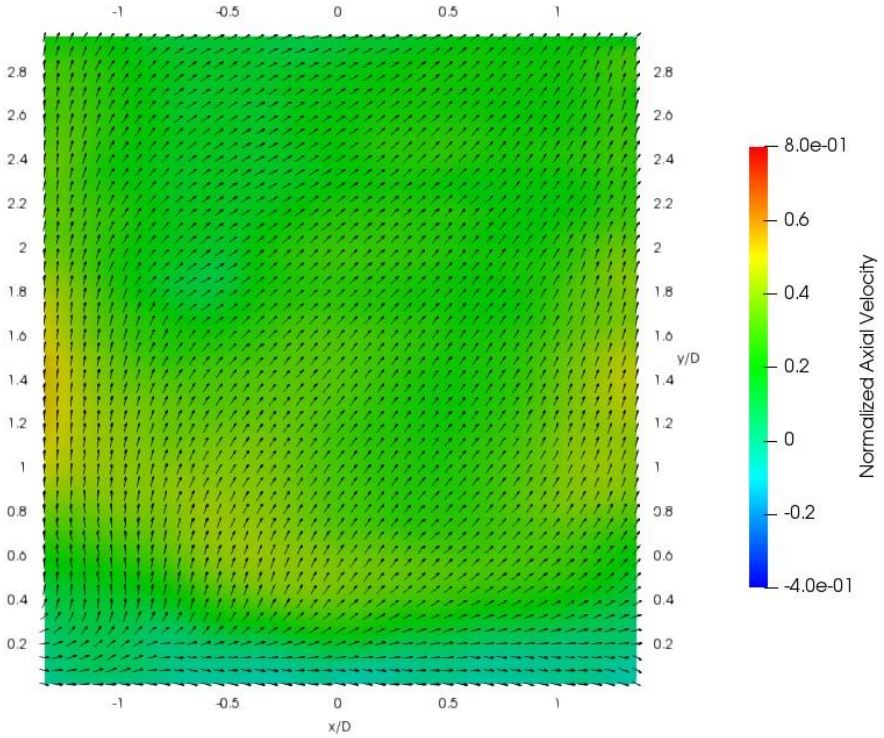

Figure B12: Axial velocity profile at Condition A4 (3% ΔP), location V5.

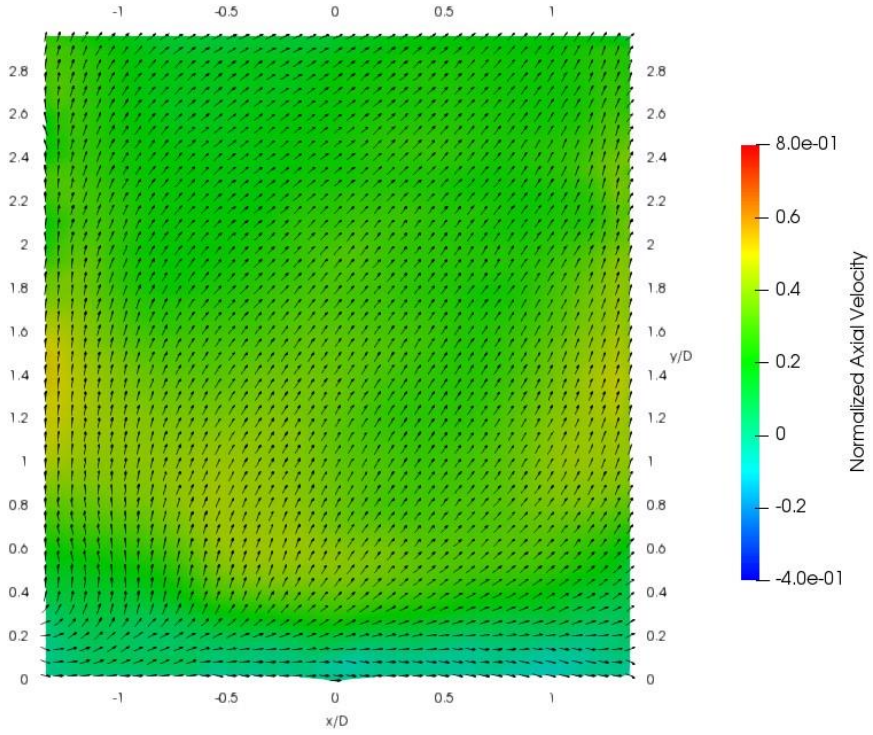

Figure B13: Axial velocity profile at Condition A5 (4% ΔP), location V5.

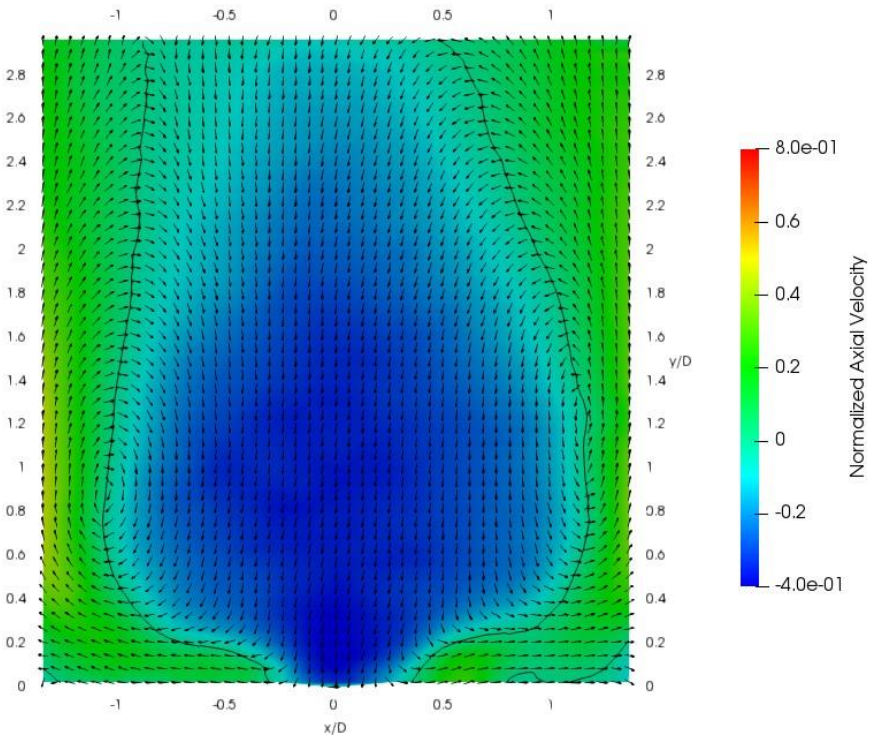

Figure B14: Axial Velocity Profile at Condition A2 (2%ΔP), location V6. Black line indicates contour of zero axial velocity.

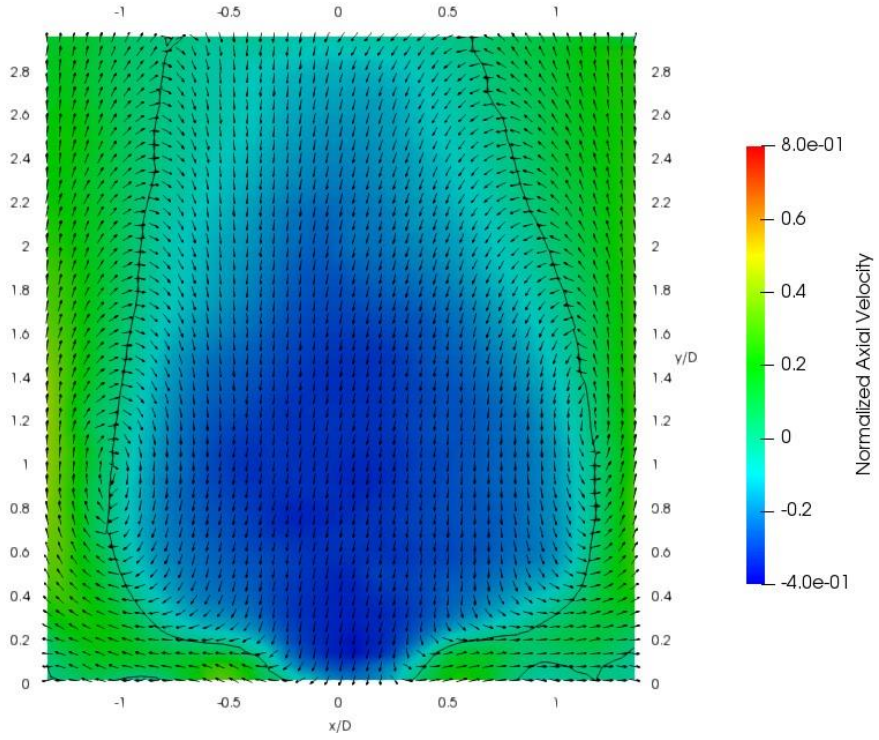

Figure B15: Axial velocity profile at Condition A4 (3%ΔP), location V6. Black line indicates contour of zero axial velocity.

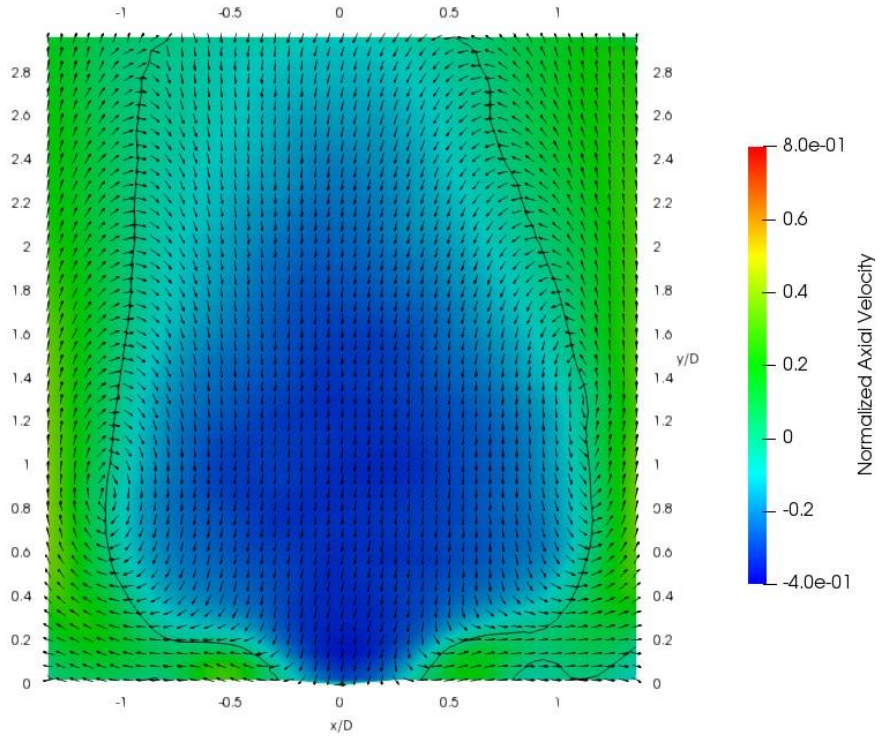

Figure B16: Axial velocity profile at Condition A5 (4%ΔP), location V6. Black line indicates contour of zero axial velocity.

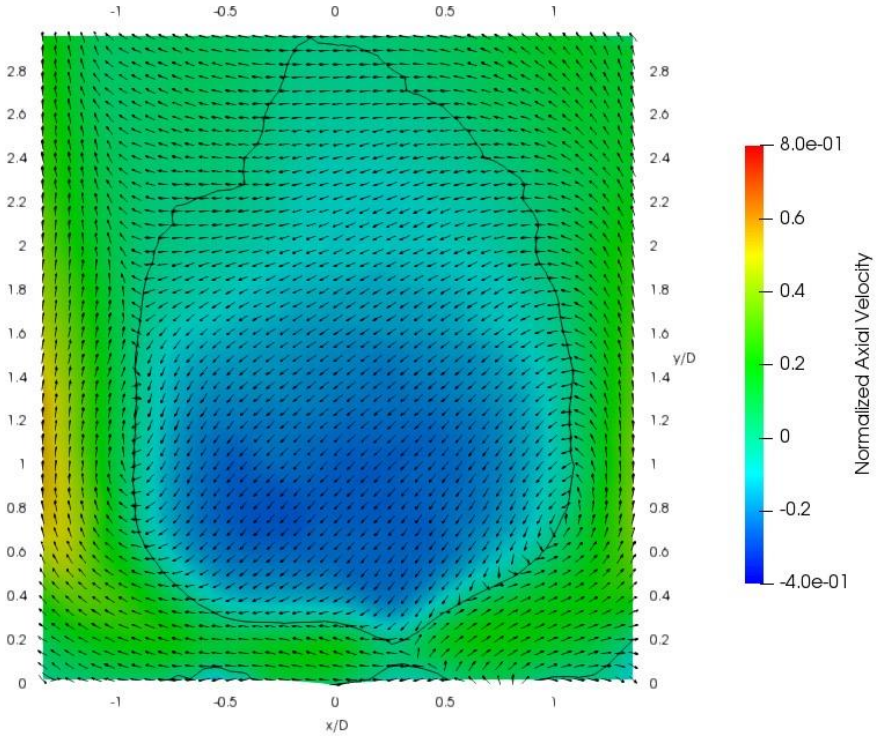

Figure B17: Axial velocity profile at Condition A2 (2%ΔP), location V7. Black line indicates contour of zero axial velocity.

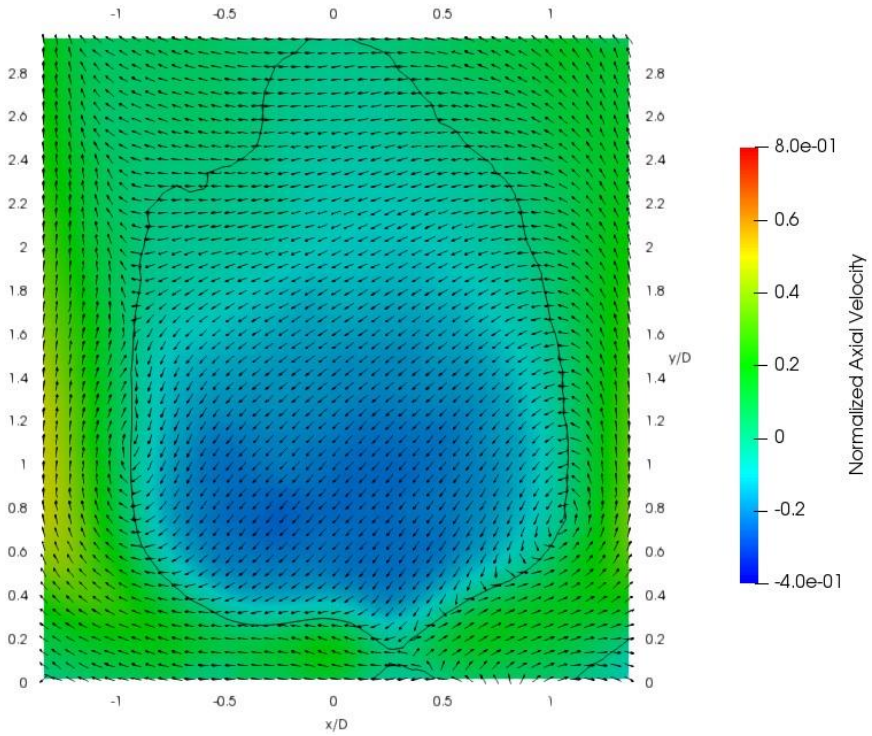

Figure B18: Axial velocity profile at Condition A4 (3%ΔP), location V7. Black line indicates contour of zero axial velocity.

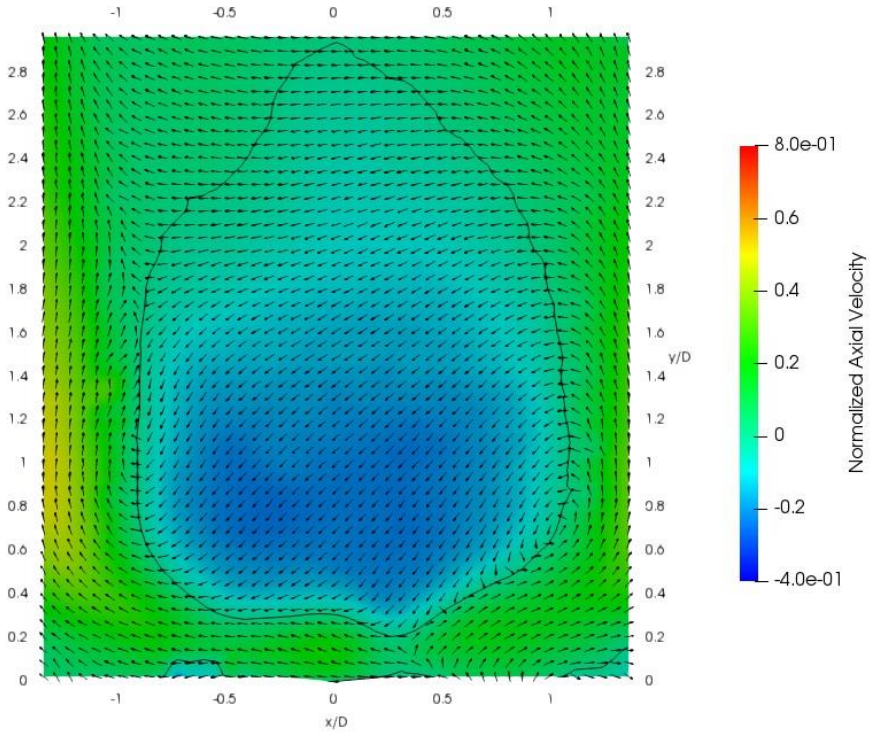

Figure B19: Axial velocity profile at Condition A5 (4%ΔP), location V7. Black line indicates contour of zero axial velocity.

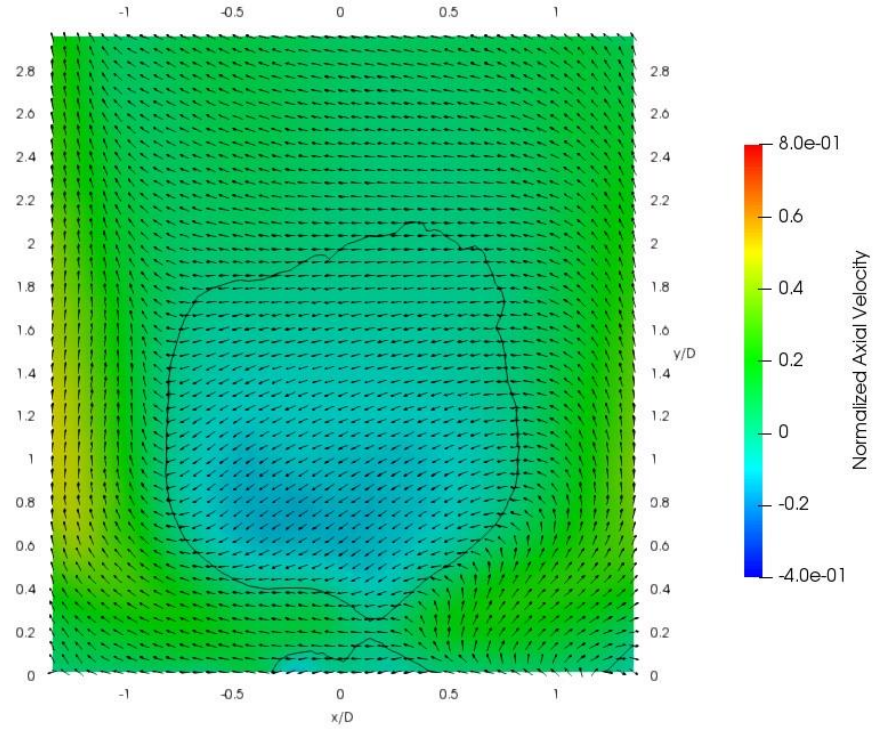

Figure B20: Axial velocity profile at Condition A4 (3% ΔP), location V8. Black line indicates contour of zero axial velocity.

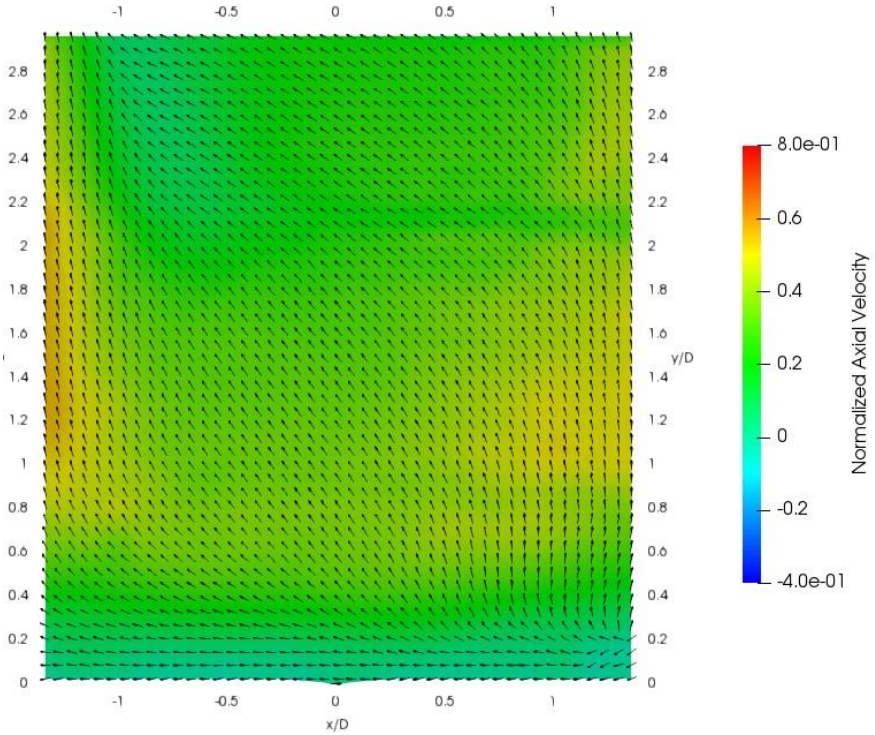

Figure B21: Axial velocity profile at Condition A2 (2% ΔP), location V9.

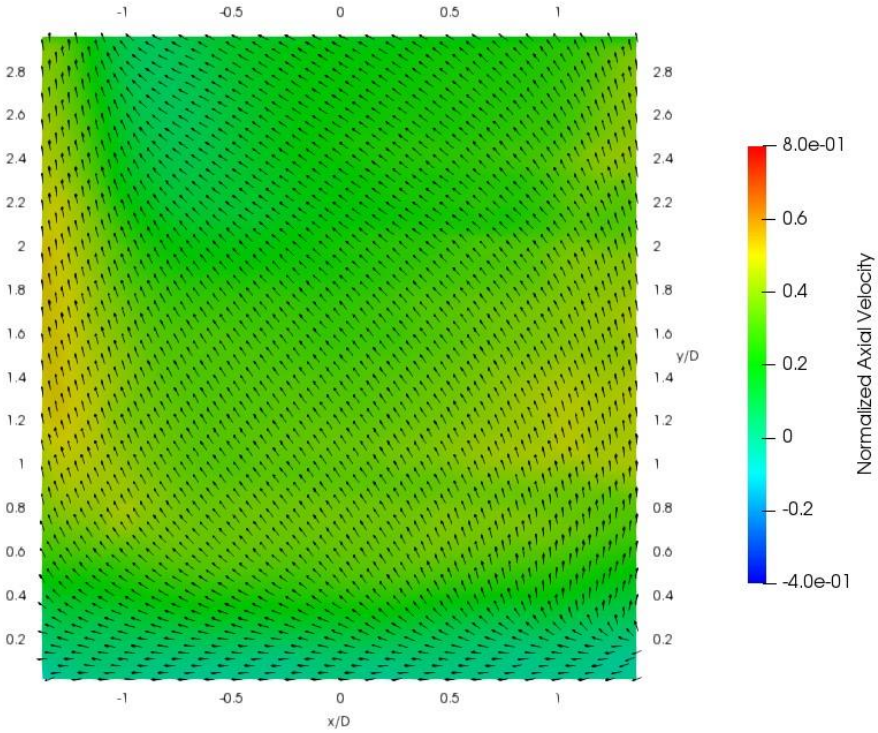

Figure B22: Axial velocity profile at Condition A4 (3% ΔP), location V9.

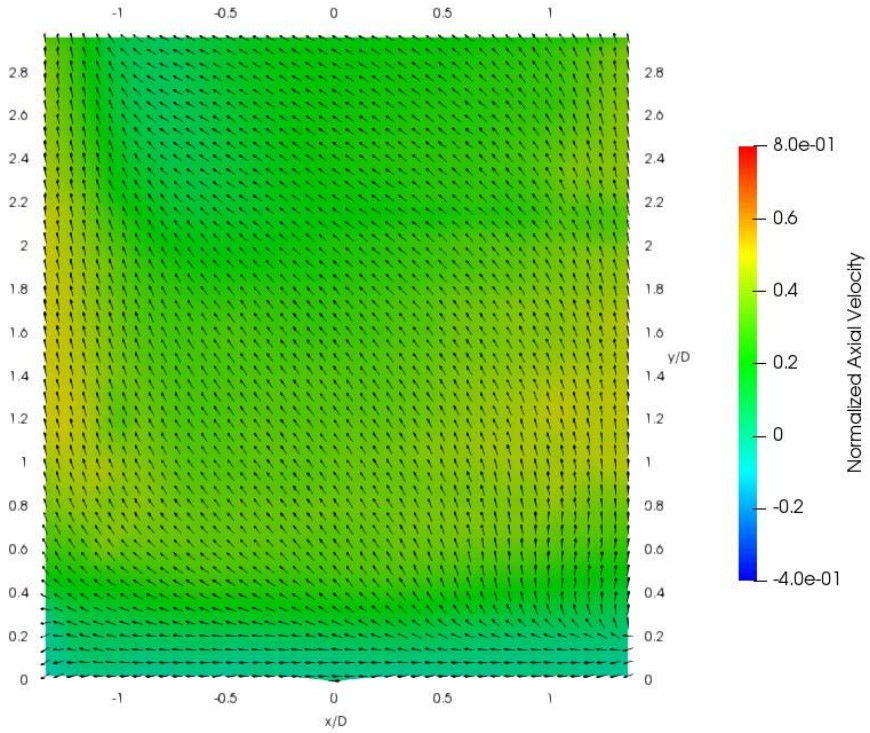

Figure B23: Axial velocity profile at Condition A5 (4% ΔP), location V9.

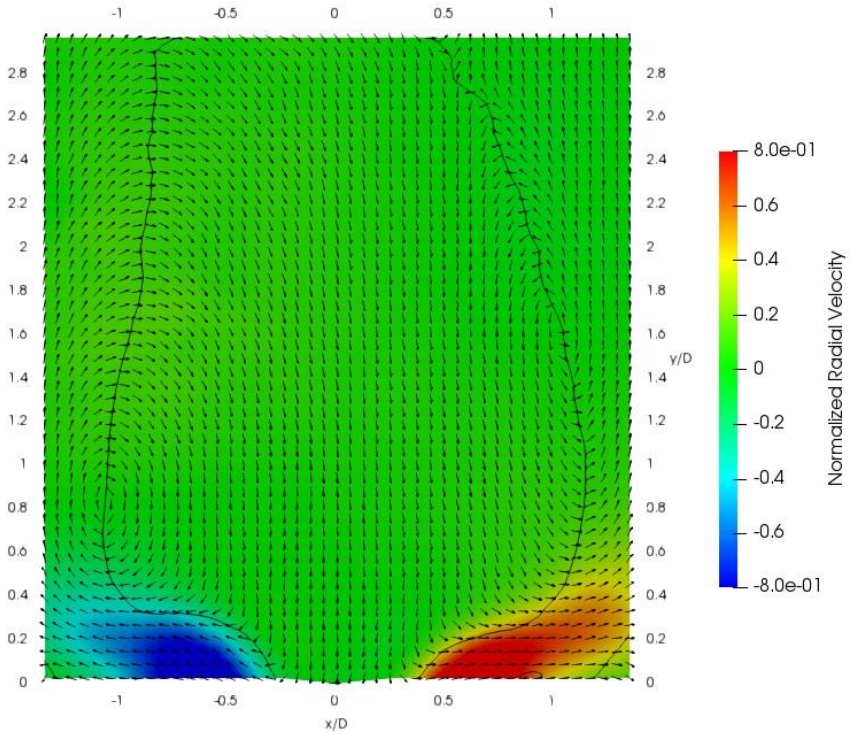

Figure B24: Radial velocity profile at Condition A2 (2% ΔP), location V1. Black line indicates contour of zero axial velocity.

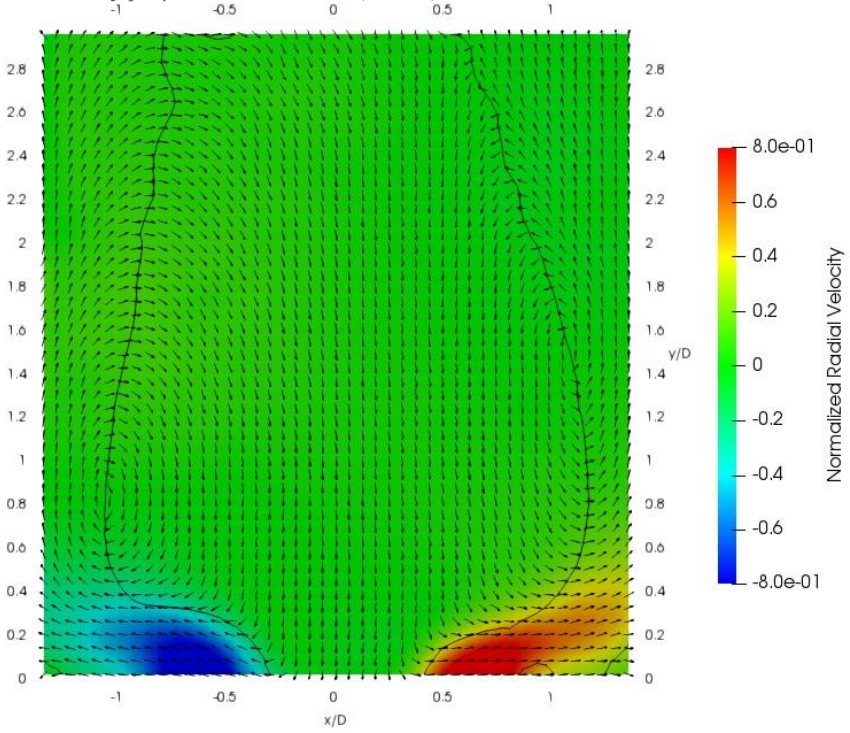

Figure B25: Radial velocity profile at Condition A4 (3% ΔP), location V1. Black line indicates contour of zero axial velocity.

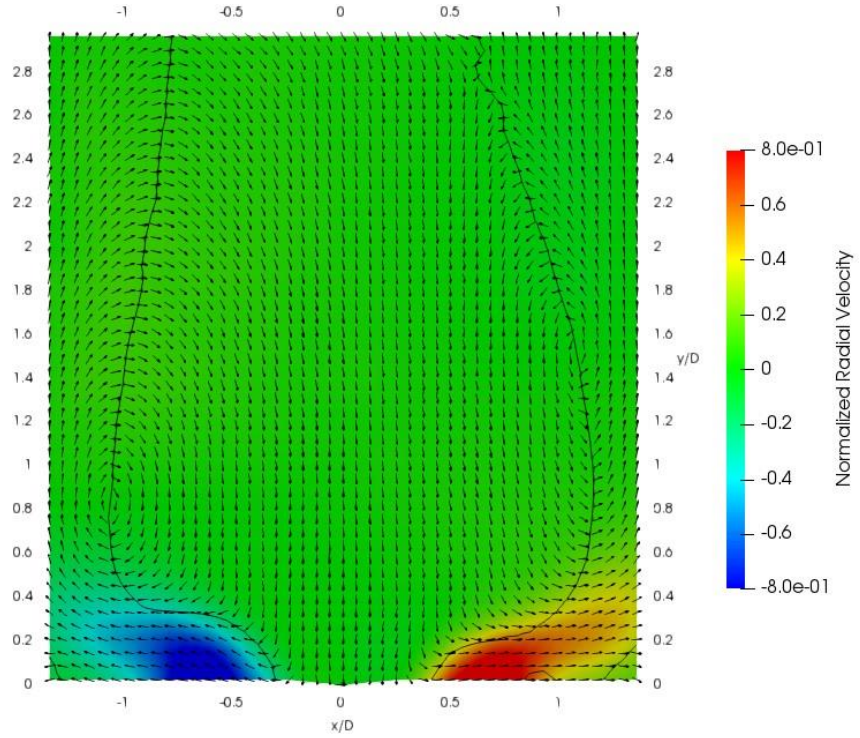

Figure B26: Radial velocity profile at Condition A5 (4% ΔP), location V1. Black line indicates contour of zero axial velocity.

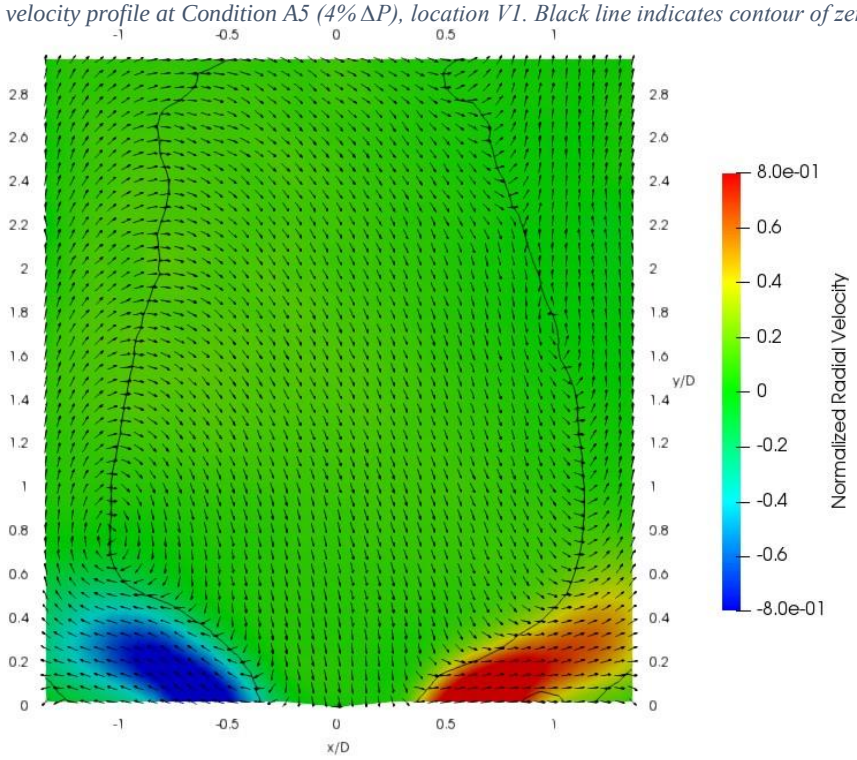

Figure B27: Radial velocity profile at Condition A2 (2% ΔP), location V2. Black line indicates contour of zero axial velocity.

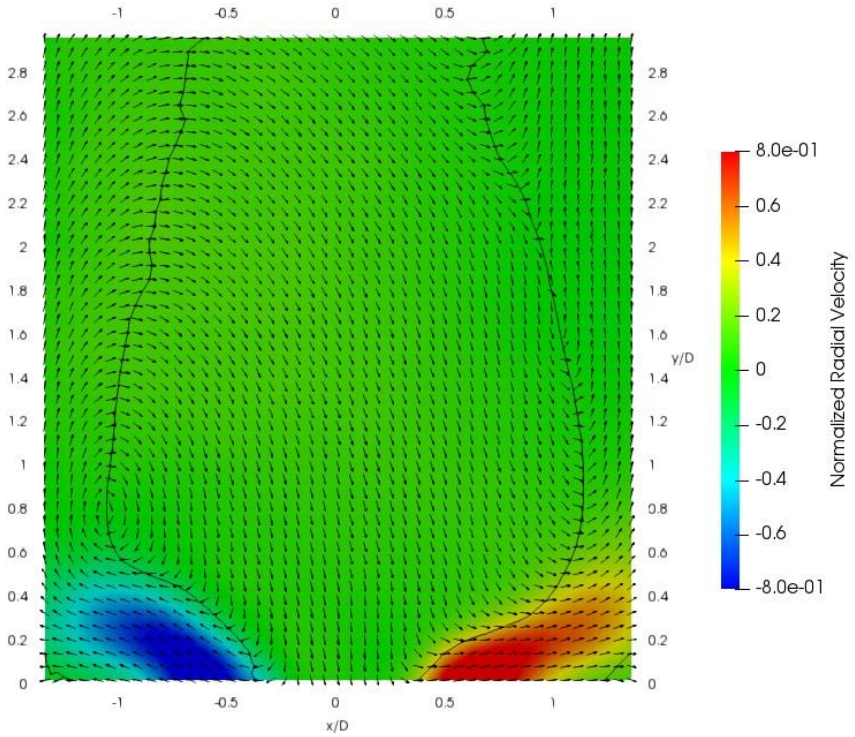

Figure B28: Radial velocity profile at Condition A4 (3% ΔP), location V2. Black line indicates contour of zero axial velocity.

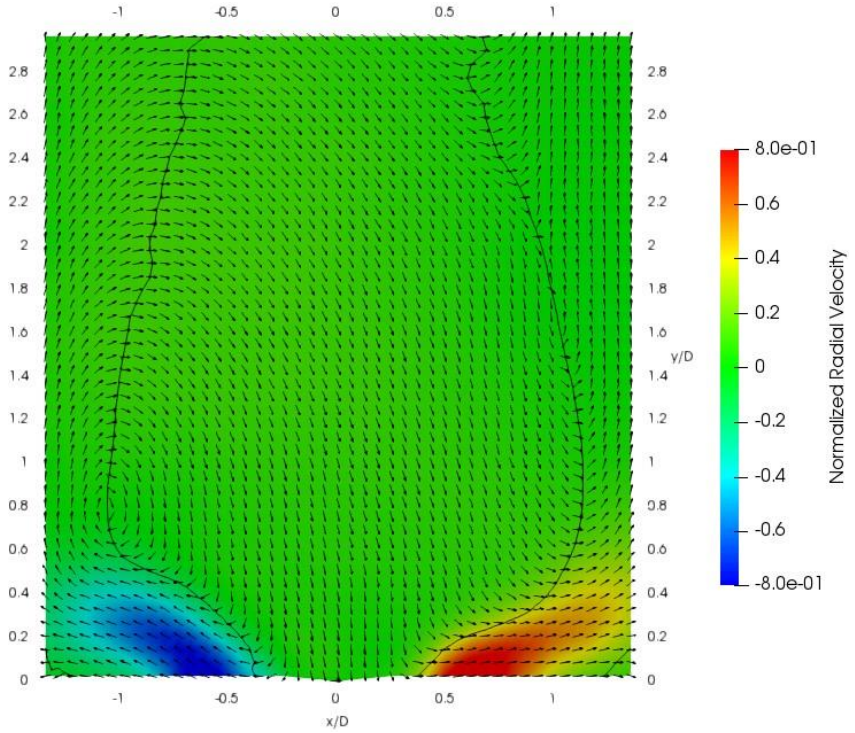

Figure B29: Radial velocity profile at Condition A5 (4% ΔP), location V2. Black line indicates contour of zero axial velocity.

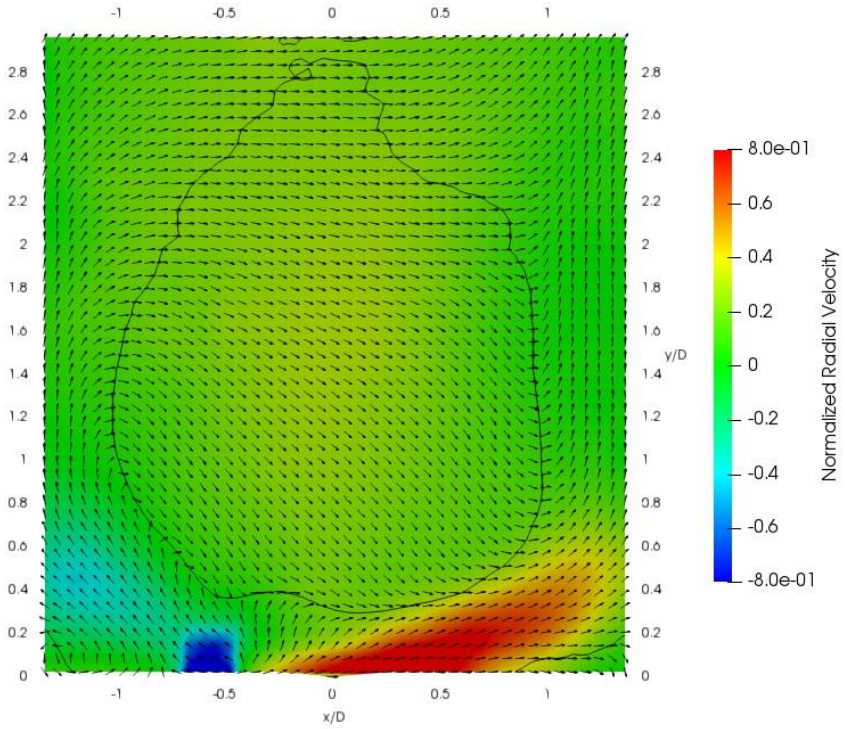

Figure B30: Radial velocity profile at Condition A2 (2% ΔP), location V3. Black line indicates contour of zero axial velocity.

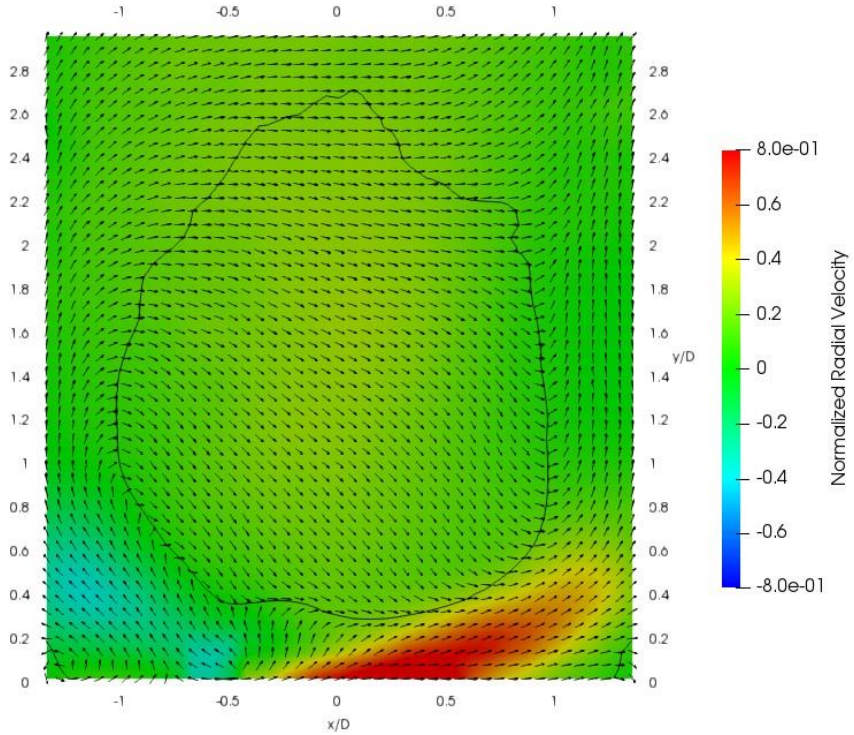

Figure B31: Radial velocity profile at Condition A4 (3% ΔP), location V3. Black line indicates contour of zero axial velocity.

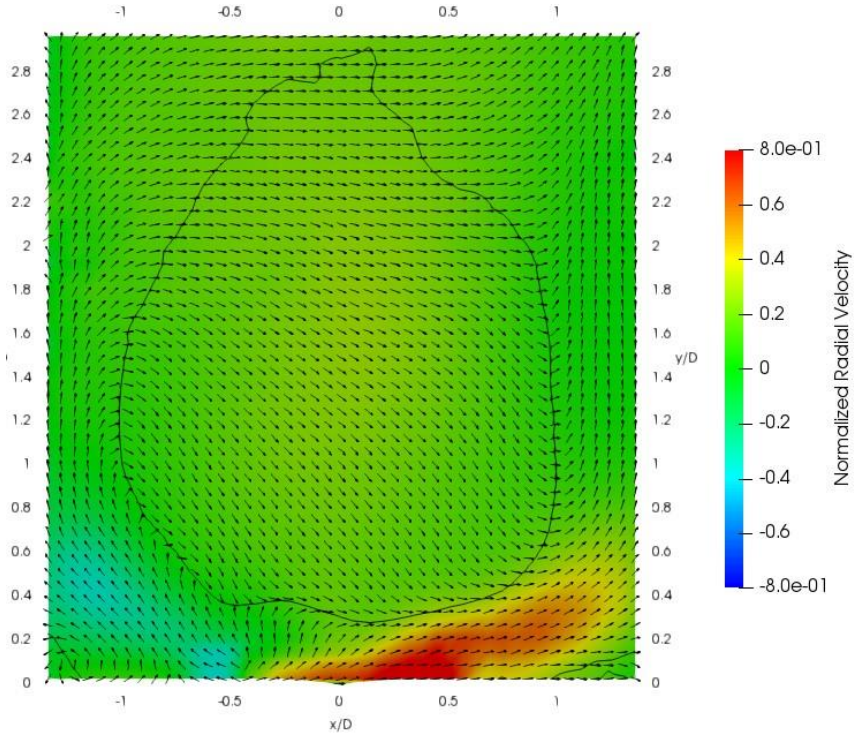

Figure B32: Radial velocity profile at Condition A5 (4% ΔP), location V3. Black line indicates contour of zero axial velocity.

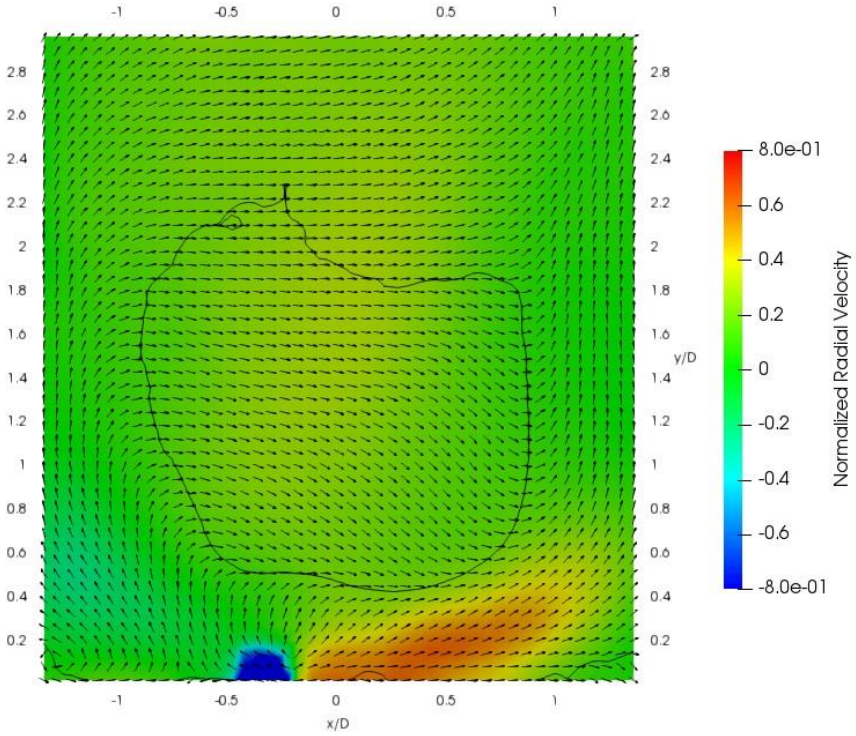

Figure B33: Radial velocity profile at Condition A4 (3% ΔP), location V4. Black line indicates contour of zero axial velocity.

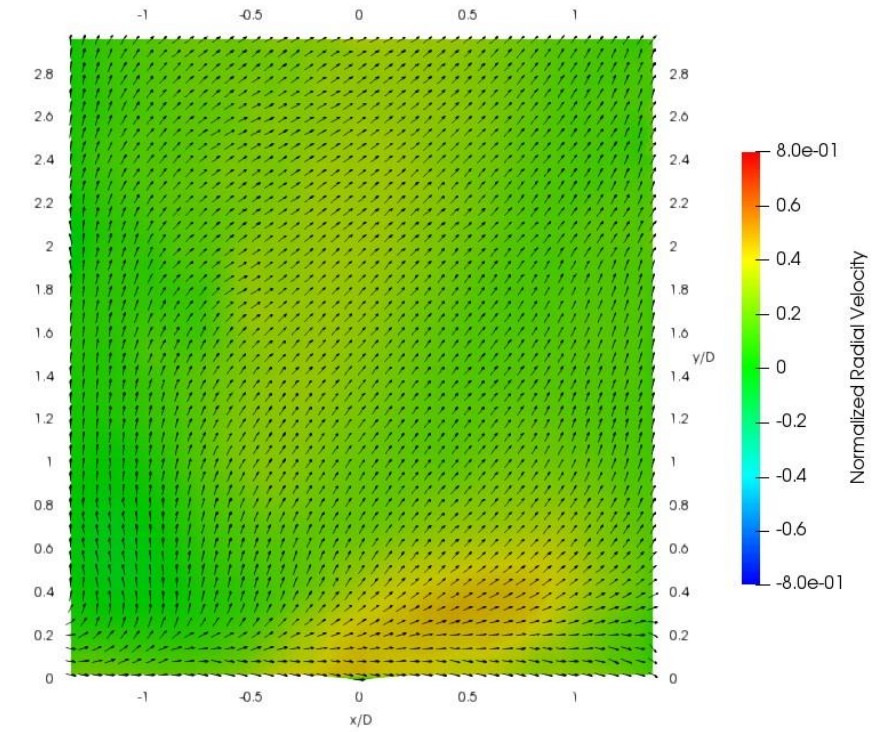

Figure B34: Radial Velocity profile at Condition A2 (2%ΔP), location V5.

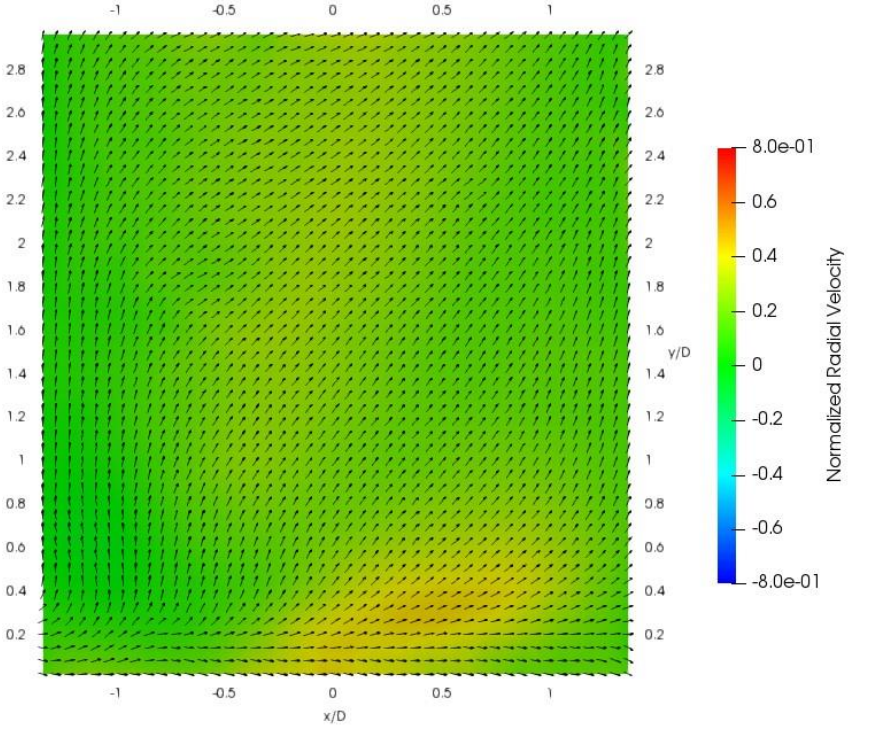

Figure B35: Radial velocity profile at Condition A4 (3%ΔP), location V5.

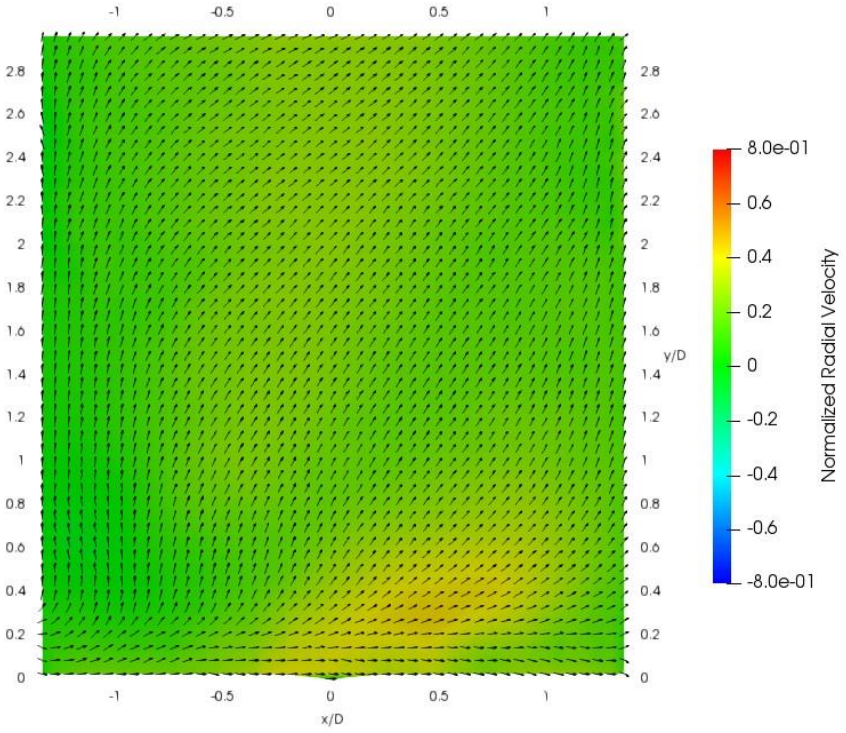

Figure B36: Radial velocity profile at Condition A5 (4% ΔP), location V5.

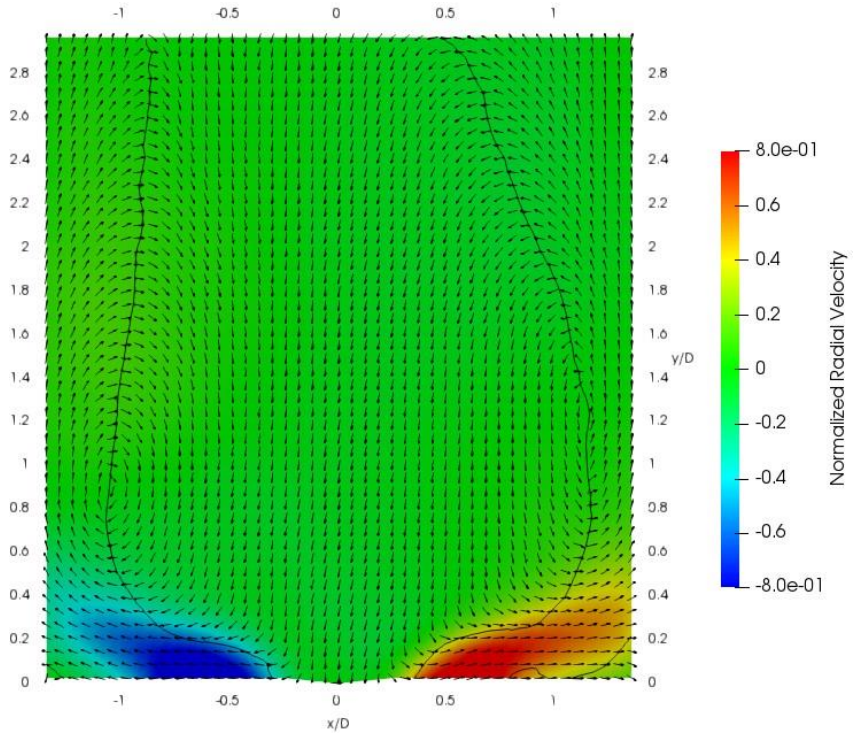

Figure B37: Radial velocity profile at Condition A2 (2% ΔP), location V6. Black line indicates contour of zero axial velocity.

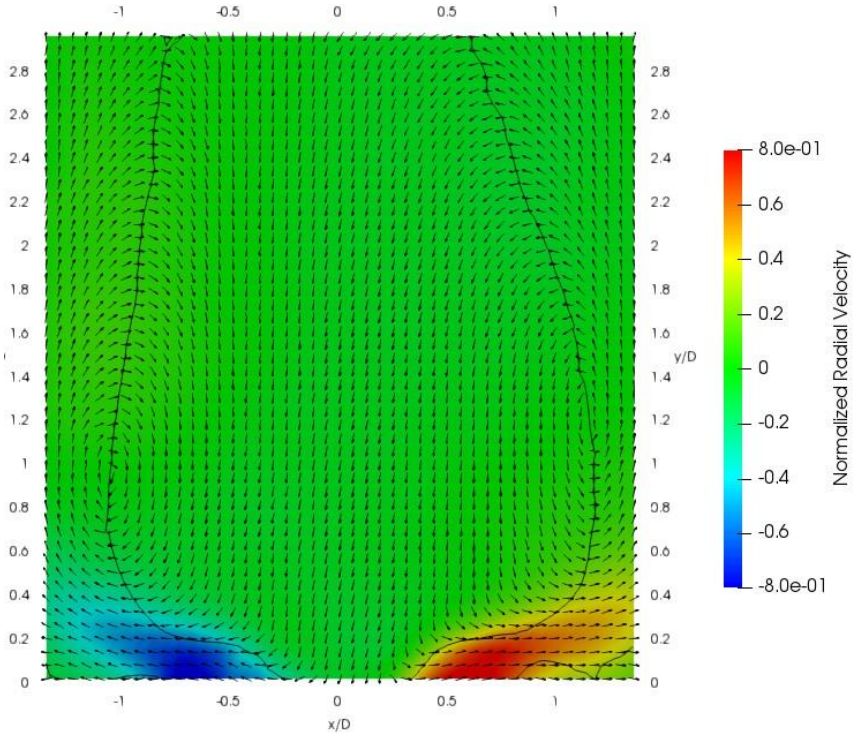

Figure B38: Radial velocity profile at Condition A4 (3% ΔP), location V6. Black line indicates contour of zero axial velocity.

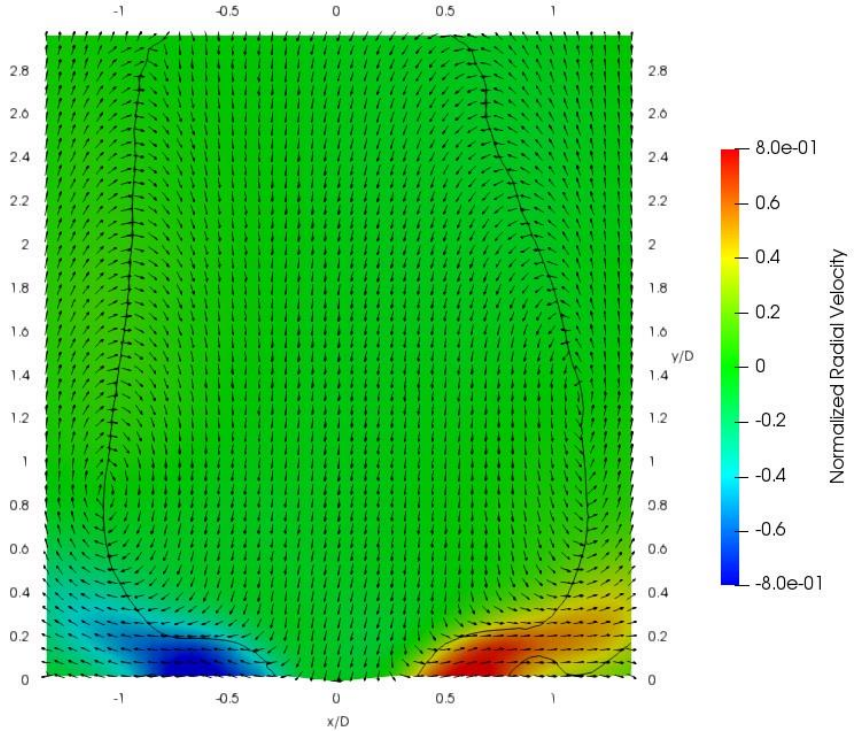

Figure B39: Radial velocity profile at Condition A5 (4% ΔP), location V6. Black line indicates contour of zero axial velocity.

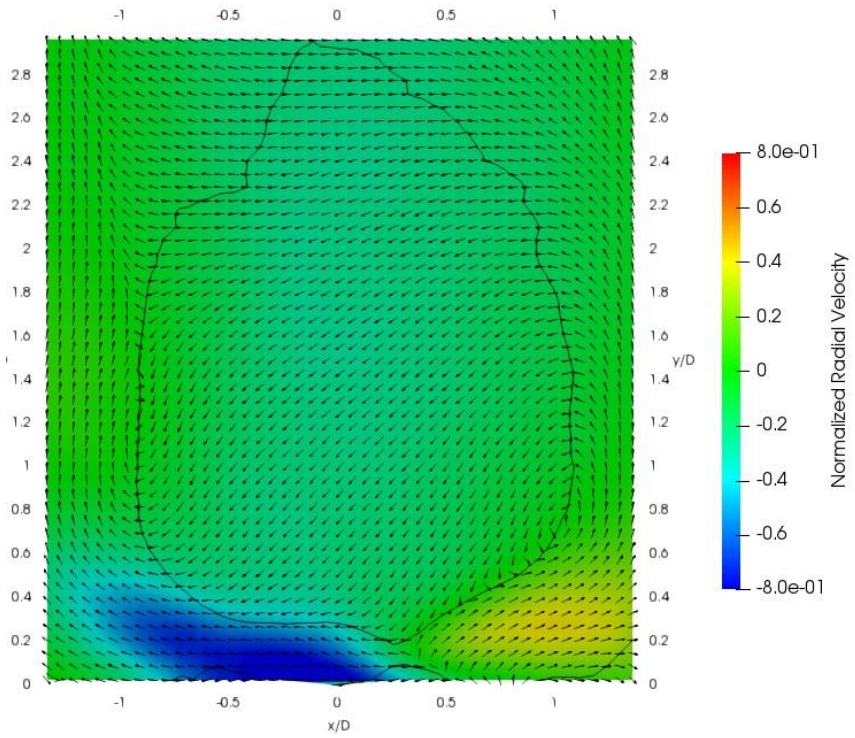

Figure B40: Radial velocity profile at Condition A2 (2% ΔP), location V7. Black line indicates contour of zero axial velocity

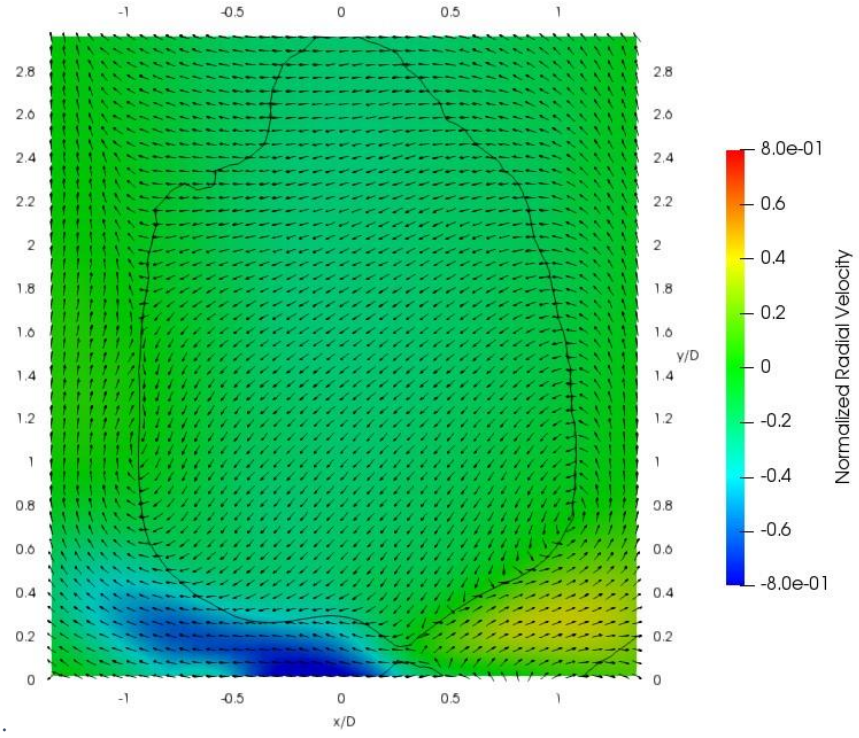

Figure B41: Radial velocity profile at Condition A4 (3% ΔP), location V7. Black line indicates contour of zero axial velocity.

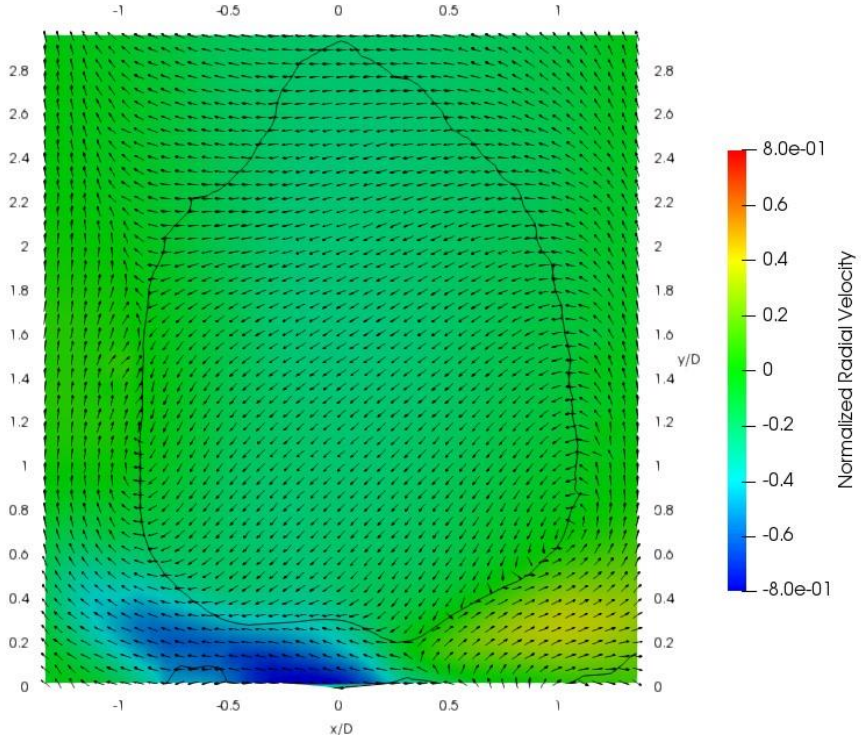

Figure B42: Radial velocity profile at Condition A5 (4% ΔP), location V7. Black line indicates contour of zero axial velocity.

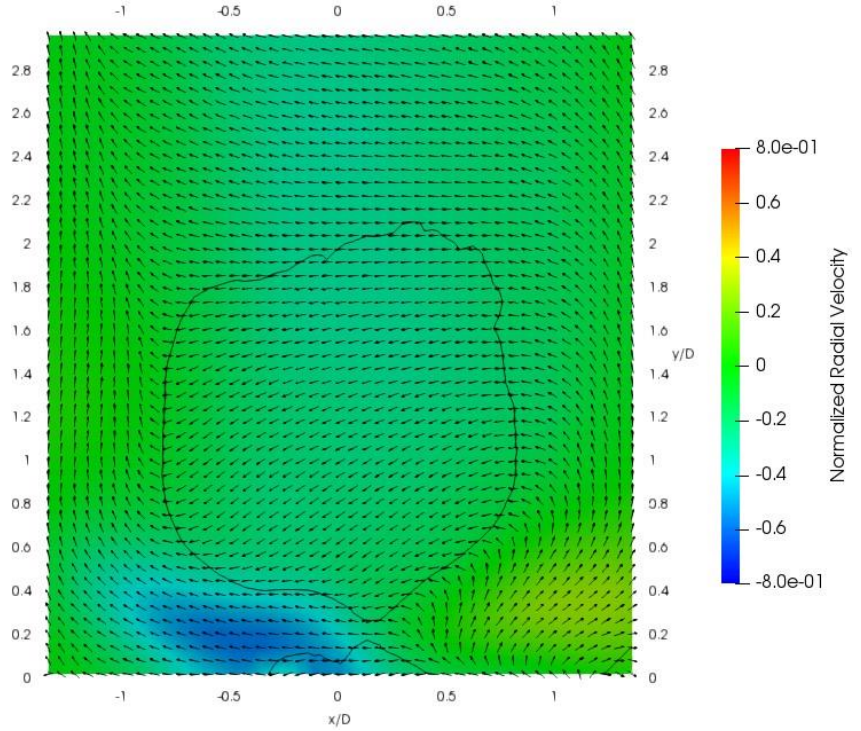

Figure B43: Radial velocity profile at Condition A4 (3% ΔP), location V8. Black line indicates contour of zero axial velocity.

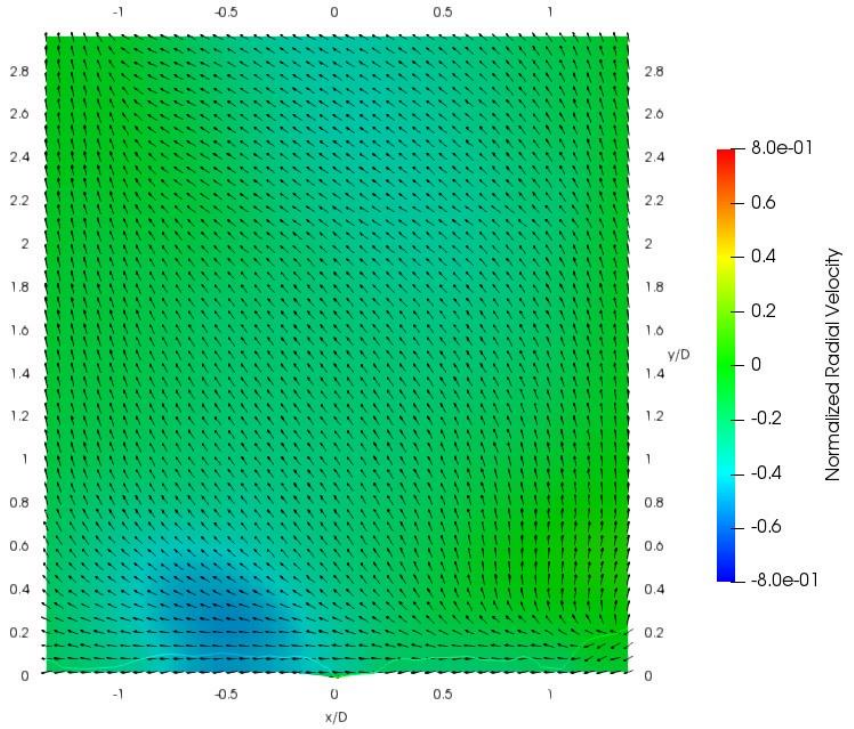

Figure B44: Radial velocity profile at Condition A2 (2% ΔP), location V9.

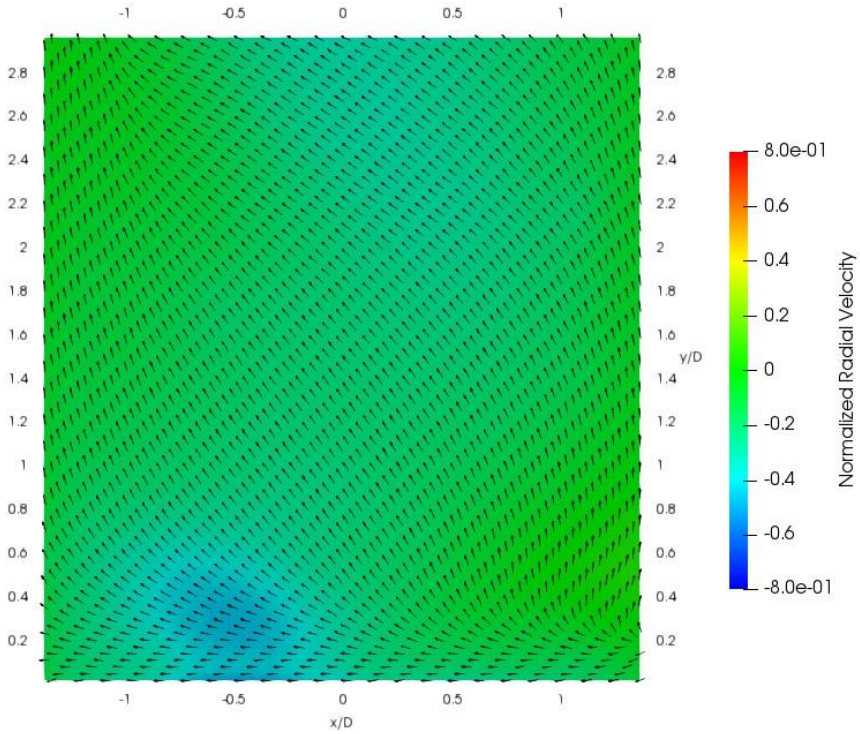

Figure B45: Radial velocity profile at Condition A4 (3% ΔP), location V9.

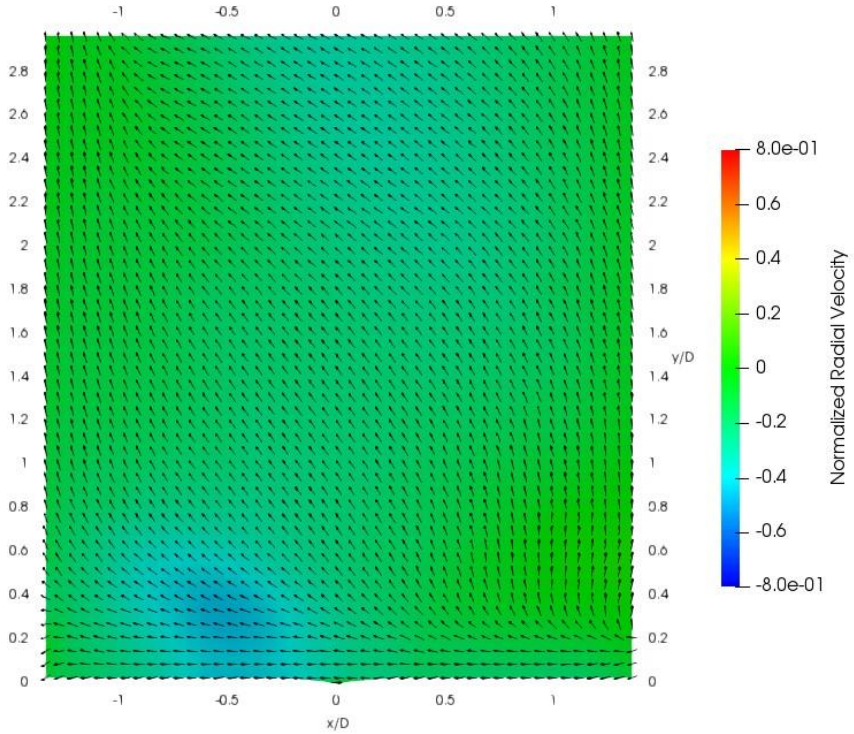

Figure B46: Radial velocity profile at Condition A5 (4% ΔP), location V9.